AN EXPERIMENTAL INVESTIGATION OF THE CHARACTERISTIC ENERGY LOSSES OF 3-10 keV LITHIUM PARTICLES IN THIN FILMS

A THESIS

Presented to

The Faculty of the Graduate Division

by

James Coyt Majure

In Partial Fulfillment

of the Requirements for the Degree

Doctor of Philosophy

in the School of Electrical Engineering

Georgia Institute of Technology

October, 1971

In presenting the dissertation as a partial fulfillment of the requirements for an advanced degree from the Georgia Institute of Technology, I agree that the Library of the Institute shall make it available for inspection and circulation in accordance with its regulations governing materials of this type. I agree that permission to copy from, or to publish from, this dissertation may be granted by the professor under whose direction it was written, or, in his absence, by the Dean of the Graduate Division when such copying or publication is solely for scholarly purposes and does not involve potential financial gain. It is understood that any copying from, or publication of, this dissertation which involves potential financial gain will not be allowed without written permission.

James C. Majure

7/25/68

AN EXPERIMENTAL INVESTIGATION OF THE CHARACTERISTIC ENERGY LOSSES

OF 3-10 keV LITHIUM PARTICLES IN THIN FILMS

Approved:

Ch.

Date approved by Chairman: 10/18/71

ACKNOWLEDGMENTS

It is a pleasure to express my sincere appreciation to my thesis advisor, Dr. J. W. Hooper, for his guidance, assistance, and encouragement throughout the performance of this research. This manuscript also benefitted from the careful reading and valuable comments of Dr. D. C. Ray and Dr. D. W. Martin. The helpful suggestions of Dr. R. K. Feeney, Dr. E. W. Thomas, Dr. E. B. Joy, and D. A. McPherson are also appreciated.

The assistance of Mercer Carithers with the thin film thickness measurements is gratefully acknowledged. Special thanks go to Bruce Keener for his untiring help in the later phases of this research.

My deepest thanks go to my wife, Patricia, who typed the rough drafts and patiently shared with me the life of a graduate student.

I would like to express my appreciation to the Controlled Thermonuclear Research Program, Division of Research, U. S. Atomic Energy Commission for the generous support of this research.

TABLE OF CONTENTS

TABLE OF CONTENTS (Concluded)

LIST OF TABLES

LIST OF TABLES (Continued)

LIST OF TABLES (Concluded)

LIST OF ILLUSTRATIONS

LIST OF ILLUSTRATIONS (Continued)

LIST OF ILLUSTRATIONS (Concluded)

SUMMARY

An experimental facility and associated techniques have been developed for the study of the characteristic energy losses experienced by heavy particles upon passage through thin solid films. The facility and techniques allow the energy losses and particle fluxes to be determined as a function of emergence angle and incident energy. The developed techniques have been applied to an investigation of lithium particles of 3-10 keV passing through thin carbon films. Some results have been compared to existing theories.

More specifically, this research has determined the energy distributions of all transmitted lithium particles for angles between 0 and 60 degrees for input energies of 10, 8, 6, and 4 keV. The angular dependence of the flux of all transmitted lithium particles was also determined for 10, 8, 6, and 4 keV incident energies. From the energy distributions, the most probable and average energy losses were determined as a function of angle and input energy. The average energy loss of all emerging particles was then determined for each input energy. The increment of projected range (film thickness) through which the particles had passed was determined interferometrically. The density of atoms in a thin film was not measured. By using the bulk density of carbon and another "fitted" density, experimental stopping cross sections and particle flux were compared to existing theories.

The developed technique also allows the measurement of charged

particle energy distributions, the flux of charged particles, and charge states. These were measured in this experiment for lithium. However, they cannot be reported as generally valid since they may depend on the surface condition of the film.

The experimental stopping cross section indicates that Lindhard's nuclear stopping cross section based on a fit of an r^{-2} potential to the Thomas-Fermi potential is more accurate in the 3 to 10 keV range than the cross section determined from the Thomas-Fermi potential directly. The multiple scattering theory of Meyer[9] was found to agree with the experimental angular flux determinations for 8 keV input energy. The agreement was within the uncertainty of the measurement when a specific gravity of 1.54 was used for the carbon film. For the energy region investigated in this research, it is clear that the most probable energy loss at zero degrees is caused not only by the more dominant electronic stopping, but by nuclear stopping as well.

CHAPTER I

INTRODUCTION

This research had two primary objectives: (1) the development of experimental facilities and associated techniques suitable for the study of the characteristic energy losses experienced by heavy particles upon passage through thin films as a function of the incident particle energy and the angle of emergence from the film; and (2) the application of the developed technique to an investigation of 3-10 keV lithium ions passing through thin films of carbon. The results are compared with existing theories to help determine the validity of these theories.

As energetic particles pass through solid matter, they lose energy through interactions with electrons and with the heavy nuclei of the solid. For particles with energies greater than those of the proposed research, the projectiles interact primarily with the electrons and hence are not deflected through large angles. In the energy range of this research, scattering by the heavy nuclei becomes significant and the particles are scattered through wide angles. An input ion rapidly charge exchanges as it passes through a solid and thus achieves a charge state equilibrium. Due to the rapidity of the charge exchange, the energy lost by the particle will not depend on the final charge state achieved.

The energy loss information is contained in the energy distributions. The average energy loss, most probable energy loss, and energy

straggling are some of the physical quantities that can be calculated from these distributions. Particles that are scattered through different angles or which have different input energies do not have the same distributions. Therefore, to study the energy losses it is necessary to determine the energy distributions for different angles and different input energies. This was a primary objective of this research for lithium particles in carbon. Average and most probable losses were then calculated as a function of angle and incident energy. In order to evaluate the importance of an energy distribution at a particular angle, it is necessary to know the probability that particles will have that distribution. Hence another primary objective of this research was to determine the flux of lithium particles as a function of emergence angle. It has been stated that the energy loss does not depend on the final charge state. Unfortunately, the final charge state is expected to depend on energy. The total particle distributions would be independent of charge state if they could be measured directly. To experimentally determine the energy distribution of all particles, it is convenient to energy analyze only charged particles. Therefore, it was necessary to develop an apparatus and technique which would determine the dependence of charge state upon the transmitted particle energy for the particular films used. Even though they cannot be considered as generally valid, charged particle energy distributions and fluxes are reported and serve as excellent consistency checks on the total particle results.

This research represents the first study of energy loss of lithium particles in carbon in the proposed incident energy range. It represents

the first known angular study of the energy loss of any atomic particle passing through a solid. Since particles which are slowed down by interactions with target nuclei are scattered through large angles, this study should contribute significantly to the understanding of the nuclear scattering process. The results should lead to more accurate range determinations by those interested in controlled doping of semiconductors and in the preparation of targets for nuclear research. The assessment of surface effects at the walls of thermonuclear and nuclear reactors could be better evaluated since radiation damage and sputtering effects should be more amenable to analysis. Nuclear physicists make lifetime measurements by determining energy losses from Doppler shifts. Their analysis would be aided by experimental results in the energy range of the present research. Preparation of energetic neutral beams of known energy and angular distributions are made possible. It also appears reasonable to expect that the present study of the energy loss of heavy particles in a solid could be extended to a study of the energy loss of ions in a plasma. The comparison of the results of this and related experiments with the existing theory may prove to be the most important application of this research since a substantiated theoretical model could be used to calculate results for other materials not experimentally examined.

Scientific Background

The comprehensive theory of Bohr[1] has had a profound effect on particle stopping theory. Bohr separates the energy loss into two categories. The first involves the elastic interactions which transfer energy to the target atoms as a whole and is usually called "nuclear stopping." The

second is the loss of energy due to inelastic processes such as ionization and excitation where energy is given to electrons and is usually referred to as "electronic stopping." For incident velocities near the velocity $v_o = e^2/\hbar$ the two processes are comparable in magnitude. Nuclear stopping predominates at lower velocities. In the velocity region corresponding to nearly equal nuclear and atomic stopping contributions, Lindhard et al.[2] have extended Bohr's theory. Using a Thomas-Fermi treatment, they obtained a "universal" cross section for nuclear and electronic stopping. Under the assumption that $\frac{dE}{dR_t} = -NS_e - NS_n$ where $\frac{dE}{dR_t}$ is the total energy loss per unit of path length, S_e is the electronic stopping cross section, S_n is the nuclear stopping cross section, and N is the density of target atoms, they obtained for the special case $v \leqq v_o Z_1^{2/3}$

$$S_e = \xi_e \left[8\pi a_o e^2\right] \left[\frac{Z_1 Z_2}{(Z_1^{2/3} + Z_2^{2/3})^{3/2}}\right] \left[\frac{v}{v_o}\right] \quad \text{erg}\cdot\text{cm}^2/\text{atom} \qquad (1)$$

and

$$S_n = \xi_v \pi^2 e^2 a Z_1 Z_2 \left[\frac{M_1}{2(M_1 + M_2)}\right] \quad \text{erg}\cdot\text{cm}^2/\text{atom} \qquad (2)$$

In Equations 1 and 2, Z_1 and Z_2 are the atomic numbers of the incoming and target particles, respectively; a_o is the Bohr radius; $v_o = e^2/\hbar$; v is the velocity of the incident particle; $a = (0.8853\ \hbar^2/me^2)(Z_1^{2/3} + Z_2^{2/3})^{-1/2}$; $\xi_v = 2/(2.7183)(0.8853)$; and ξ_e is a constant "thought" to have a value of $Z_1^{1/6}$. All quantities are in Gaussian units. Equation 2 is an approximation to their more exact nuclear stopping curve that was determined numerically. The approximate result of Equation 2 was calcu-

lated using an inverse squared potential that had been appropriately fitted to the Thomas-Fermi potential. The general features of their theory for electronic stopping have been verified by a group working at McMaster University[3]; however, the McMaster group found a pronounced periodic dependence on the atomic number of the incoming particle. Recent theories of Cheshire et al.[4] using Hartree-Fock wave functions indicates this is due to the size of the incoming ion. The periodic dependence on atomic number has been experimentally verified by Fastrup et al.[5] at energies greater than 100 keV.

The particles pass almost straight through the stopping medium when electronic stopping dominates. Nuclear scattering, which becomes significant at lower velocities, leads to scattering of particles through large angles. Nielsen[6] has suggested that the concepts of diffusion might be applied for this low energy range since the large angle scattering leads to random motion. Such a diffusional approach has been applied by Tsendin[7] whose theoretical angular distributions were found to be in qualitative agreement with the experimental results of Lepeshinskaya and Zarutskii.[8] Direct comparison of experiment and theory was not possible since the experiment measured only charged particles and the theory pertained to the net number of particles (charged and neutral) emerging from the film.

Meyer[9] has recently calculated the multiple scattering of low energy heavy particles in solids. He has obtained the angular distribution as a function of the film thickness, film density, film type, and of of the energy in the film. He used Lindhard's numerically calculated "nuclear" differential cross section and then closely followed the theory of Moliere.[10] His numerical results are tabularized in his paper.

Stopping of energetic particles has been studied experimentally by two different methods. One method consists of determining the range of particles incident on thick targets. The second is to determine the energy loss experienced by particles passing through thin films. The two can naively be related by the formula

$$R_t(E) = \int_0^E \left[\frac{dE'}{dR_t}\right]^{-1} dE' \qquad (3)$$

where E is the incident energy of the particles, R_t is the particle range, and $\frac{dE'}{dR_t}$ is the average energy loss per unit path length. In the velocity region of interest in this research, range concepts become somewhat ambiguous because of the large angle scattering arising from nuclear interactions. The experimentalist measures the "projected range" which is defined as the distance that the projectile travels into the solid in the direction of incidence. The theoretician most often calculates the total path length traveled by the particle in the solid. Lindhard et al.[2] enumerate the different range concepts and calculate the connection between them for input particles that are heavier than the target particles. Schiott,[11] using the Thomas-Fermi model of Lindhard et al., recently calculated the relationships between projected range and the true range for incident particles that are much lighter than the target particles. Sanders,[12] using Lindhard's differential cross sections for inverse power potentials, has calculated many of the moments of the range distributions. Included among these was the average projected range as a function of energy. However, he did not include the effects of electronic stopping in his theory.

The projected range of low velocity projectiles has been studied experimentally by the Chalk River group.[13] They bombarded solid targets with mono-energetic radioactive ions and then studied the depth of penetration by removing successive uniform layers of target material and determining the radioactivity in each layer. Good agreement between experiment and the theory of Lindhard et al. was obtained for 10 to 1000 keV Na, Ar, Kr, and Xe incident upon Al_2O_3 amorphous films. This technique is limited in that information may be obtained only for radioactive projectiles.

The measurements of electronic stopping cross sections by the McMaster University group of Ormrod, Duckworth, Van Wijngaarden, and Macdonald[3] represent a major contribution to the knowledge of stopping in solids. They have studied projectiles with $Z \leq 19$ for input energies between 10 and 100 keV in films of C, Al_2O_3, Al, and B. By selecting only particles which emerge from the solid at zero deflection angle, they avoid consideration of most of the particles which have undergone nuclear scattering. A Monte Carlo calculation was used to evaluate the contribution of those particles which were successively scattered out of and then back into the beam by nuclear scattering processes. Their method appears to have yielded accurate determinations of the electronic stopping, but not of nuclear stopping.

Measurements by Barnett and Ray[14] seem to indicate that nuclear scattering is significant for protons in the energy range 10-30 keV. Using a semiconductor detector operated in a dc mode, they determined an "average" energy for all particles emerging from the film. The resulting average energy loss per unit of projected path length was found to be

about a factor of 2 greater than that of the McMaster University group's results for electronic stopping. Measurements by Van Wijngaarden et al.[15] of total energy losses in phosphors also imply that nuclear effects are significant.

An interesting technique has been advanced by White and Mueller[16] whereby incident particles are reflected from thin gold layers that were separated by a thin layer of aluminum. Energy differences in the peaks of the spectrum of the back-scattered particles were interpreted as the energy loss in aluminum. These films were mounted on thick substrates and thus eliminated many of the problems associated with making uniform thin films as required for research at low energies. Their work again only measured the electronic stopping; however, good agreement was obtained with Ormrod and Duckworth[3] for H and He projectiles. White and Mueller indicate that their techniques could probably be extended as low as 10 keV, but any lower extension would be complicated by nuclear effects.

Morita et al.[17] have presented some results for stopping of H in Au, Ag, Cu, Al, and Be which are not in agreement with Ormrod. The energy used by these investigators was 7 to 40 keV. Fair agreement is found with the theory of Lindhard et al., but ξ_e is found to depend upon both Z_1 and Z_2. Bernhard et al.[18] examined electronic stopping of 30 to 100 keV lithium in films of carbon, aluminum, titanium, nickel, and copper. They also measured the half widths of angular scattering of 10-100 keV lithium ions in films of carbon and aluminum. They compared their results with Meyer's theory for the angular distribution of transmitted particles.

The work of the Russians Zarutskii,[19] Gott and Tel'kovskii,[20] and Arkhipov and Gott[21] and the work in this country of Wax and Bernstein[22]

represent the only significant experimental results known to date for particles with energies below 10 keV. Zarutskii examined H^+ and Li^+ incident on copper films, Gott and Tel'kovskii studied H^+ and D^+ on silver films, and Arkhipov and Gott looked at H^+ on ten different types of films. The Russian groups determined the energy loss for only those particles which emerged from the films at zero deflection angle. Thus the full effect of nuclear scattering was not measured. The work of Wax and Bernstein represents the first known study of particles which emerge from the films at angles other than the incident angle. Apparently these investigators were interested only in the total flux of particles emerging at a given angle. Flux data for 3, 5, and 10 keV protons passing through a $2\mu g/cm^2$ carbon film were given for angles up to 28 degrees.

Experimental Methods of This Research

This research was complicated by the necessity of measuring energy distributions and particle fluxes as a function of angle. A rotatable Li^+ source and fixed detectors were used. Faraday cups were used to measure charged particle flux. A 127 degree electrostatic energy analyzer was used to measure the energy distributions. The flux of all particles (charged and neutral) was determined with the use of a detector whose properties did not depend on the charge state.

This experiment differs in many ways from previous work. The entire energy distribution function was measured and not just the most probable values. The energy distributions were measured at angles other than zero. Corrections were made for the energy analyzer transmission function's dependence on energy. This correction had not previously been

made for heavy particle energy analysis. It was determined that the measured energy distribution is affected by the energy dependence of the final charge state. The measurements were corrected for this effect for the first time in this research. Angular distributions were determined for all particles and not just for the charged particles. In order to prevent erroneous angular scatter, the thin films were mounted without supporting grids. This research represents the first study of the energy losses of lithium in carbon for energies below 10 keV.

CHAPTER II

EXPERIMENTAL APPARATUS

An experimental facility suitable for the study of characteristic energy losses of energetic heavy particles passing through solids has been developed. The facility has been used for the study of lithium ions passing through thin carbon films. It consisted of a rotatable source with fixed detectors and allowed the measurement of energy distributions and particle fluxes at any angle between 0 and 70 degrees.

The most important parts of the apparatus are shown in the photograph in Figure 1. These same parts are represented schematically in Figure 2. Li^+ ions were thermionically emitted and electrostatically accelerated in the Li^+ source. The beam was collimated into a thin pencil beam and entered the target film normal to its surface. The source and target holder were fastened together and were rotatable about an axis passing through the target. The target holder could be moved vertically along the rotation axis, thus allowing the film to be removed from the path of the beam. Two Faraday cups whose outputs were connected to electrometers were used to measure charged particle flux. A detection system which consisted of a thin film of carbon mounted just in front of a channel electron multiplier was calibrated and used as a detector that was independent of charge state. An electrostatic cylindrical analyzer with a channel electron multiplier at the output was used to determine the energy distribution of the emerging charged particles. All of the above components

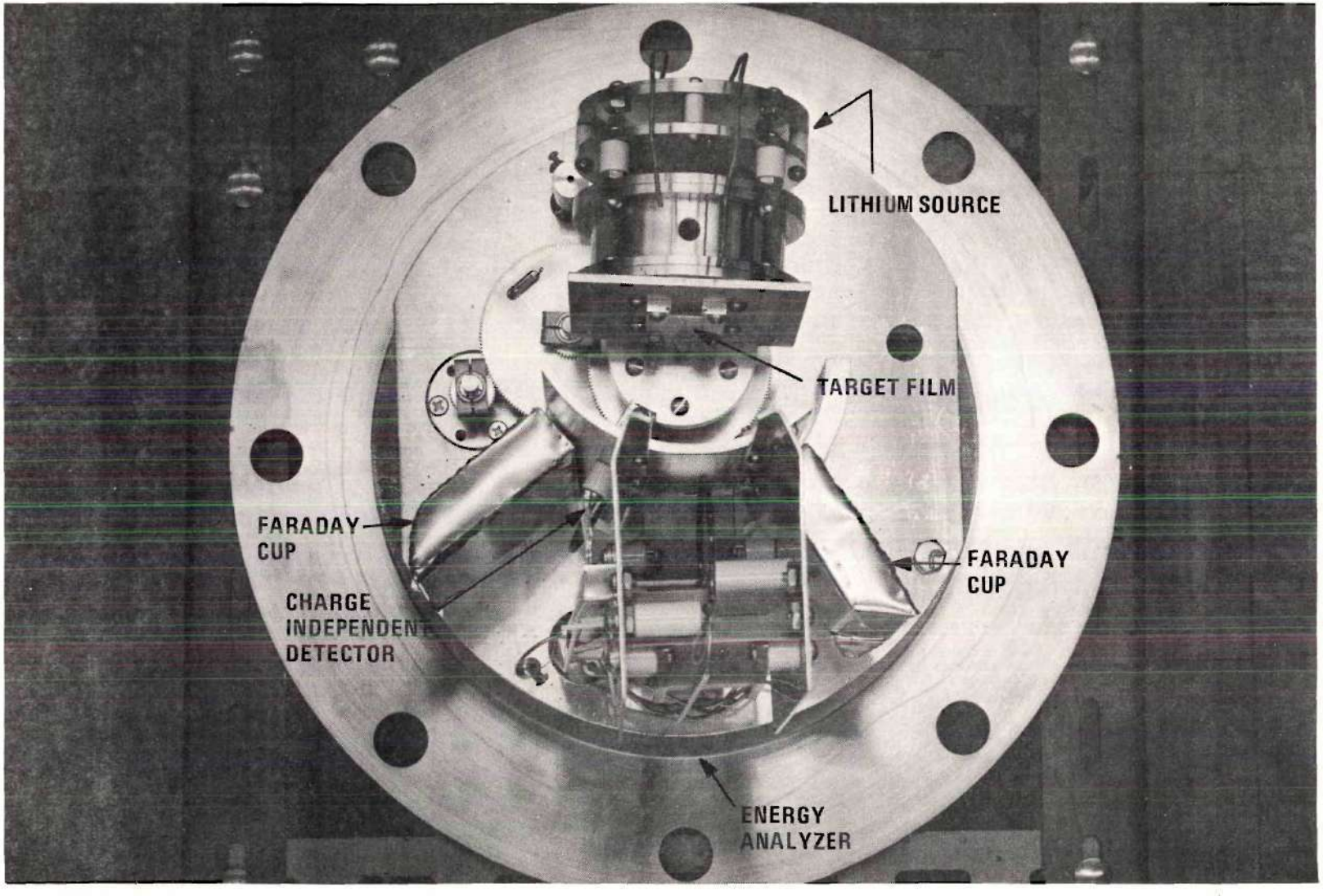

Figure 1. Photograph of Energy Loss Apparatus (Shielding not shown)

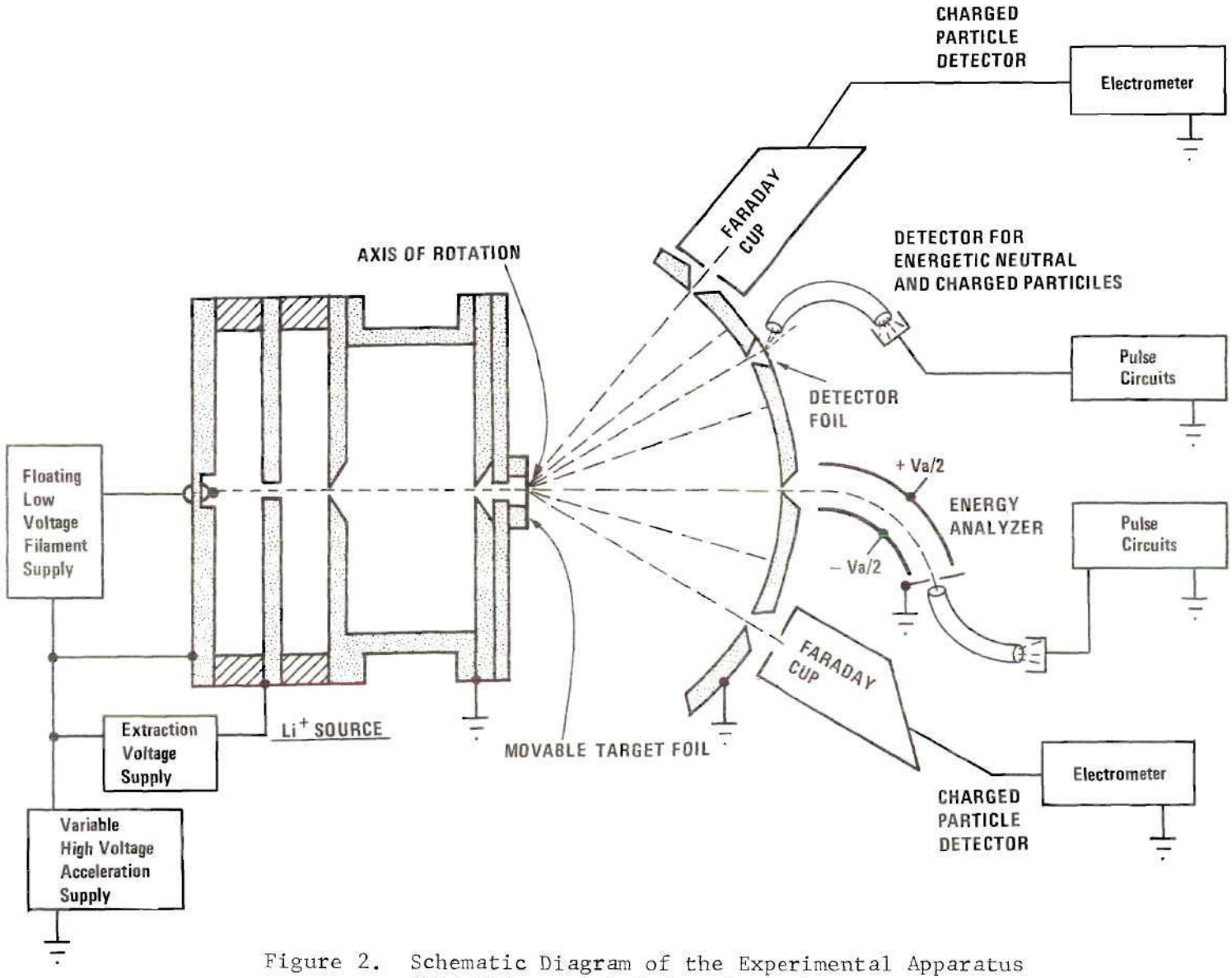

Figure 2. Schematic Diagram of the Experimental Apparatus
(Shielding omitted for clarity)

were rigidly connected to a stainless steel experiment plate which was attached to the top cover of an ultrahigh vacuum system. These components were suspended inside the vacuum chamber, which was usually evacuated to pressures of the order of 10^{-8} Torr.

Figure 3 is an overall view of the apparatus used in this experiment. It includes everything used except the thin film measuring and handling equipment and the Univac 1108 computer. Of special interest in Figure 3 is the data acquisition system which greatly facilitated this research. The data acquisition system scanned all of the signal monitoring instrumentation and produced punched paper tape and teleprinted page. The paper tape output was used to enter the data on the Univac 1108 computer for processing.

The remainder of this chapter will describe in greater detail all of the components of the apparatus mentioned above.

Vacuum System

A very clean ultrahigh vacuum system was assembled for use in this experiment. The walls of this vacuum system were made of stainless steel. No organic materials were used inside the vacuum chamber. Metals and ceramics used inside the vacuum chamber were selected for their good ultrahigh vacuum characteristics. Heliarc welds were used throughout and were always made on the vacuum side of the vacuum walls.

A chamber, 9 inches in diameter by 11 3/4 inches in depth, enclosed the principal apparatus. The chamber was surrounded by a magnetic shield which reduced the earth and pump fields in the chamber. In order to prevent distortion of the top cover from affecting the vertical beam align-

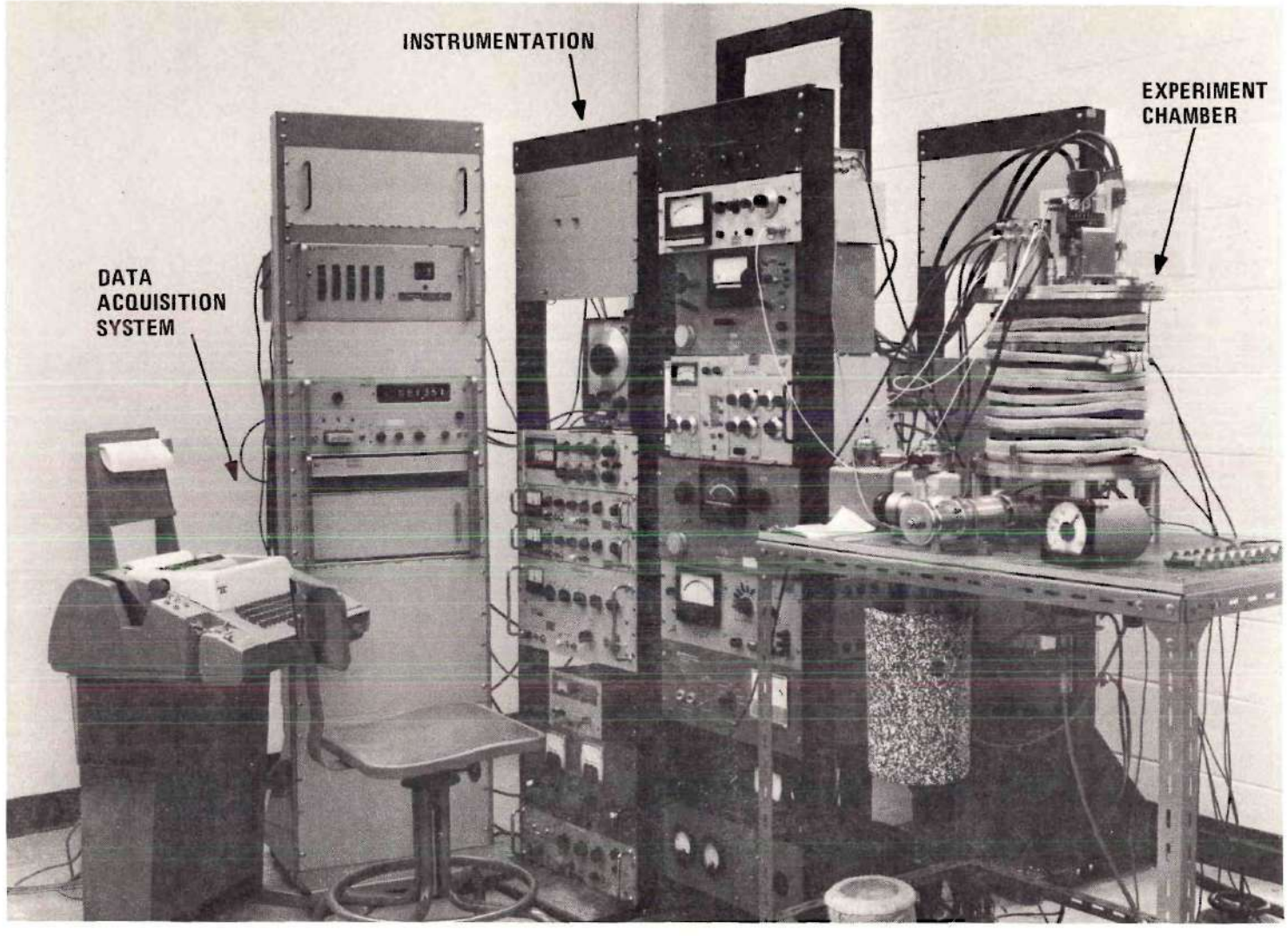

Figure 3. Overall View of Energy Loss Apparatus

ment on detector apertures and to reduce the number of blind tapped holes in the top cover plate, the principal apparatus was rigidly affixed to a 1/8 inch stainless steel experiment plate which was suspended from the chamber cover. Stainless steel lock washers used as spacers between the experiment plate and top cover held the plate stationary but absorbed stresses produced by distortion of the top cover. The use of the experiment plate also simplified changes in the experimental arrangement. The chamber cover was made of 1/2 inch stainless steel. It had been machined to accommodate four high voltage feedthroughs, one rotary motion and one linear motion feedthrough, an eight pin instrumentation feedthrough, and four shielded signal feedthroughs.

All flanges throughout the system were of the ConFlat type with copper gaskets except for the chamber cover, bottom, and one of the high voltage feedthroughs which were of the compression type utilizing aluminum o-rings. The copper gaskets were purchased from Varian, but due to the use of non-standard sizes, the aluminum o-rings had to be hand fabricated. The simplest fabrication method seemed to be to butt two ends of the wire together so that they were aligned approximately 45 degrees from vertical. When the ends were heated rapidly to the melting point by a small torch and the two sides were forced together, a small ball of aluminum formed at the joint. This ball was then filed to approximately the original size of the wire, and the entire o-ring was then polished with very fine steel wool until it was smooth. Cold finished aluminum wire, alloy AA1100-0, was used. Air Reduction Company Formula Number 40 Aluminum Welding Flux appeared helpful in preventing oxidation during welding.

Pumping System

To prevent pump oil from attacking the thin films and channel electron multipliers used in the experiment, sorption and ion pumps were used instead of the more conventional roughing and diffusion pumps.

The sorption pump selected for rough pumping was a Varian VacSorb Pump, type 941-6001. This pump rough pumped the system to below 10^{-2} Torr at which point the ion pump could be started. Due to initial outgassing of the ion pump, it was necessary to leave the sorption pump connected to the system for approximately one-half hour. The rough pump pressure was monitored with a Veeco thermocouple gauge, type DV-1M. When the ion pump ceased outgassing, the rough pump region was completely valved off from the ultrahigh vacuum region with a Granville Phillips Auroseal UHV Valve, series 267.

The ion pump used was a 15 liter per second Varian VacIon Pump, type 911-5011. It required the use of a magnet, type 911-0012. The pressure could be read directly to below 10^{-8} Torr from the Varian VacIon Pump Control Unit, type 921-0013. This pressure determination was adequate for this experiment. Unfortunately, the use of the ion pump caused a noticeable background electron current in the Faraday cups. The source of the problem appeared to be highly energetic neutrals leaving the pump.[23] A baffle placed at the pump port of the vacuum chamber reduced the electron current to below 10^{-15} amps. The baffle was made of 0.003 inch stainless shim stock and consisted of two boxes, one of which enclosed the other. Each of the boxes had the bottom and one side open. The open sides faced in opposite directions making it necessary for particles to be

multiply reflected to enter the experiment region as illustrated in Figure 4.

Bakeout and System Performance

The sorption pump was baked for about two hours at 300°C before each pumpdown begins. After about 24 hours of operation or when the pressure reached approximately 10^{-6} Torr, the vacuum chamber was warmed by heating tapes wrapped around it. The temperature was slowly increased to approximately 140°C taking care not to overload the small ion pump. It usually took about 48 hours for the chamber walls to reach 140°C. Top and bottom covers were not baked above 100°C. The chamber was then baked for approximately 24 hours at that temperature. At the end of the bakeout period and before the heat was removed, the ion source filament was heated to prevent its outgassing vapors from being readsorbed on the walls. The pressure increased due to the heated filament but reduced to the original pressure in only a matter of minutes. The system was baked for about one more hour and then the heating tapes were turned off. The pressure then fell to 5-9 $\times$ 10^{-8} Torr. No effort was made to further reduce the base pressure since it had been reported that the gain of a channel electron multiplier suffers fatigue and sometimes becomes unstable if the pressure is reduced to below 10^{-8} Torr.[24] It was necessary to reduce pressures to the low 10^{-7} range to avoid problems with high voltage breakdowns in the experiment chamber.

Ion Source

The Li^+ ion source used in this experiment was a thermionic type similar to that used in this laboratory previously by Lineberger.[25] It

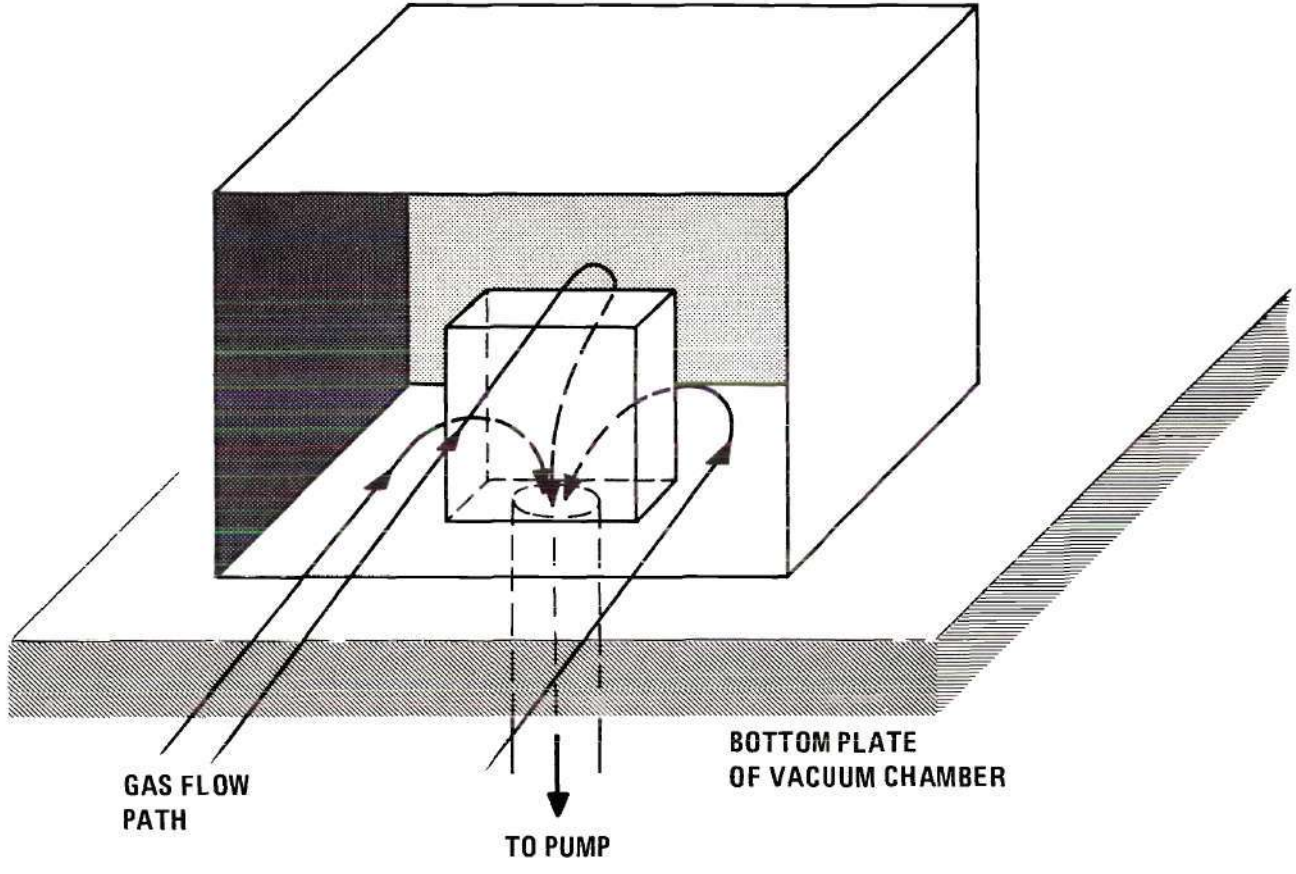

Figure 4. Baffle to Remove Ion Pump Noise

differed significantly, however, in that it was rotatable, was used to produce higher energy beams, and had a circular beam cross section.

Emission Material

The emission material was synthetically prepared β-eucryptite, $Li_2O \cdot Al_2O_3 \cdot 2SiO_2$. It was enriched in the mass seven isotope so that the velocity of the Li^+ ions was unambiguously known. This material was prepared by Dr. R. A. Strehlow of the Oak Ridge National Laboratories for use by Lineberger.

The details of preparing the filament are given by Lineberger[25] and will not be repeated here. The filament used in this experiment was shorter, 9/16 inch, but about the same width, 1/8 inch, as Lineberger's. Lineberger[25] showed that, after five hours of operation at 1000°C, more than 99.9 percent of the total emission was lithium ions and 99.7 percent was the mass seven isotope. This result was important because it removed the necessity for mass analysis within the experiment. The impurities did not seem to be removed as fast as indicated by Lineberger when a low extraction voltage was used. But when a voltage greater than 500 volts was used, the problem disappeared. Apparently an electric field strength greater than 50,000 volts per meter is required for the rapid removal of impurities. Since small currents, less than 10^{-10} amps, were required in this experiment, the filament was used at temperatures below 1000°C after the initial purifying conditions had been met.

Source Construction and Alignment

The principal design criteria for this source were that it be stable upon rotation and that beam direction be well defined. The attain-

ment of large currents was not a criterion.

A photograph of the source is given in Figure 5. The source was constructed of circular stainless steel plates 1/8 inch thick and 3.0 inches in diameter. The extraction plate was separated from both the filament plate and first collimating plate by 4 steatite insulators. The distance between filament plate and extractor was 3/8 inch, and the distance between extractor and the first collimation plate was 1/2 inch. The first collimation plate was at ground potential so the full acceleration of the ion was developed between the filament plate and collimating plate (see Figure 2). The extractor had a 3/64 inch hole in the center and each of the collimating plates had a tapered hole in the center for which the minimum diameter was .037 inch. The collimating plates were separated by a rigid stainless steel spacer machined from solid stainless steel. The distance between collimating plates was 1 1/8 inches. To give better beam direction definition, focusing fields were eliminated where possible. A slot was milled out of the accelerating potential plate so that the filament would lie even with the surface of the plate to prevent distortion of the equipotential lines between plates. After it was heated, the center of the filament bowed slightly into the slot. The electric field was determined primarily by the flat region of the plates. The bent filament therefore caused only a small perturbation of this field. The beam direction definition was found to be better than the ± 2 degrees that could be expected from the collimating plates alone (see Chapter III).

The alignment of the source was important to prevent introducing systematic error in the determination of angles. Many methods were tried including a laser technique; however, the simplest method by far was to

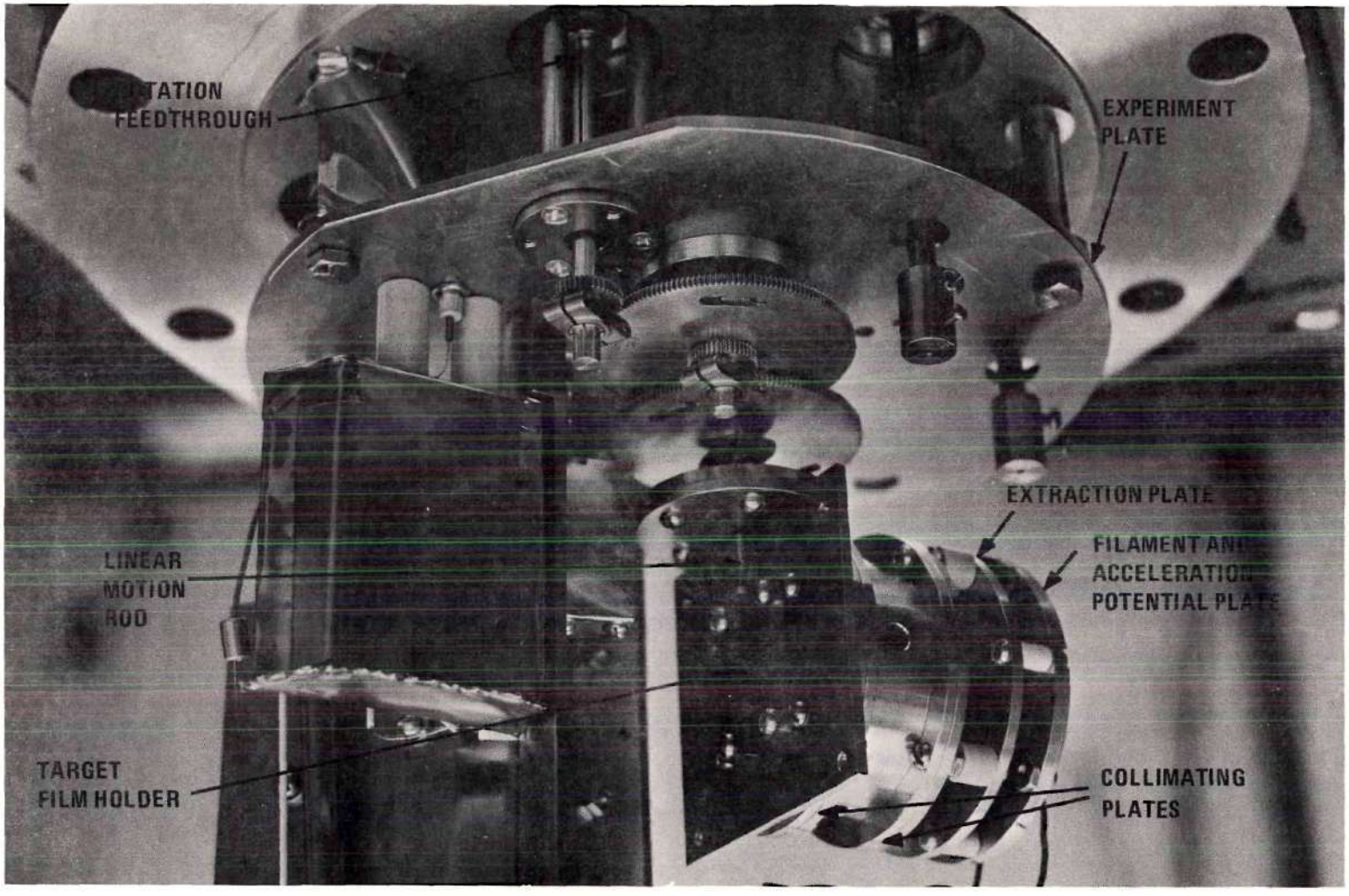

Figure 5. Photograph of Ion Source

use a 1/32 inch precision ground stainless steel shaft purchased from PIC Design Corporation. The shaft was placed in the center holes of the collimating plates. The centers of the other plates were then aligned with the shaft. The most important consideration was that, as the source rotates, the beam was on the same horizontal level at each detector aperture. With the alignment screw shown in Figure 6, the alignment can be made to about ± 0.1 degree which is small compared to the error in angular resolution, ± 0.5 degree, due to the finite size of the apertures. This alignment was checked electrically after the apparatus was placed in vacuum (see Chapter III).

Rotation Mechanism

A schematic representation of the rotation mechanism which was located inside the experiment chamber is given in Figure 6. As can be seen, the entire source and target holders rotated on an axis that passed through the target.

The bearing adapters shown were PIC Precision Adapters, type A. The gears, rods, bearings, and clamps (not shown) were all stainless steel precision PIC parts. The bearings were degreased and relubricated with MoS_2 before they were placed in the vacuum. The overall gear ratio was 16 to 1. The larger gears were anti-backlash gear assemblies. No backlash in the entire rotation system could be observed. A 2 degree rotation in either direction of the mechanism outside the chamber will cause a change in current to a detector if the beam has been directed onto the edge of the detector aperture. This rotation corresponds to a 1/8 degree movement of the source. Therefore, mechanical backlash does not contribute to errors in angular determinations.

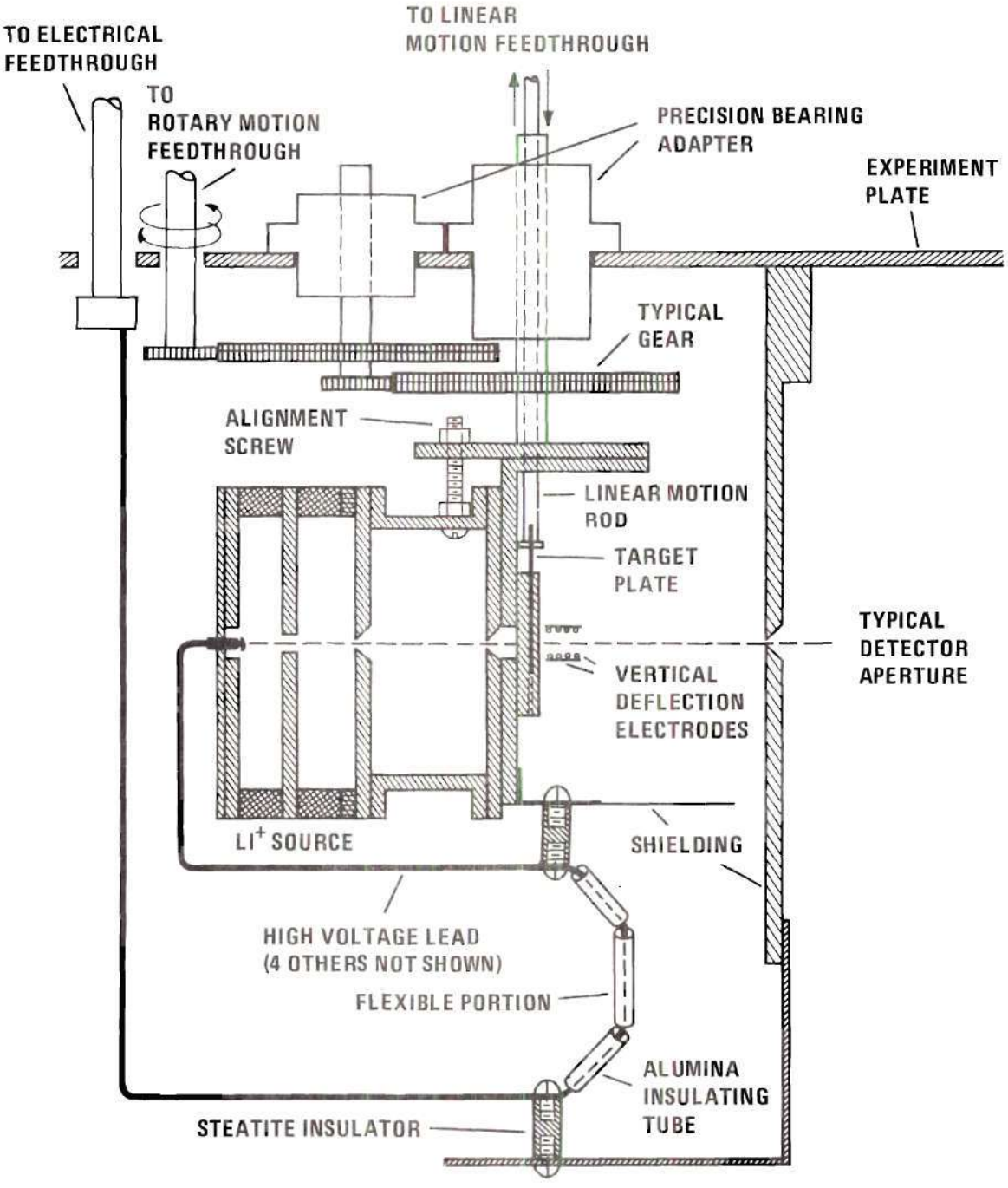

Figure 6. Source Rotation Mechanism

A typical high voltage lead is shown at the bottom of Figure 6. Since the source can rotate almost 180 degrees, five of the leads had to be brought in to a point near the axis of rotation. This minimized the net motion of the leads. Two of these leads supplied the ac filament current and the high dc voltage for the acceleration potential plate. Another lead supplied the extraction voltage. The remaining leads connected to the vertical deflection electrodes. The acceleration potential was supplied by a Fluke Model 410B high voltage dc power supply of 1-10 kV range with 0.25 percent accuracy and better than 0.005 percent regulation and ripple control. The extraction voltage was supplied by voltage dividing the acceleration potential across a 5 megohm variable resistor and a 50 megohm resistor. Thus, the maximum potential difference between accelerator and extractor is approximately 1/11 of the acceleration potential.

The construction of the rotary motion feedthrough on top of the experiment chamber is shown in Figure 7. It consisted mainly of a Varian Positive Drive Rotary Motion Feedthrough, type 954-5120. The Varian feedthrough was modified to provide manual readout of the angle on a PIC Drum Dial and Vernier Set. A 10 turn potentiometer, Bourns type 34005-1-102, was mounted on the axis of rotation. The voltage of a mercury battery was applied to this one kilohm potentiometer and provided a signal which was a linear function of the angle. The computer program converted that reading into the four angles between the beam path and each detector. The potentiometer had a linearity of 0.15 percent. The accuracy of the data acquisition system, which monitored this signal, was ± 0.02 percent

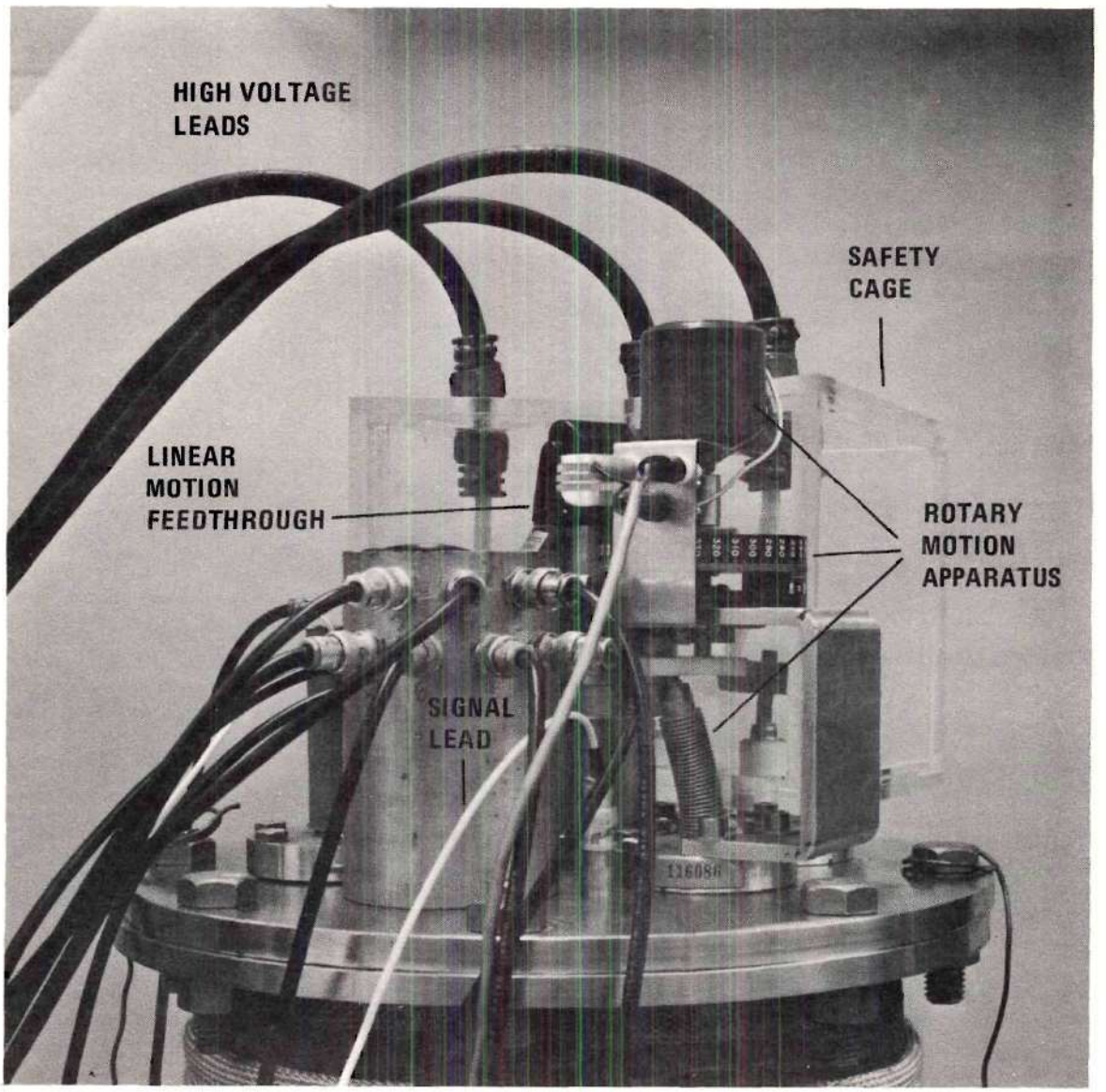

Figure 7. Photograph of Chamber Cover

of the reading. Compared to the ± 0.5 degree possible error due to the finite size of the detector entrance apertures, the error in electrical measurement was negligible.

Figure 7 also shows the high voltage plexiglas safety cage. This cage enabled the frequent adjustments of both motion feedthroughs to be made without danger of accidentally contacting the high voltages employed.

Target Films

Carbon films which were nominally 2 $\mu g/cm^2$ thick were used in this research. They were supplied by Yissum Research and Development Company of Israel. The quoted accuracy of film thickness was +100 or -50 percent. Therefore, the film thickness had to be determined in this research. Details of the thickness measurement are given in Chapter III. The films were mounted on the target plate shown in Figure 8. Target preparation and movement are described below.

Film Preparation

The films were supplied on glass microscope slides. They were removed from the slides in hot water. Before they were removed, each film was scratched with a pin so that it would separate into several films each of which were the approximate size of the target plate on which they were to be mounted. A laboratory jack and ring stand were used to lower the film into the water. The slide was mounted on the ring stand at about a 45 degree angle with the surface of the water. The slide was gently lowered into the water until the water just touched the bottom edge of the film. The slide was held in this position until the water lifted up the edge of the film. The slide was then carefully lowered further into the

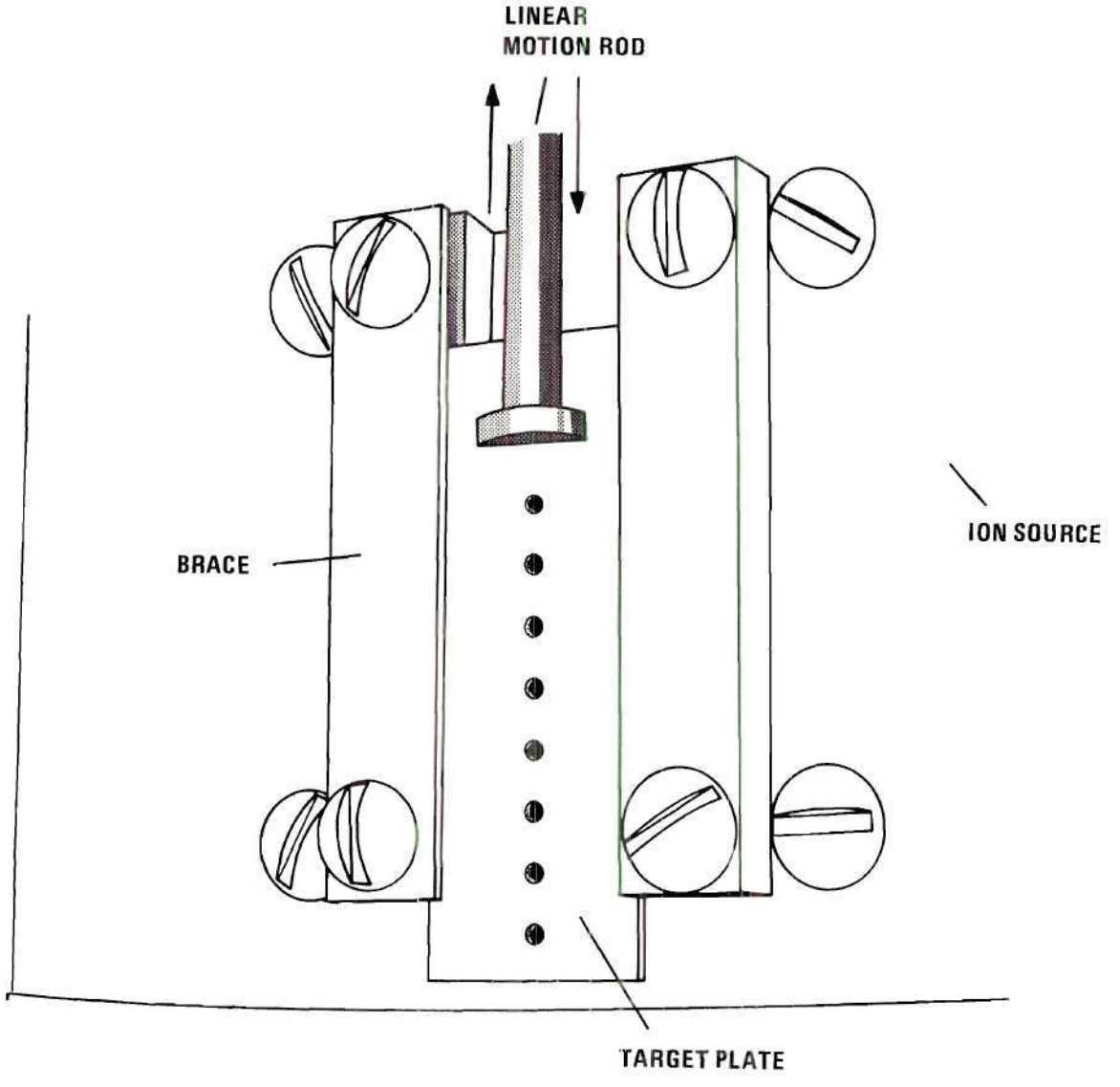

Figure 8. Film Movement Mechanism

water. The film separated from the slide and floated on the surface of the water. It was necessary that the surface of the water approach the scratch in the film parallel to that scratch or the film would break. When necessary, the lowering was stopped just before the scratch reached the surface of the water. The slide was adjusted on the ring stand so that the scratch was parallel to the water's surface. The scratch was lowered to the water's surface and the film then floated completely free of the slide.

A target plate was lowered by hand into the water. The plate was pushed against the edge of the film until the film stuck to the plate. The film and plate were then removed vertically from the water. The target plate and film were kept vertical until the film was dry. The film was examined under a stereoscopic microscope to insure that it was not wrinkled or torn. Soap in the water helps to keep films from tearing while drying. However, soap was not used in the water for this research.

The above procedure gave a carbon film across each of the 0.045 inch diameter holes in the target plate. The film was completely removed from one of the holes in the target plate. Free passage of the ion beam was therefore possible through that hole.

Target Movement

The target plate was 1/4 inch from the second collimating plate. There are eight vertically alighed holes 1/8 inch apart in this plate. At least one hole had no film across it. The target movement rod pulled or pushed the target plate into position for the beam to pass through a selected hole. The ion source rotates about the axis of the target move-

ment rod. The slotted braces which hold the target plate on either side are rigidly fastened to the source. These braces forced the target plate to rotate with the source so that the ion beam always enters the film normal to its surface. The head on the movement rod kept the vertical position of the plate constant as it was rotated. The slots and head were lubricated with MoS_2 for smoother operation. The movement rod passed through the gear shaft and attached to a Varian Linear Motion Feedthrough, type 954-5049. This feedthrough had a digital readout, resolution of better than 0.001 inch, and total travel of 1.10 inches.

Ion Detection System

Two Faraday cups were used as detectors to measure the charged particle flux in this experiment. They differ only in that one had a larger entrance aperture than the other. The small aperture detector was used in calibration of the energy analyzer and the charge state independent detector. The large aperture detector was used to measure the total current into the target film and to measure the angular distribution of charged particles which pass through the film.

An entering beam of particles would strike the back surface of each Faraday cup at about a 45 degree angle. This prevented specular reflection of part of the beam back out the opening of the cup. The fraction of total solid angle that was seen from the point where the beam struck each cup was less than 0.0003. Therefore, loss of secondary electrons and reflected ions should have been negligible.

The entrance aperture of the large detector was 1/8 inch in diameter. Since it was two inches from the target, the angular resolution

was ± 1.8 degrees. The small aperture detector had a 0.039 inch diameter entrance aperture. It was also two inches from the target film and thus had an angular resolution of less than ± 0.6 degree.

Except for the entrance aperture, both cups and their leads were completely enclosed by shielding which was grounded. Since the detectors were not rotated, shielding with extremely rigid material was not necessary and stainless steel .003 inch shim stock could be used. Each lead was brought through the vacuum chamber cover with a Ceramaseal MHV Coaxial Feedthrough, type 804B5230. Outside the vacuum system a Microdot Low Noise Cable, type 260-3819, connected each detector to a Cary Model 31 Vibrating Reed Electrometer. The electrometer which monitored the large aperture current had a turret switch, which allowed the use of four different large resistors in the feedback path. The three smaller resistors were one percent resistors. The largest was a two percent resistor. All measurements except for currents smaller than 10^{-14} amps could be made using the one percent resistors. Since the electrometer gave a signal proportional to the input current times the resistor value, the input current could be determined within the accuracy of the resistor used.

Charge State Independent Detector

In order to measure the flux of all (charged and neutral) lithium particles transmitted through the thin film, a detector which was independent of charge state was constructed. It was similar to that suggested by Wax and Bernstein.[21] The charge state independent detector (hereafter referred to as the CSI detector) consisted of a small entrance aperture,

a thin film of carbon, a channel electron multiplier, and a small electron collection electrode.

The entrance aperture had a diameter of 0.039 inch. The two inches distance from the target gave an angular resolution of less than ± 0.6 degree. The thin film of carbon was mounted on a 75 mesh grid placed 1/8 inch behind the entrance aperture of the detector. An energetic particle which entered the film would very quickly reach charge equilibrium.[26] Thus any particles which left the film and entered the channel electron multiplier would not depend on the charge state of the incident particle. Of course the detection of particles leaving this detector film would depend on the type of particle and its initial energy. Since the output of this detector did not depend on the charge state, it could be calibrated using Li^+ ions of known energy (see Chapter III).

The channel electron multipliers used in this research were Bendix Channeltrons, type 4010. A Channeltron has a pulse width of 20-30 nanoseconds and is capable of delivering 10^8 electrons for each detected particle when 3000 volts are applied to it. It was not necessary to operate the channeltron at full gain in this experiment. With about 2200 volts applied the multiplier output was significantly greater than the noise level. The output pulse was preamplified in an RIDL Model 31-14 Preamplifier. The pulse was then amplified in an RIDL Model 30-19 Linear Amplifier and Discriminator. The discriminator was typically set at one volt and provided an output pulse of +12 volts that was 0.5 μsec wide. For greater compatability with the data acquisition system which counts these pulses, the pulse was inverted, stretched, and amplified in a simple

circuit designed specifically for this purpose. The final negative pulse was slightly over 1.0 μsec wide and was 18 volts in magnitude. Optimum settings of detector voltage, electron extraction voltage, amplifier gain, and discriminator level were determined with the use of a low current Li^+ beam (less than 10^{-12} amps to prevent damage to the detector film). When the beam was on the detector, adjustments were made to maximize count rate and stability. The most important consideration was that the count rate not depend sensitively on the Channeltron gain since this can change somewhat during the experiment.[24] This dependence was checked easily by varying the amplifier gain and the discriminator level. The amplifier gain could be varied from 75 to 400 with less than one percent change in the count rate with the discriminator setting used. When the beam was aimed away from the detector, adjustments were made to reduce the noise count rate. Typical settings were 2200 volts on Channeltron, 100 volts for extraction, amplifier gain of 300, and a one volt discriminator level. The noise rate was less than 0.2 counts per second. Once the proper settings were determined, they were fixed for the entire experiment. The calibration of the CSI detector was made with these particular settings.

Energy Analyzer

The most important detector of this experiment was the energy analyzer shown schematically in Figure 9. It was a 127 degree electrostatic analyzer. A channel electron multiplier operated in the pulse mode was at the output of the analyzer. The analyzer was capable of energy resolution of better than one percent and has less than 0.1 noise counts/sec.

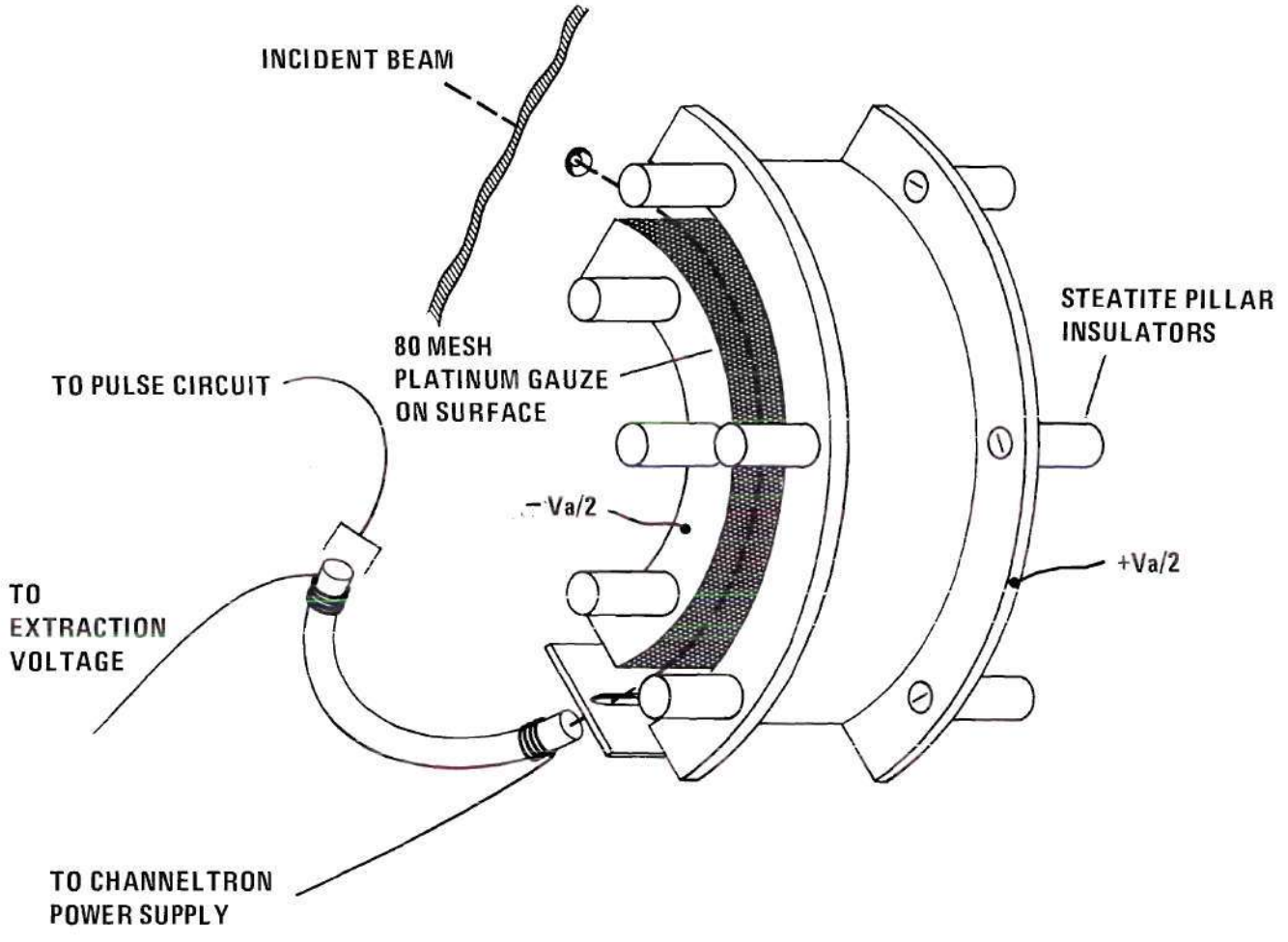

Figure 9. Energy Analyzer

Analyzer Construction

The analyzer plates were cylindrical with radii of 2 9/16 and 2 7/16 inches. These plates were machined from solid stainless steel to obtain maximum precision and strength. Each plate was 1 1/4 inches wide and was supported on each side by steatite pillar insulators. The insulators were shielded from the beam path by the sides of the plates. A large flat plate on either side of the analyzer supported the insulators. The entrance aperture had a 0.039 inch diameter which is the same as the small aperture Faraday cup and CSI detector. The distance from the target film to the entrance aperture was again two inches. The exit aperture was rectangular with a slit width of 1/32 inch. The multiplier was another Bendix Channeltron Electron Multiplier, type 4010. Both multipliers used in the experiment were powered by the same Fluke High Voltage DC Supply, type 413D. Not all particles that left the analyzer were captured by the multiplier since it had only a 0.039 inch opening. However, the loss of particles was more than compensated for by the reliability and low noise of the pulse counting technique. The output pulses were treated identically to those of the CSI detector and will not be discussed again.

Early calibration experiments showed the analyzer to have side lobes in the transmission function. The apparent cause was reflection of ions from the cylindrical plates. This effect was removed by lining the analyzer plates with 80 mesh platinum gauze made of interwoven circular wires. The wires in the gauze were crisscrossed with respect to beam path to minimize specular reflection into the multiplier.

The analyzing potential V_a was supplied by two Fluke High Voltage

DC Supplies, type 415. This voltage was also applied across a resistor chain to supply an analog readout to the data acquisition system. The value of resistance was set so that the data acquisition system read the energy E_o (in keV) for which the analyzer was tuned.

Theoretical Considerations of Electrostatic Analyzers

The transmission function, $g(E,E_o)$, is defined to be the fraction of particles of energy E which are passed by the analyzer that is tuned to energy E_o and detected by the Channeltron. Hughes and Rojansky[27] have shown that the width of the transmission function of a cylindrical electrostatic analyzer of 127 degrees is a linear function of the energy E_o. Appendix I shows that the integral, $G_E(E_o)$, of $g(E,E_o)$ should be a linear function of E_o. That is

$$G_E(E_o) \equiv \int_{-\infty}^{\infty} g(E,E_o)dE = kE_o \tag{4}$$

where k is some constant. Since the energy analyzer had a channeltron at the exit and not a Faraday cup, the function $G_E(E_o)$ might not depend exactly linearly on E_o. Since the function $G_E(E_o)$ was important for processing the results of this experiment, it was determined experimentally (see Chapter III).

The theoretical resolution, $\frac{\Delta E}{E}$, of the analyzer should be 1.25 percent. The proper definition for ΔE would be the full energy width for which g is not zero. If we define ΔE as the difference in energy values where the transmission function is only two percent of its maximum, the analyzer resolution was approximately 2.4 percent. However, as can be

seen from Figure 10, the resolution was about 1.5 percent if a ΔE that is the full width at half maximum is used. The analyzer constant, which is the ratio of the analyzer voltage V_a to the energy E_o of the beam which will optimally be transmitted, was found to indeed be constant to within $\pm$ 0.2 percent. Throughout the remaining discussion the value of energy E_o for which the analyzer is tuned will be referred to instead of the voltage V_a that is applied to the analyzer.

Scattering Region

The region between collimating plates and the region between the last collimating plate and the target film were field free regions. The region between the target film and the detector apertures has a small field present which should affect electron trajectories but not ion trajectories.

All of the high voltage leads for extraction and acceleration of the particles were shielded from the scattering region. All insulators were shielded by stainless steel shim stock. The only potential that was not shielded or held at ground potential was the potential on two electrodes located just in front of each Faraday cup's entrance aperture. These electrodes were used as secondary electron traps. A small positive potential of less than 90 volts was applied to these cylindrically shaped electrodes. This positive potential attracted secondary electrons generated on the back side of the target film and those generated on the detector aperture plate. With the positive potential applied, an increase of typically three to five percent was observed in the indicated positive current. A negative potential would be more conventional to suppress

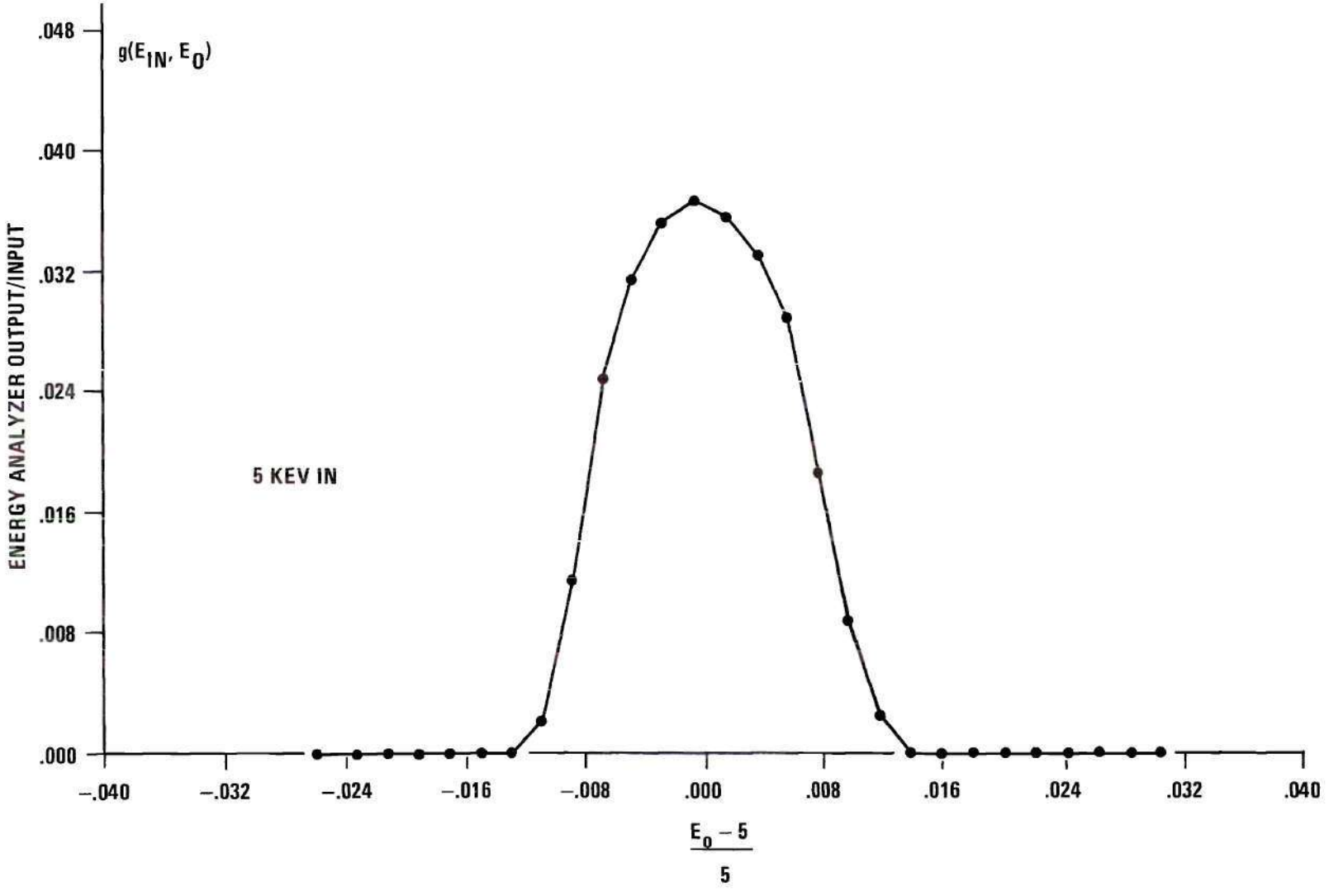

Figure 10. Typical Energy Analyzer Transmission Function
(Beam energy held constant at 5 keV and analyzer voltage varied.)

secondaries from the target film, but when this was tried, a small decrease of the measured (positive) current was sometimes observed. The largest source of secondaries seemed to be from the grounded detector aperture plate. It appeared that a negative suppression potential would actually repel some of the secondaries from the plate back into the aperture. A first approximation to the field seen by ions that have emerged from the target was one which was radial and thus would not steer the particles. Also the potential was so small compared to the energy of the ions that it was assumed not to affect the ion trajectories.

There were two small horizontal parallel plates located near the target film. These plates were used only during calibration, when the target film had been removed from the beam path, to deflect the beam vertically and verify that it was directed straight into the detectors. It also served to check the vertical alignment of the source. These electrodes were held at ground potential when the film was in the path of the beam. They were covered with the 80 mesh platinum gauze to reduce erroneous specular reflections into a detector.

Data Acquisition System

The data acquisition system monitored all of the electrical signals and recorded channel identification and signal value. The data in this experiment had to be obtained very quickly before the bombardment of lithium particles changed the film characteristics significantly. This would have been impossible to achieve without a data acquisition system. Also this experiment generated a great deal of data. It would have been most inconvenient to have punched computer cards for all of it.

The system used was a Hewlett Packard Model 2010L Data Acquisition System. It consisted of an input scanner, an integrating digital voltmeter, a coupler, and a teleprinter. Four dc voltages and two pulse signals were monitored by the system. The four dc signals were the energy E_o for which the energy analyzer was tuned, the angular readout signal, and the recorder outputs of the two vibrating reed electrometers, which were connected to the Faraday cups. Since the voltage accuracy of the system was 0.01 percent of the reading, the electrical error in angle and energy determinations was insignificant compared with the errors due to the finite size of the aperture and resolution of the analyzer. The vibrating reed electrometers were linear amplifiers so the electrical error was that of the feedback resistors which were either 1.0 or 2.0 percent.

Sample periods of 0.01, 0.1, and 1.0 seconds were available using the data acquisition system's internally generated frequency of 100 kHz. With the use of an external frequency of 1 kHz, sample periods of 1.0, 10.0, and 100.0 seconds were available. This latter mode of operation was adopted since the speed of the system was already limited by the teleprinter to times greater than 1.0 sec, and the longer sample periods greatly reduced the number of data points that had to be taken to eliminate statistical fluctuation. The external frequency was supplied by a Hewlett Packard Audio Oscillator, type 200AB. The frequency was adjusted to 1 kHz $\pm$ 0.002 percent with the digital voltmeters internal plus and minus 1.0 volt references. That is, the frequency was adjusted until the 1.0 volt standards read 1.00000 $\pm$ 0.00002 volt. The oscillator was allowed to warm up for over two weeks and then found to be stable to 0.005 percent per week.

The digital voltmeter was also capable of counting pulses. This mode was used to monitor pulse signals from the channel electron multipliers that were part of the energy analyzer and CSI detectors. Since these detectors were calibrated with a Faraday cup, the only error due to the electronics was the error in time scale which was less than 0.01 percent.

The teleprinter reproduced the acquired data on typewritten pages and punched tape. The punched tape was read into the Univac 1108 computer by the optical reader. Programs were written to decode and process the resulting data.

CHAPTER III

PROCEDURES AND RESULTS

This research can be separated into several related experiments. Each of these with their results will be described in this chapter.

A brief description of the procedure follows. The energy analyzer and CSI detector were calibrated. For each input energy the energy distribution of charged particles was determined at scattering angles of 0, 5, 10, 20, 30 degrees and at one or more of the angles of 40, 50, and 60 degrees. The ratio of charged particles to total particles transmitted through the films was then determined as a function of the emergence energy by an iteration procedure. Since the condition of the surfaces of the films was not carefully controlled, the ratio obtained was of value only as it applied to this experiment. It was used to convert energy distributions of the charged particles to the energy distributions of all (charged and neutral) particles emerging from the film. For each input energy the fluxes of charged particles and of all particles was determined as a function of angle. Several experimental checks were made for consistency and accuracy. Finally, the energy losses were calculated from the above determined data. Each of the above steps, their results, and estimated errors will be discussed in detail in the remainder of this chapter.

The least known parameter of this research was the film thickness in mass per unit area. To minimize this effect on the data, all of the

final data were taken on the same carbon film. Since the thickness was the same for all data, it affects the data as a single constant. Early in the experimental work it was found that the films change their characteristics with bombardment time. To minimize this effect the data were taken as rapidly as possible. Also different portions of the film were used for experiments that were not too closely related. All particle flux and energy distribution measurements for a particular input energy were made using the same portion of the film.

Initial Experiment Checks

Several initial checks were necessary before data could be taken. These were concerned primarily with the operation of the source. The adequacy of operation of the energy analyzer and CSI detector was determined during their calibration which is described later in this chapter.

Source Stability

The most important check was the source stability. After the filament had been on and current extracted for a long enough period to remove all impurities (see Chapter II), a four hour stability check was made. If the current varied more than ± 2 percent, the filament was allowed to continue aging. The stability run was made using the magnitude of current to be used in the experiment since varying the temperature of the filament often led to temporarily unstable outputs. Additional one hour stability checks were repeated many times before and after data runs. Since the input beam current could not be monitored while a film was in the beam path, these stability checks provided important estimates of experimental errors due to source current changes.

Source Alignment

The vertical alignment could not be changed after the apparatus had been placed in the vacuum chamber. In order to determine the amount of error in this alignment, the beam was steered into each detector aperture with the source rotation mechanism and vertical electrostatic deflection plates. When the output of the detector had been peaked, the vertical deflection was calculated from the voltage applied to the deflection plates. In all cases it was found to be less than 0.1 degree.

For the computer program to convert the signal output of the angular potentiometer into the angle between the source direction and a given detector, it was necessary to know the electrical output corresponding to the source being aimed directly into that detector. The source was rotated horizontally across the detector and the output was recorded and plotted. Typical scans are shown in Figure 11. The point centered between the half maximum points was selected as the zero angle. The deflection voltage used during the above scans was that required to center the beam vertically on the detector. The beam was usually the same approximate size as the detector aperture so that the results of these scans included the effects of the finite beam dimensions. Such curves allowed the combined angular resolution to be determined directly. For the large aperture Faraday cup the combined resolution was $\pm$ 2 degrees, and for all other apertures it was about $\pm$ 1 degree. The flat region of the large aperture cup indicates that the beam was entirely inside the detector aperture there. Hence this cup can be used to accurately measure the total output current of the source. The variations in the CSI detector curve are thought to be due to the grid wires used to support the detector film.

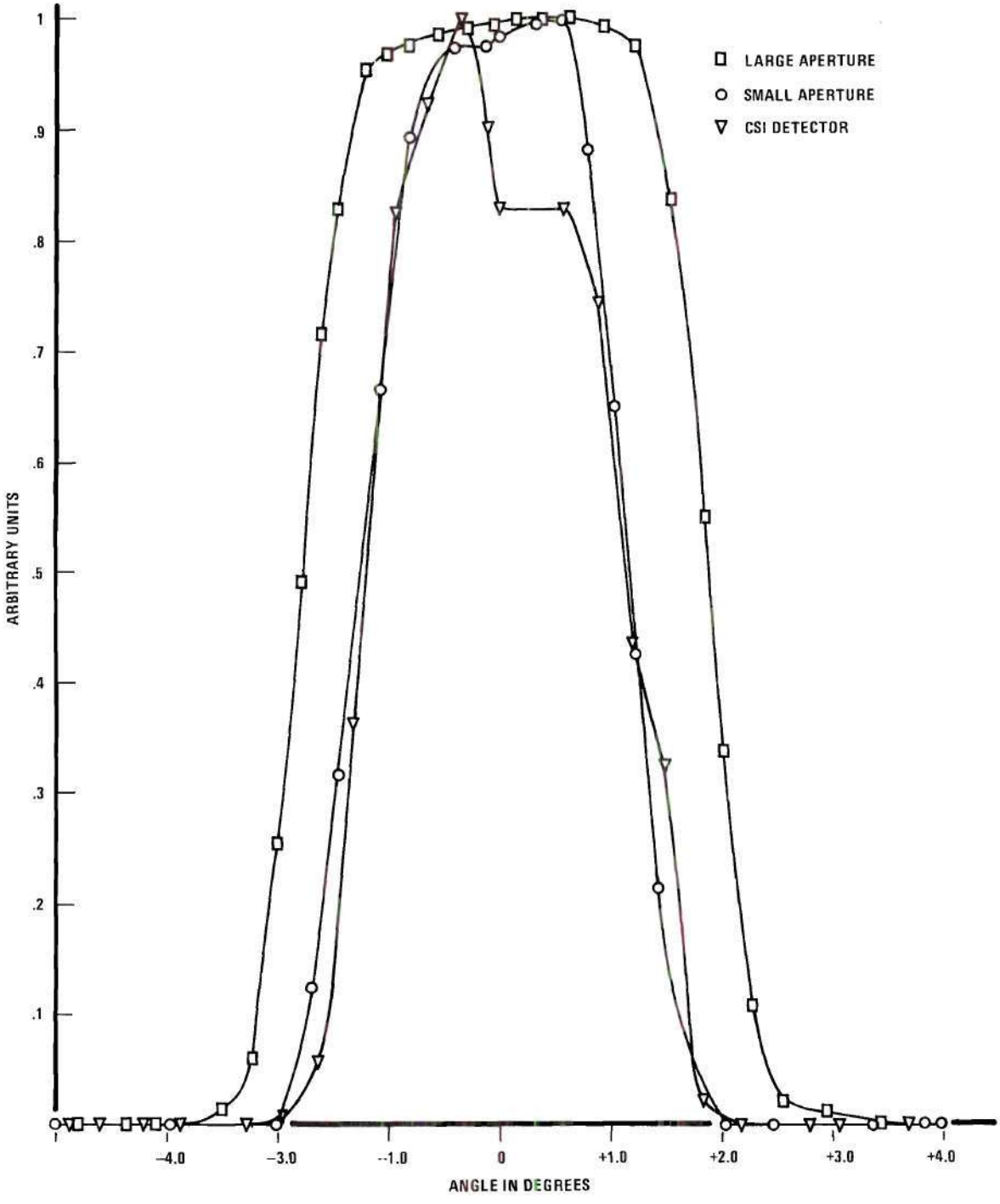

Figure 11. Typical Angular Scans Across Detectors (Detector outputs normalized to maximum value of one. Angle in degrees.)

It was found that the zero angle readings changed slightly (less than 0.1 degree) for different acceleration and extraction voltages. Therefore the zero angles were determined before each data run with the acceleration voltage and extraction voltage to be used in that run.

For the program to convert electrical readings into degree readings, a conversion factor was needed. This was usually determined by changing the angle of the source by 67.5 degrees (three complete rotations of the external rotation mechanism) and dividing 67.5 degrees by the magnitude of the difference in the electrical readings. This ratio was calculated before each angular scan to determine particle fluxes was made. This factor changed by less than 0.5 percent over a period of five months.

Calibration of Energy Analyzer

The energy analyzer was used to determine the energy distribution of Li^+ particles, $f_\theta(E)$, that emerge from the film at the angle θ. The output of the energy analyzer, $I_E(E_o,\theta)$, that is tuned to the energy E_o is given by

$$I_E(E_o,\theta) = C(\theta)\Delta\Omega_E \int_{-\infty}^{\infty} g(E,E_o) f_\theta(E)\,dE \qquad (5)$$

where $\Delta\Omega_E$ is the small solid angle subtended by the energy analyzer, $C(\theta)$ is the Li^+ flux (per steradian) at the angle θ, $g(E,E_o)$ is the transmission function of the analyzer tuned to energy E_o for charged particles of energy E, and $f_\theta(E)$ is in units of $(keV)^{-1}$. The analyzer was calibrated by the procedure described below.

Procedure

With the film removed from the beam path, an Li^+ beam of about 10^6 particles per second was directed into the small aperture detector. The beam had a well defined energy E_{in} so that $f_\theta(E) = \delta(E - E_{in})$ where δ is the familiar Dirac delta function. Since $\Delta\Omega_E$ was the same as the solid angle subtended by the small aperture Faraday cup, $\Delta\Omega_S$, Equation 5 yields

$$g(E_{in},E_o) = \frac{I_E(E_o,0)}{I_S(0)} \tag{6}$$

where $I_S(0)$ is the particles per second measured by the small aperture Faraday cup with the beam directly into the cup. The voltage on the analyzer plates was varied to change the energy E_o for which the analyzer was tuned. For each fixed input energy a curve was obtained of $g(E_{in},E_o)$. The value of $G_E(E_o)$ which is the integral of the curve $g(E,E_o)$ with respect to the particle energy E was desired. Appendix I shows that

$$G_E(E_o) = \int_{-\infty}^{\infty} g(E,E_o)dE = \int_{-\infty}^{\infty} g(E_o,E_o')dE_o' \tag{7}$$

Therefore, $G_E(E_o)$ was obtained by integrating the function obtained by varying E_o with a fixed input energy. Input energies of 1, 2, 3, 4, 5, 6, 7, 8, 9, and 10 keV were used. The values of $G_E(E_o)$ for all $E_o \leqq 10$ keV was obtained by a mean square fit of a linear function of E_o to the data points. The results are shown in Figure 12 and are discussed below.

Results

The experimentally determined data points (x's in Figure 12) agree

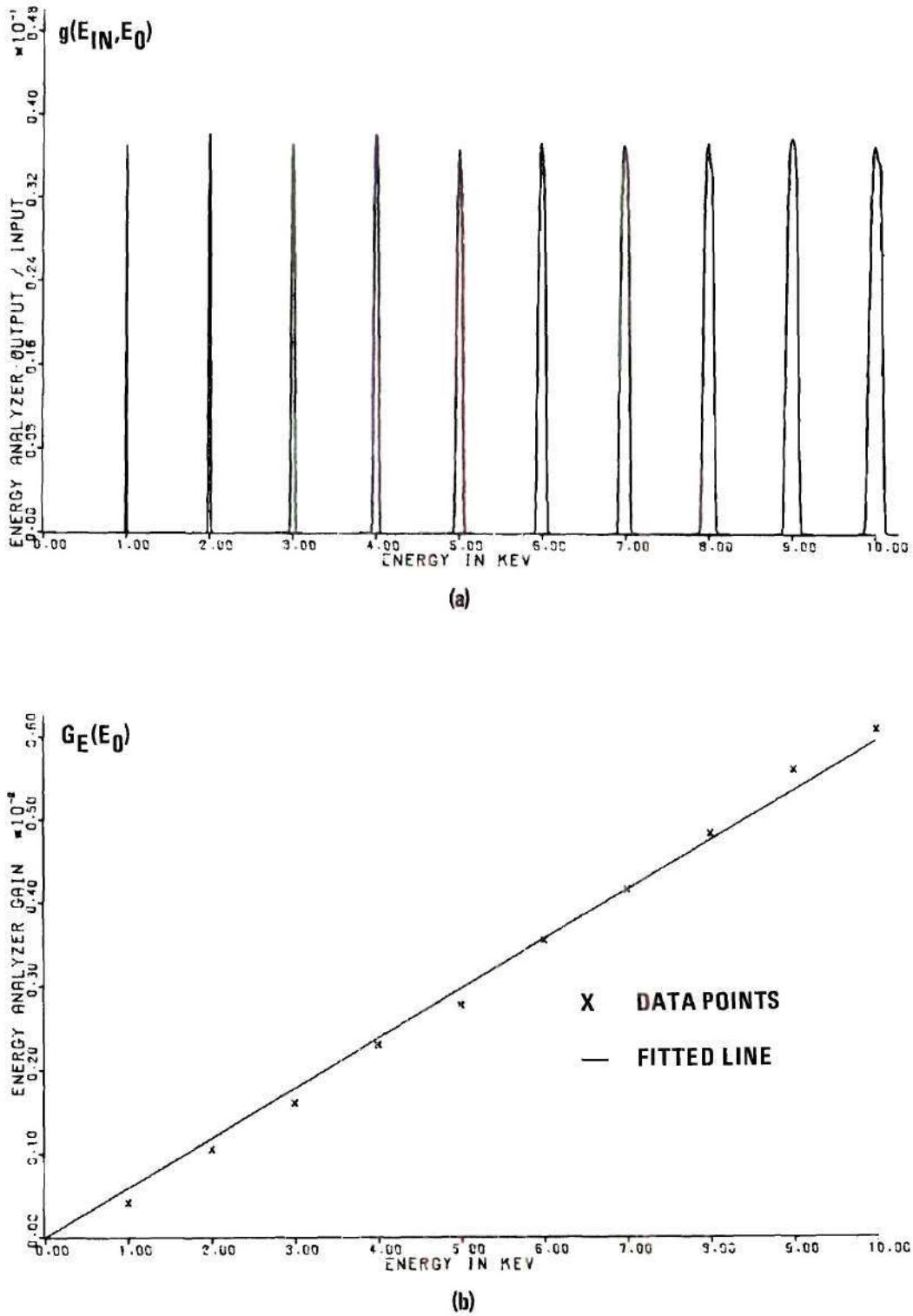

Figure 12. Energy Analyzer Calibration
(a) Analyzer Output Divided by Input
(b) Calibration Curve

with the linear theoretical curve within ± 7 percent above 2.0 keV. The experimental error of the calibration was estimated to be ± 10 percent for energies ≧ 2.0 keV. The main source of error was in determining the input current to the analyzer and the solid angle subtended by the analyzer entrance aperture. At 1 keV the experimental point is about 30 percent below the fitted line. For this energy the source gave a broader beam which may have been focused somewhat. Several different determinations of this value showed it to be consistently 20 to 35 percent below the line.

The linearity of the curve has thus been verified for energies ≧ 2.0 keV. The magnitude of the multiplying constant has been determined to within ± 10 percent. For this research most of the transmitted particles had energy above 2.0 keV. Therefore, the value of $G_E(E_o)$ was not very important below 2.0 keV. The magnitude of the constant will be shown later to be unimportant, but the shape (linearity) was quite important.

Charged Particle Energy Distributions

The charged particle energy distributions $f_\theta(E)$ were obtained from the energy analyzer. From Figure 10 or Figure 12 it can be seen that

$$g(E,E_o) = 0 \quad \text{for } |E - E_o| \geqq \alpha \tag{8}$$

where α is much smaller than E_o. The value of α is approximately $E_o/100$. If $f_\theta(E)$ is constant in the interval $[E_o - \alpha, E_o + \alpha]$ or if it varies slowly (see Appendix II) in that interval, Equation 5 becomes

$$I_E(E_o,\theta) = C(\theta)\Delta\,\Omega_E f_\theta(E_o)G_E(E_o) \tag{9}$$

which can be solved for $f_\theta(E_o)$ to obtain

$$f_\theta(E_o) = \frac{1}{C(\theta)\Delta\,\Omega_E} \frac{I_E(E_o,\theta)}{G_E(E_o)} \tag{10}$$

Since

$$\int_{-\infty}^{\infty} f_\theta(E_o)dE_o = 1 = \frac{1}{C(\theta)\Delta\,\Omega_E} \int_{-\infty}^{\infty} \frac{I_E(E_o,\theta)}{G_E(E_o)}\, dE_o \tag{11}$$

we have that

$$C(\theta)\Delta\,\Omega_E = \int_{-\infty}^{\infty} \frac{I_E(E_o,\theta)}{G_E(E_o)}\, dE_o \tag{12}$$

Substitution of Equation 12 back into Equation 11 gives

$$f_\theta(E_o) = \left[I_E(E_o,\theta)/G_E(E_o)\right] \Big/ \int_{-\infty}^{\infty} \left[I_E(E_o,\theta)/G_E(E_o)\right] dE_o \tag{13}$$

This equation was the basis for the determination of the energy distributions of Li^+ emerging from the film. The experimental procedure and some typical results are given below. Complete results are given in Appendix III.

Procedure

With the desired acceleration voltage applied to the source and the film removed from the beam path, the output beam current was adjusted to approximately 0.5×10^{-10} amps into the large aperture Faraday cup. The steering electrodes were grounded, and the target plate moved into position so that the beam passed through the thin carbon film. The source was then aimed at the analyzer. The analyzer voltage was varied so that

the energy for which it was tuned, E_o, varied from the input energy of the incident beam down to about 0.5 keV. Data were taken at each selected value of E_o. Before the small value of 0.5 keV was reached, the output of the analyzer usually had gone to zero. Since the peak of the curve is the most important region, more data points were taken in that region. The entire file of data was recorded on the punched paper tape of the data acquisition system. After the scan was completed at zero degrees, the source was rotated to obtain scans at 5 degrees, 10 degrees, 20 degrees, and other larger angles. The counting period used for a data point was selected so that the total counts that represented the peak value on the curve was between 10^3 and 10^4 counts. This was sufficient to reduce statistical fluctuations to less than one percent of the peak reading. The same counting period was used for all data at a given angle. The counting time for small angles of 0, 5, and 10 degrees was typically 10 seconds while for larger angles 100 second counting times were necessary. Since the films will change their characteristics with bombardment time, it was necessary to take the scans as rapidly as possible. Therefore, for the larger angles fewer data points could be taken. Data points were taken at closer intervals near the peak of the curve to insure that the peak value was determined.

Finally, to insure that the film had not changed its characteristics during the bombardment, a check scan was made at one of the small angles. Sometimes this scan was made at a negative value of the earlier angle used to insure angular symmetry. Small angles were used for checking purposes since scans could be made more rapidly there and the char-

acteristics of the film at the end of bombardment could be compared with those near the beginning.

For a different value of the input energy of the ion beam, a different portion of the film was used, and the entire procedure described above was repeated. All of the data were entered on the Univac 1108 computer. Charged particle energy distributions were determined as indicated in Equation 13. The trapezoidal rule was used for all numerical integrations.

Results

Figure 13a shows a typical analyzer output for a large angle. The x's are the data points and they have been connected by straight lines. Figure 13b is the energy distribution determined from the data in 13a. A large angle was selected to illustrate the correction since the effect is more pronounced for curves which have a greater spread. Figure 14 includes all the Li^+ distributions determined for 8 keV input energy. Again the symbols indicate data points which have been connected by straight lines. Tables of these data and curves and tables for other input energies are presented in Appendix III. For 8 keV input energy, distributions were determined at 0, 5, 10, 20, 30, 40, and 60 degrees. Check curves were made at 0 and 5 degrees. These check curves show the excellent repeatability of the data and indicate that the ion bombardment of about 5.5 hours has not affected the energy loss characteristics of the film. For all other input energies only one check curve was made at the end of the data run.

The primary sources of error are fluctuations of input current and

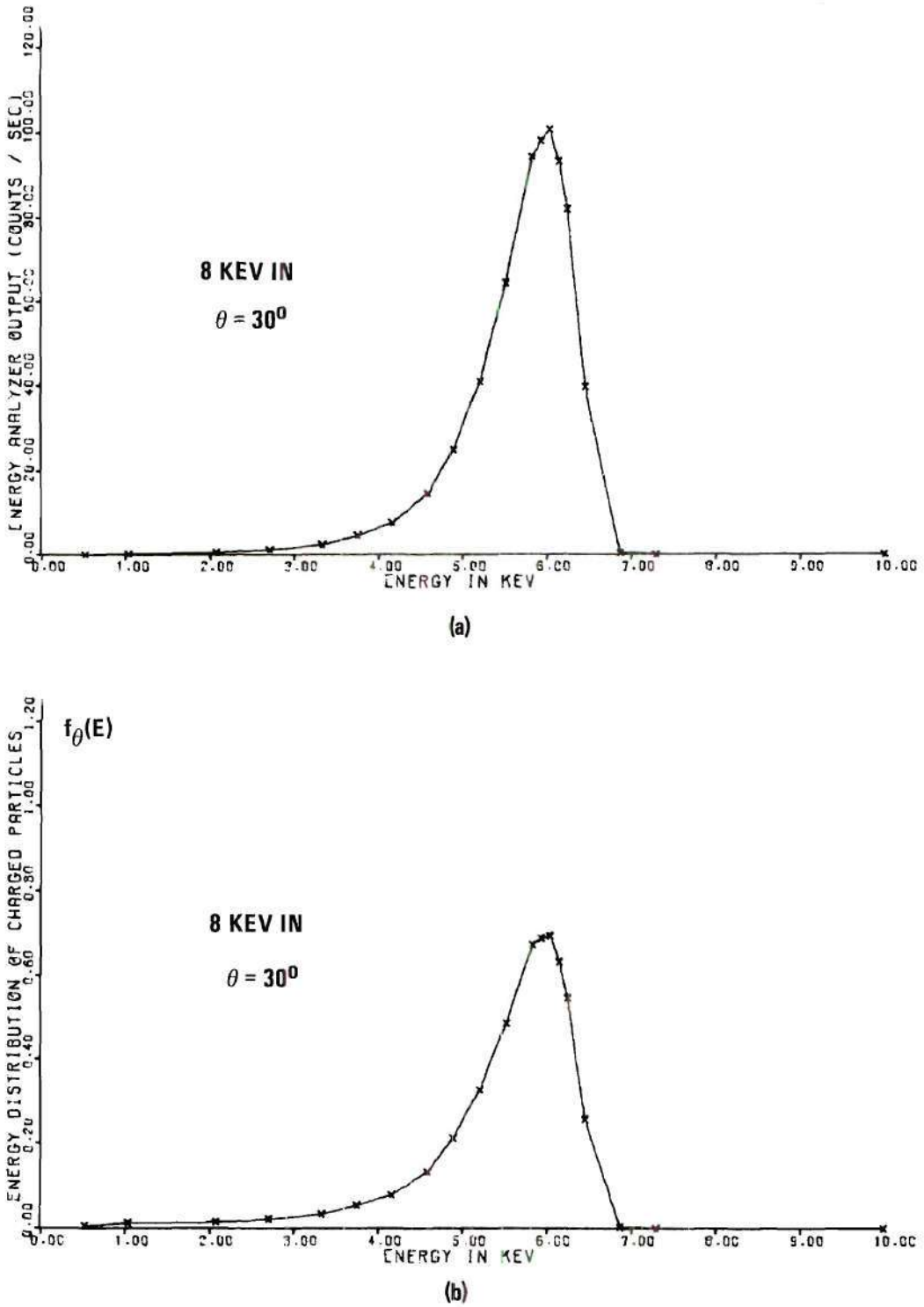

Figure 13. Analyzer Correction
(a) Typical Analyzer Output
(b) Output Corrected by $G_E(E_o)$ and Normalized

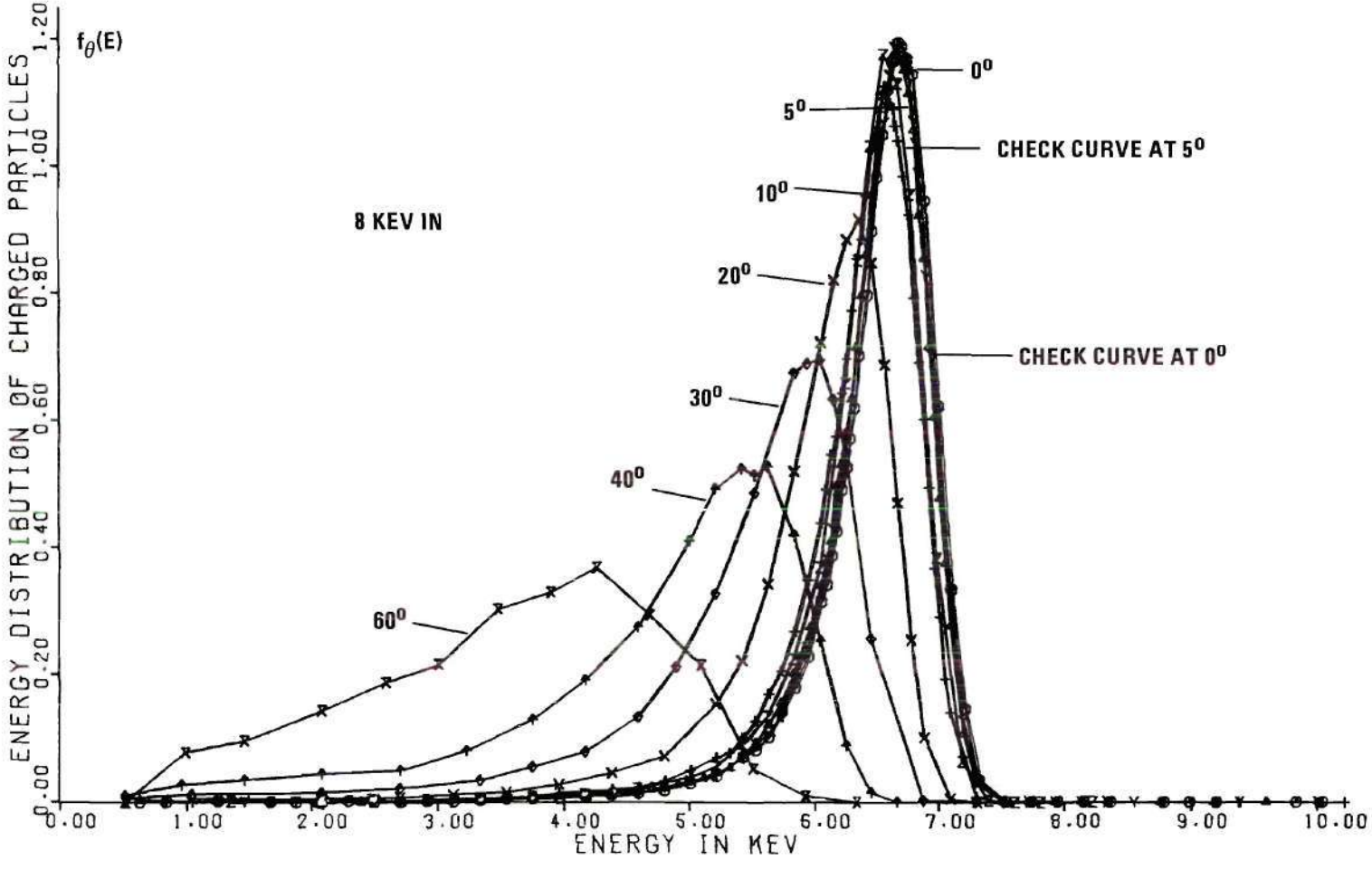

Figure 14. Energy Distributions of Li^+ for 8 keV Input

the statistical nature of the process itself. Source instability dominates when the signal levels are large and the statistical fluctuation dominates for small signal levels. A consideration of these error sources led to an estimated uncertainty in the distributions of $\pm$ 0.04 $(keV)^{-1}$. That this measurement was almost completely free of noise was indicated by the zero values measured above 7.5 keV. Systematic errors as in solid angles, electrometer resistor determinations, and magnitude of $G_E(E_o)$ constant can be seen to cancel in Equation 13. The numerical integration error was assumed negligible compared to the random errors previously mentioned.

Calibration of the CSI Detector

The CSI detector was used to determine the total flux of Lithium particles per steradian, $T(\theta)$, in this experiment. A detector which did not depend on charge state was also essential to determine the ratio of charged particles to total particles as a function of energy. The output, $I_T(\theta)$, of the CSI detector is given by

$$I_T(\theta) = T(\theta)\Delta\,\Omega_T \int_{-\infty}^{\infty} G_T(E)\,p_\theta(E)\,dE \qquad (14)$$

where $\Delta\,\Omega_T$ is the small solid angle subtended by the CSI detector, $G_T(E)$ is the detection efficiency of lithium particles of energy E, and $p_\theta(E)$ is the energy distribution of all (charged and neutral) particles at the angle θ. This detector was calibrated by the procedure described below.

Procedure

The Li^+ pencil beam was aligned on the large aperture detector.

No film was in the path of the beam. The beam current was selected by varying the filament temperature. A value near 5×10^{-12} amps was typical. The beam was essentially monoenergetic with energy E_{in} so it was assumed that

$$p_{\theta}(E) = \delta(E - E_{in}) \tag{15}$$

Substitution of the above equation into Equation 14 and interpretation of $T(\theta)\Delta\,\Omega_T$ as the current measured in the large aperture detector gives

$$G_T(E_{in}) = \frac{I_T(0)}{I_L(0)} \tag{16}$$

where $I_T(0)$ was determined by aligning the beam on the CSI detector. $G_T(E_{in})$ was determined at 10, 9, 8, 7, 6, 5, 4, 3, 2, and 1 keV by the above procedure. Values between these points were determined by linear interpolation.

Unfortunately the above procedure gives only a relative calibration of the CSI detector. The number of particles per second into the CSI detector, $T(\theta)\Delta\,\Omega_T$, was not the same as the total particles per second in the Li^+ beam because the beam was larger than the detector opening. Subsequent measurements with the large and small aperture Faraday cups have shown the ratio of currents measured in these cups to be constant for source energies that are greater than or equal to 2 keV. However, the measurement at 1 keV showed that due to beam spreading a smaller value would have entered the small aperture of the CSI detector. The relative calibration as determined by Equation 16 was made absolute by correcting

$I_L(0)$ by the above determined factors.

Results

The results of the calibration by the above procedure are shown in Figure 15. This procedure leads to a fairly large estimated possible error of ± 20 percent for $E_{in} \geq 2.0$ keV and ± 50 percent of the value at 1.0 keV. Subsequent calibrations were made using the small aperture current directly as the current into the CSI detector. These were therefore more accurate but were made after changes had been made in the detector film and Channeltron placement. $G_T(E)$ depends on the placement of the Channeltron, the thickness of the detector film used, and perhaps on the surface condition of the film. Therefore, it was necessary to use the calibration that was made during the same vacuum pumpdown for which the data reported in this research were taken.

Above 2.0 keV the primary errors are the systematic errors in the solid angles, $\Delta \Omega_S$ and $\Delta \Omega_T$, of ± 5 percent each and the electrometer resistor determinations of ± 2 percent. Added to these are source instability of ± 2 percent for each of the four current measurements and random noise of the Channeltron of less than one percent. At one keV the largest error contribution was the random error in determinations of the ratio of particles into the two Faraday cups. This error was due to the different beam spread of the source at 1.0 keV for different filament temperatures and extraction voltages.

Ratio of Positive Particles to Total Particles

The ratio of Li^+ to total lithium particles (No significant amount of Li^{2+} or Li^{3+} was expected. See results below.) which have passed

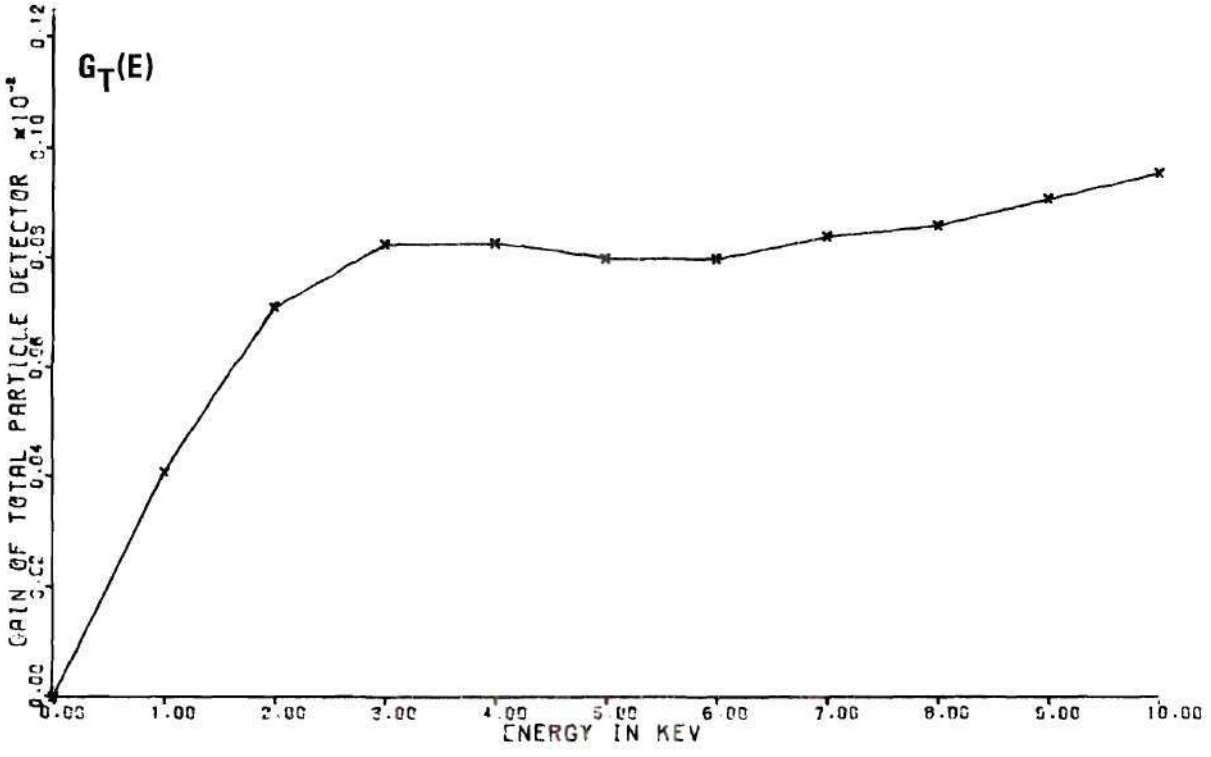

Figure 15. Calibration of CSI Detector

through the carbon film was expected to be a function of energy. This function, denoted by R(E), related the energy distributions of positive particles to the energy distribution of all lithium particles. Hence it was necessary to determine this function to obtain the energy distributions of all particles, $p_\theta(E)$, from the distributions of the charged particles, $f_\theta(E)$. The ratio is expected to depend very sensitively on the surface condition of the films. The objective of this portion of this research was not to obtain generally valid results for R(E), but to obtain R(E) for the film used with its particular surface condition.

The relationship between $f_\theta(E)$, $p_\theta(E)$, and R(E) can be seen in the following equation

$$C(\theta)f_\theta(E) = R(E)T(\theta)p_\theta(E) \tag{17}$$

All terms have been defined previously. Each side is the flux of Li^+ (per steradian) in an increment dE about E. If R(E) were independent of the energy, then obviously $f_\theta(E)$ and $p_\theta(E)$ would be identical as has been assumed by others.

Dividing both sides of Equation 17 by $C(\theta)R(E)$, integrating over all energies, and using the fact that the integral of $p_\theta(E)$ is unity yields

$$\int_{-\infty}^{\infty} \left[f_\theta(E)/R(E) \right] dE = T(\theta)/C(\theta) \tag{18}$$

Substituting the above integral into Equation 17 and solving for $p_\theta(E)$ gives

$$p_\theta(E) = \left[f_\theta(E)/R(E) \right] \Big/ \int_{-\infty}^{\infty} \left[f_\theta(E)/R(E) \right] dE \qquad (19)$$

Equation 19 is the basis of the procedure used to determine $p_\theta(E)$ after R(E) was determined. The procedure described below was used to determine R(E) at small scattering angles.

Procedure

The target plate was moved so that a portion of the film that had not been bombarded previously was in the ion beam path. The steering electrodes were grounded, and the source was directed to the zero angle of the large aperture detector to determine C(0). The source was then turned to the zero angle of the CSI detector, and its output, $I_T(0)$, was recorded. Finally, the source was placed at the zero angle of the energy analyzer and $f_0(E)$ was determined in the manner previously discussed. The above procedure was carried out for input energies of 10, 9, 8, 7, 6, and 5 keV input energies. All of the above data were entered on the computer and processed as described below.

For all of this data the angle was fixed at zero degrees and the incident energy was varied. Hence the variable θ will be suppressed in the notation in this section. The subscript i which indicates different input beam energies is added. Dividing both sides of Equation 17 by T_i and integrating over all energies yields

$$C_i/T_i = \int_{-\infty}^{\infty} R(E) p_i(E) dE \approx R(E_i) \qquad (20)$$

where E_i is the average energy of all lithium particles emerging at zero

degrees. The last approximation is valid if R(E) is "smooth."[28] This approximation is more accurate when the standard deviation of the distribution is small. The zero degree distributions were used since they have smaller standard deviations than larger angle distributions. For distributions with small standard deviations, a rough approximation is

$$p_i(E) \approx f_i(E) \tag{21}$$

This is the starting point of the iteration procedure which was used to determine R(E). Solving Equation 14 for T_i gives

$$T_i = I_T(i) \Big/ \left[\Delta \Omega_T \int_{-\infty}^{\infty} G_T(E) p_i(E) dE \right] \tag{22}$$

The definition of E_i is

$$E_i = \int_{-\infty}^{\infty} E p_i(E) dE \tag{23}$$

In Equations 22 and 23 all terms on the right hand side were known except $p_i(E)$. Equation 21 was first assumed to be valid. T_i and E_i could then be determined. They were tentatively determined at each of the input energies. These values were used in Equation 20 to obtain approximate values of R(E) at six points. A first order polynomial was mean square fitted to these points and used to calculate more accurate $p_i(E)$'s from Equation 19. These more accurate total particle distributions were then used to calculate T_i's and E_i's again, which were used to calculate a more accurate R(E) curve. This iteration procedure was continued until

the values of R changed by less than five percent of their previous value. For the present data this took only two iterations.

Results

A first order polynomial (linear and constant terms) was found to give a very good fit. In fact R(E) was almost constant. Figure 16a shows the $f_i(E)$ curves used in the determination of R(E). Figure 16b shows the corresponding $p_i(E)$ curves which were the result of the iteration procedure described above. If any significant amount of Li^{2+} or Li^{3+} were present, they would appear as peaks at 1/2 and 1/3 of energy values corresponding to the energy values of the peak in these distribution curves. No such peaks were found. The numbers above the curves give the input energy for that curve. Figure 17 shows the values of R(E) determined by the procedure described above.

As can be seen from Figure 16, input energy values of 4, 3, and 2 keV were also used. Their use was an attempt to determine R at energies less than 3.0 keV. They were made on a different area of the film than that used for the higher energy values. Their three points were above the fitted curve by about 20 percent. The difference in these experimental values and the fitted line is within the absolute error expected. However, the relative error was not expected to be larger than 12 percent except for the lowest energy value where the random error in $G_T(E)$ was very large. One plausible explanation is that R(E) for lithium is relatively independent of energy for 2 to 10 keV particles, but depends so sensitively on surface effects that two different areas of the same film have different ratios (R). The only known charge state study for lithium

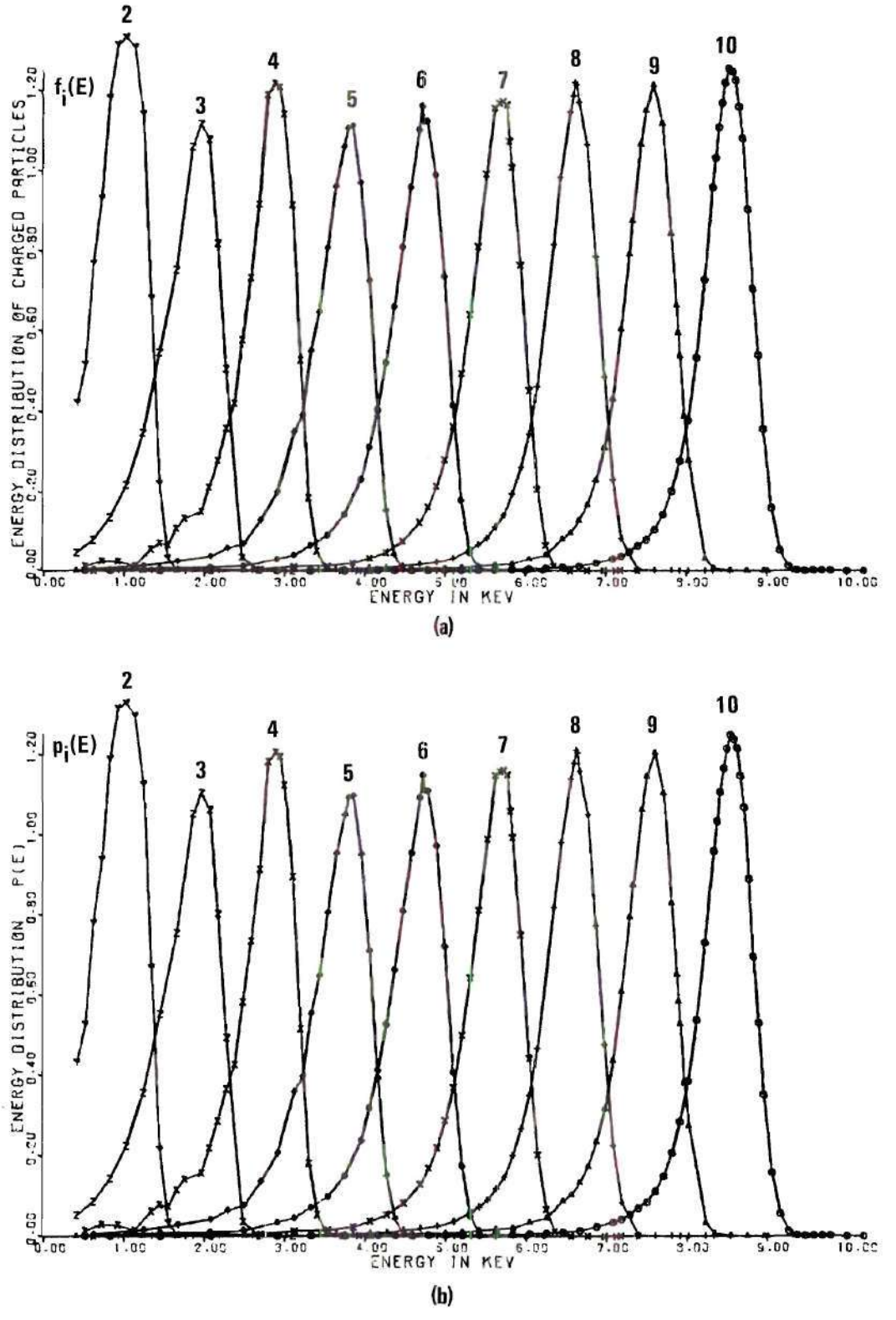

Figure 16. Energy Distributions Used to Determine R(E)
(a) Li^+
(b) All Lithium

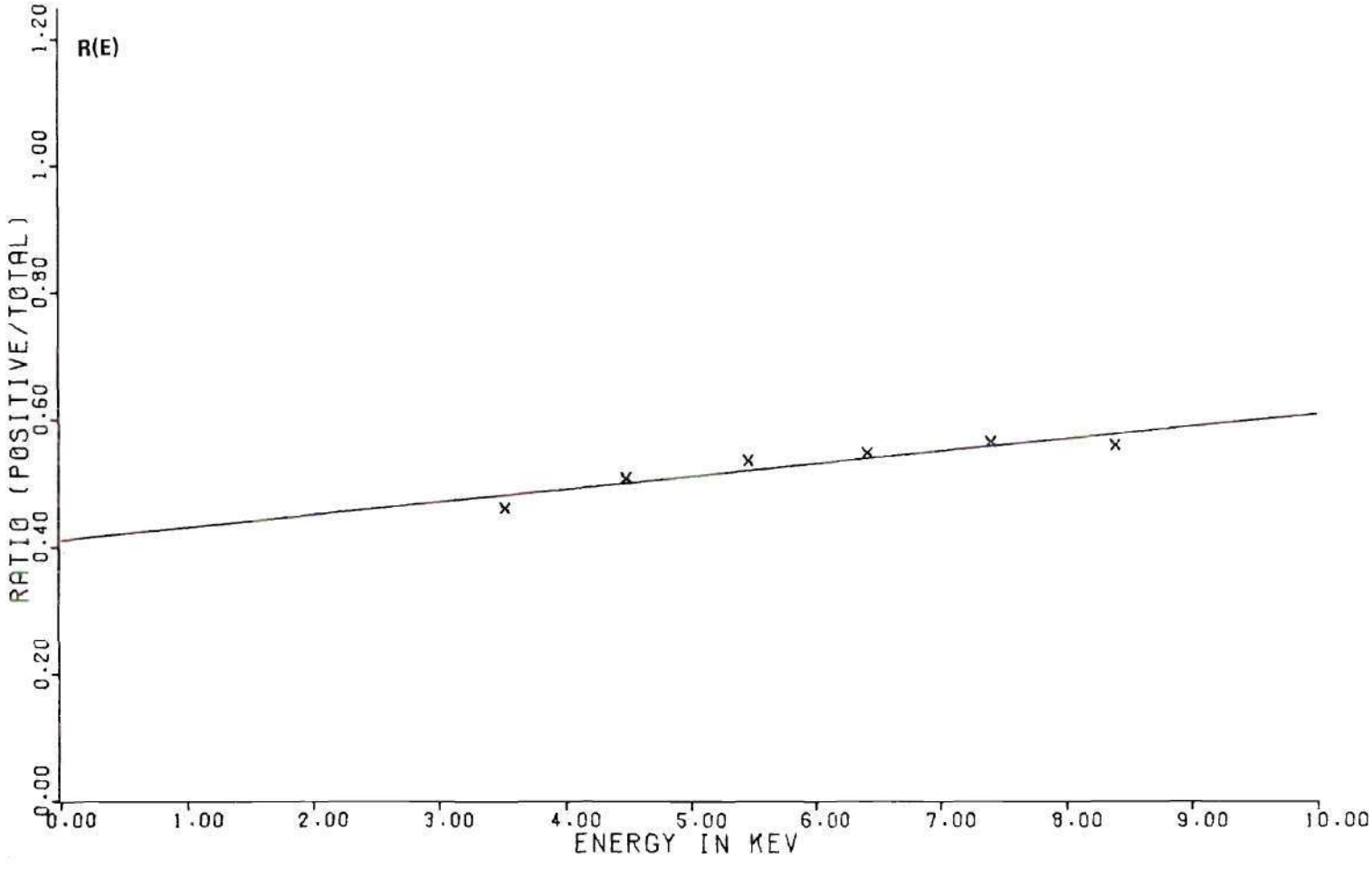

Figure 17. Energy Dependence of the Ratio of Charged Particles to Charged and Neutral Particles

emerging from thin films in this energy range is that of Bethge and Fabricus.[29] Interpretation of their results supports the above possible explanation. The equilibrium fractions determined by Allison et al.[30] for lithium in hydrogen gas for energies above 20 keV supports the energy independent concept. Since the relative energy dependence of R(E) and not its absolute magnitude is important in determining $p_\theta(E)$ (see Equation 19), the data below 3.0 keV was ignored for the curve fitting.

The principal source of error is the ± 20 percent error in the determination of $G_T(E)$ previously discussed. Another error of ± 5 percent is possible in the determination of the solid angle of the large aperture Faraday cup. Source instability contributes a possible random error of ± 2 percent each in the measurement of $C_i(0)$ and $I_T(i)$. Therefore, the relative determination above 3.0 keV should be accurate to ± 12 percent, and the absolute values should be accurate to within ± 30 percent. The values of R for energies below 3.0 keV should still be within the absolute uncertainty, but the relative uncertainty may have increased. This point will be discussed again later in this chapter when the consistency checks are considered.

Total Particle Energy Distributions

The determination of the energy distributions of all (charged and neutral) particles transmitted was discussed in connection with determining R(E). There $p_i(E)$'s were determined at a single angle in order to determine R(E). An iteration procedure was used with a reasonable first guess of the distribution. Since R(E) and $f_\theta(E)$ had been determined,

$p_\theta(E)$'s were determined using Equation 19 with no iterations necessary. R(E) has been written with no expressed angular dependence. An angular dependence is not expected for the amorphous films used. If there were an angular dependence and if a separation of variables were possible, that is

$$R(E,\theta) = R(E)\,\Theta(\theta) \tag{24}$$

this dependence would not affect the value of $p_\theta(E)$ as can be seen immediately by substituting Equation 24 into Equation 19. Therefore, the value of R(E) determined at zero degrees was used to determine $p_\theta(E)$ for all angles at which charged particle energy distributions had been determined.

The total particle distributions for eight keV input energy are shown in Figure 18. Tables of these values are given in Appendix III along with curves and tables for 10, 6, and 4 keV input energies. The curves shown here are for the same angles as in the Li^+ energy distributions. These results have all of the possible errors present in the Li^+ distributions. Also the error in the relative determination of R(E) is present. Systematic errors in the absolute determination can be seen to cancel in Equation 19. The same area of the film was used for all input energies so a change in the value of R(E) that depends on the area of the film used would not affect these results. Therefore, it appears that an additional error of ± 12 percent of the value is sufficient to account for the errors due to R(E) determinations. However, this cannot be conclusively established for emergence energies less than 3.0 keV. Particles with emergence energies less than 3.0 keV represent a small fraction of

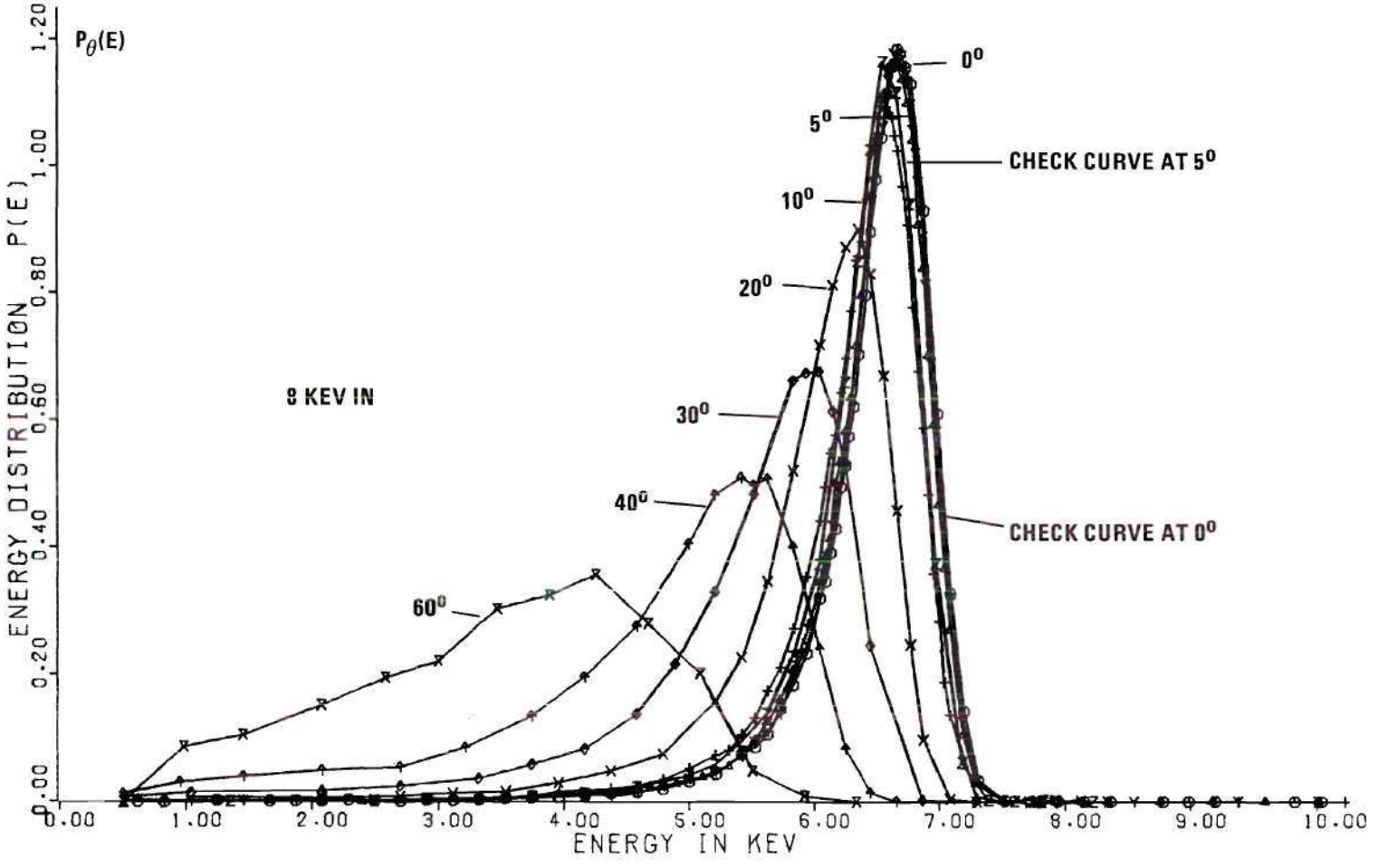

Figure 18. Total Particle Energy Distributions for 8 keV Input

the transmitted particles except for the data for four keV input energy.

Particle Fluxes

This research measured the flux of Li^+ and the flux of all lithium particles which had been transmitted through the carbon film. The Li^+ flux $C(\theta)$ is simply related to the output of the large aperture Faraday cup by

$$C(\theta) = I_L(\theta)/\Delta\,\Omega_L \tag{25}$$

where $\Delta\,\Omega_L$ is the solid angle subtended by the large aperture cup and $I_L(\theta)$ is the number of particles per second (current/e) measured in the Faraday cup.

If Equation 14 is solved for $T(\theta)$, the result is

$$T(\theta) = I_T(\theta)/\left[\Delta\,\Omega_T \int_{-\infty}^{\infty} G_T(E)p_\theta(E)dE\right] \tag{26}$$

Equation 26 is the basis of the determinations of the total flux of lithium particles as a function of the angle into which they have been scattered.

The experimental procedure for determining particle fluxes and eight keV results are given below. Complete results are given in Appendix III.

Procedure

For each input energy (4, 6, 8, or 10 keV) the particle flux data were taken using the same portion of film on which the energy distribution data were taken. After the input current was determined and the film had

been placed in the path of the beam, the source was rotated to aim to one side of the large aperture detector. The angular potentiometer signal, large aperture cup current, and the CSI detector output were monitored and recorded by the data acquisition system. The source was rotated to another angle and the readings repeated. Therefore, angular data for Li^+ and for all particles were taken at the same times; of course, the angle into each detector was different. For example, while a point for which the input beam direction was 10 degrees from the large aperture cup was being taken, the reading for which the input beam direction was 50 degrees from the CSI detector was also being taken. Data near the large aperture Faraday cup were taken first, but the angular scan was continued until data were taken with the source aimed on the other side of the CSI detector. All of the data were entered into the computer. $C(\theta)$ was determined as indicated in Equation 24. Linear interpolation was used to obtain $C(\theta)$ at 326 equally spaced points between 0 and 65 degrees. $T(\theta)$ was also desired at the same 326 points. To use Equation 25 to determine $T(\theta)$ requires that the average gain, $\langle G_T(E) \rangle_p$, be known at each angle for which $T(\theta)$ was desired. $\langle G_T(E) \rangle_p$ was calculated at the angles for which energy distributions, $p_\theta(E)$, were known. Values of $\langle G_T(E) \rangle_p$ were then determined at the 326 desired angles by linear interpolation between angles for which it was known. $I_T(\theta)$ was also determined at the 326 angles by linear interpolation between data points. $T(\theta)$ was then calculated at the 326 evenly spaced angles by using Equation 26. For many of the remaining calculations it was necessary to multiply $C(\theta)$ and $T(\theta)$ by $\sin(\theta)$. In order to get meaningful results after multiplying by $\sin(\theta)$, it was necessary to have

determined $C(\theta)$ and $T(\theta)$ at a large (326) number of points. Interpolation after multiplying by $\sin(\theta)$ would have introduced larger errors.

$C_N(\theta)$ and $T_N(\theta)$ are defined by the following equations.

$$C_N(\theta) \equiv C(\theta) / \int_0^{\pi/2} C(\theta) 2\pi \sin\theta d\theta \tag{27}$$

$$T_N(\theta) \equiv T(\theta) / \int_0^{\pi/2} T(\theta) 2\pi \sin\theta d\theta \tag{28}$$

The first integral represents the total Li^+ transmitted through the film per second, and the second integral represents the total lithium particles transmitted per second. The integrals were approximated by integrating from 0 to $\pi/2.77$ (65 degrees). The normalized fluxes, $C_N(\theta)$ and $T_N(\theta)$, were calculated from Equations 27 and 28. They were then multiplied by $2\pi\sin(\theta)$ to obtain what will be called angular distributions.

Results

The outputs of the large aperture Faraday cup and the CSI detector are shown in Figure 19. These curves are also for eight keV input energy. The x's represent data points which have been connected by straight lines. The fluxes, $C(\theta)$ and $T(\theta)$, which were calculated from this data are shown in Figure 20. Fluxes for other input energies are given in Appendix III. The entire curves are the interpolated results. The symbols are not data points, but are used only to distinguish between curves.

The possible systematic errors in $C(\theta)$ are solid angle determinations and electrometer accuracy. The combined systematic possible error is $\pm$ 7 percent. Random errors are due to input beam fluctuations and background

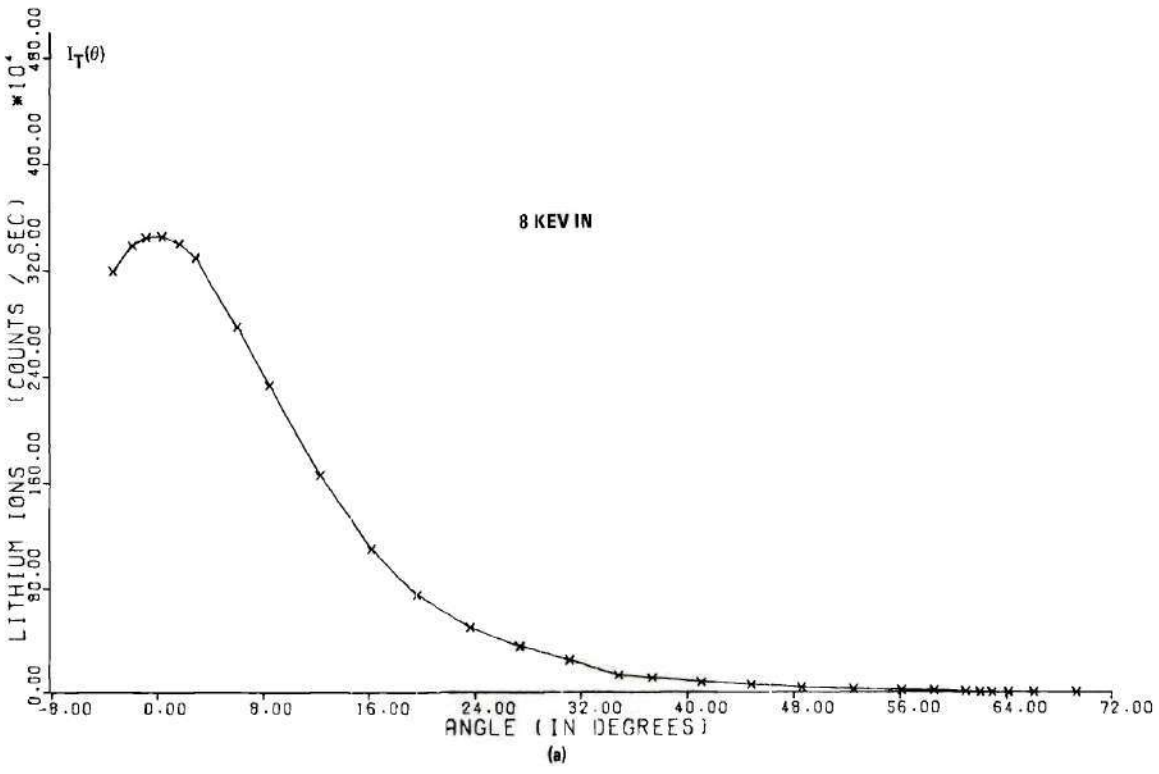

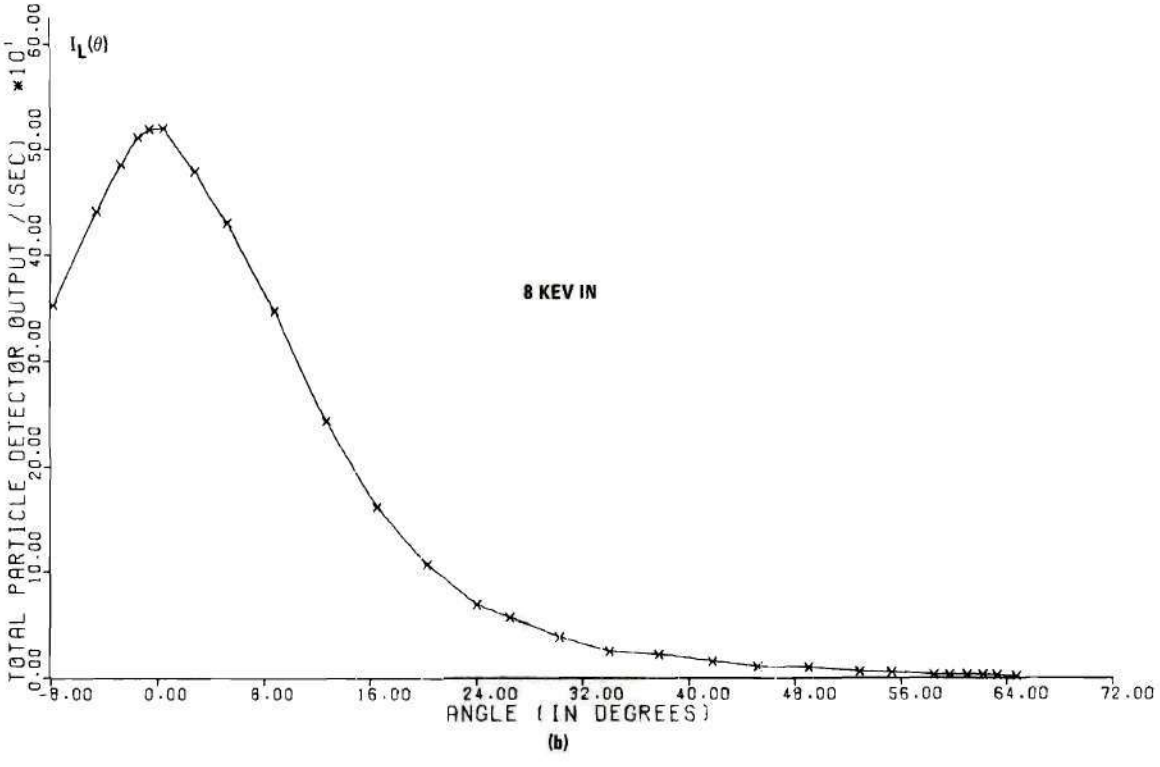

Figure 19. Angular Data for 8 keV Input
(a) Faraday Cup Output
(b) CSI Detector Output

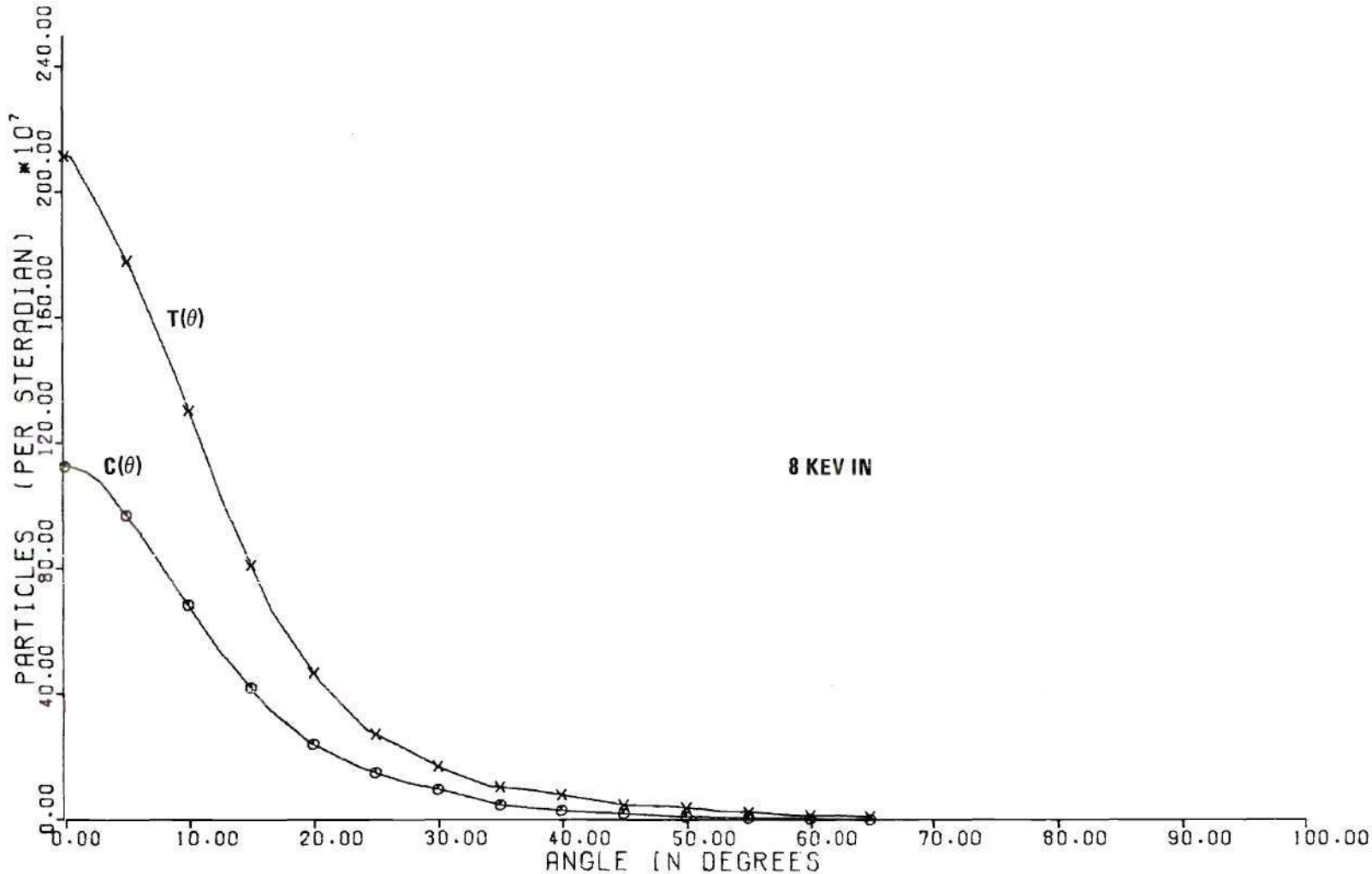

Figure 20. Fluxes of Positive and Total Particles for 8 keV Input

electron noise. The beam fluctuations are estimated to cause magnitude errors of less than ± 2 percent. However, the background noise is estimated to be about two percent of the maximum flux value. This electron noise error becomes very important at large angles where the positive current was comparable to the background noise. Therefore, the measurement of $C(\theta)$ is always too small at large angles.

The measurement of $T(\theta)$ has a possible systematic error from the $G_T(E)$ determinations of ± 9 percent and a random error of ± 7 percent. One of the solid angle inaccuracies present in $G_T(E)$ determination would cancel in the determination of $T(\theta)$. The source stability during the determination of $I_T(\theta)$ adds an additional ± 2 percent. The errors in $T(\theta)$ discussed so far amount to ± 18 percent of $T(\theta)$. There was also an additive noise for this measurement due to extraneous pulse counts of about one percent of the maximum value of $T(\theta)$. This error becomes quite significant at large angles, especially when $T(\theta)$ is multiplied by $\sin(\theta)$ and integrated. The measurement of $T(\theta)$ is always too large at large angles.

Figure 21 shows the angular distributions for particles which had eight keV input energy. Results for the other input energies are again given in Appendix III. Again the symbols are only to distinguish between curves. These curves are important since they indicate the net number of particles which have undergone a given amount of deflection. They determine the importance of the energy distributions at the various angles.

Systematic errors should be completely removed in these curves. However, new errors may be introduced due to the integrations indicated

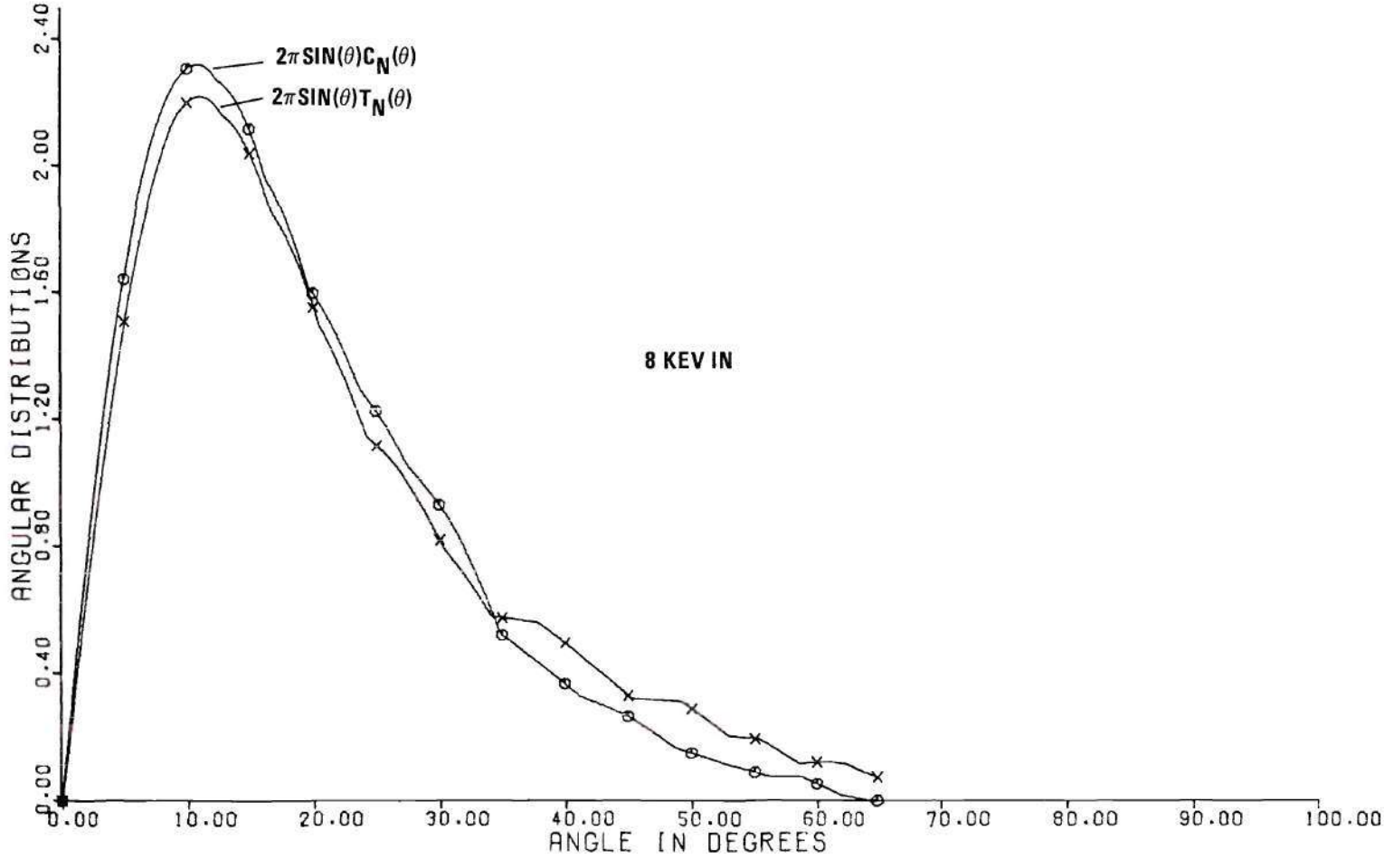

Figure 21. Angular Distributions for 8 keV Input

in Equations 27 and 28. The error due to the truncation of the curve and reduction of the upper limit of integration to $\pi/2.77$ (65 degrees) is probably insignificant except for the four keV curves where it creates an obvious error. For four keV, perhaps ten percent of the particles are scattered through angles larger than 65 degrees. Hence, the integrals in Equations 27 and 28 would be ten percent too small. Consequently $C_N(\theta)$ and $T_N(\theta)$ may be ten percent too large.

For large angles ($\geqq$ 30 degrees) the angular distribution of total particles is too large due to the added noise which is always positive. The distribution of Li^+ is too small at large angles due to the electron noise. The amount of error is hard to evaluate, but the true curves probably lie between the two plotted curves.

There is a random error of $\pm$ 7 percent of the value present in the determinations of $C(\theta)$ and $T(\theta)$. These errors are also present in the angular distributions.

Film Thickness

The film thickness was measured by the multiple beam interferometry method of Scott, McLauchlan, and Sennett.[31] The film used in this research was determined to be 184 Å $\pm$ 30 Å. The measurement was made on a small piece of film which had been left on the glass slide. On similar slides the variation of thickness with position on the slide was measured. No variation was detectable outside of the measurement accuracy of approximately $\pm$ 15 percent.

In order to compare the results of this research with theory, it would have been desirable to determine the thickness in terms of a mass

per unit area. Such a determination was not possible for these films that had been deposited on glass slides. If these films were close to the manufacturers stated mass per unit area of 2 $\mu g/cm^2$ and if the density were that of bulk carbon, the thickness should have been approximately 100 Å. The density of these films may be only 5/9 of the bulk density. As mentioned previously, the data reported in this research was taken so that the thickness in mass per unit area enters as a single unknown parameter.

Energy Losses

This research measured several types of energy losses as a function of input energy and the angle of emergence from the film. These losses were determined from the Li^+ energy distributions, $f_\theta(E)$, the energy distributions of all lithium particles, $p_\theta(E)$, and the angular distributions of all particles. The definition and procedure for determining these losses are given below. Typical results will also be discussed in this section.

Definitions

At each angle θ for which an energy distribution was determined, average and most probable transmitted energies were determined. One average energy and one most probable energy were determined using each type of energy distribution. These transmitted energies are defined by the following equations and inequalities.

$$\langle E \rangle_p \equiv \int_{-\infty}^{\infty} E p_\theta(E)\, dE \tag{29}$$

$$\langle E \rangle_f \equiv \int_{-\infty}^{\infty} E f_\theta(E)\, dE \tag{30}$$

$$p_\theta(E_{mp}) \geq p_\theta(E) \quad \text{for all } E \tag{31}$$

$$f_\theta(E^+_{mp}) \geq f_\theta(E) \quad \text{for all } E \tag{32}$$

The corresponding energy losses at each angle θ are defined by

$$\Delta E \equiv E_{in} - \langle E \rangle_p \tag{33}$$

$$\Delta E^+ \equiv E_{in} - \langle E \rangle_f \tag{34}$$

$$\Delta E_{mp} \equiv E_{in} - E_{mp} \tag{35}$$

$$\Delta E^+_{mp} \equiv E_{in} - E^+_{mp} \tag{36}$$

For a given input energy the average energy of all transmitted particles is defined by

$$E_{av} \equiv \int_o^{\pi/2} \langle E \rangle_p T_N(\theta) 2\pi \sin\theta d\theta \tag{37}$$

The corresponding average energy loss of all particles which has input energy E_{in} is defined by

$$\Delta E_{av} \equiv E_{in} - E_{av} \tag{38}$$

Procedure

All of the transmitted energies and energy losses defined above were calculated on the computer. The appropriate distributions were searched for the maximum to determine E_{mp} and E^+_{mp}. The average energies

were determined by numerical integration using the trapezoidal rule. To obtain E_{av}, the values of $\langle E \rangle_p$ at several angles was needed. These values were obtained by linear interpolation and extrapolation.

Results

Most of the data presented in this section is again for eight keV input energy. Comparable data for the other three input energies will be found in Appendix III.

Figure 22 shows the transmitted energies as a function of the emergence angle. The symbols are again the data points which have been connected by straight lines. The spacing between data points in the energy distribution determinations is the principal source of error. Points were rarely taken at closer intervals than the resolution of the energy analyzer. The most probable values could be slightly shifted by random error in adjacent data points. The random error was considered to be reduced by the integrations in the determinations of average values. Each energy distribution curve was examined to estimate the possible error introduced in the transmitted energies due to random errors in adjacent data points. This analysis led to the following estimated uncertainties. For E_{mp} the combined uncertainty is $\pm$ 3 percent for $\theta \leqq 10$ degrees and $\pm$ 12 percent for $\theta \geqq 20$ degrees. For E^{+}_{mp} the estimated uncertainty is $\pm$ 3 percent for $\theta \leqq 10$ degrees and $\pm$ 10 percent for $\theta \geqq 20$ degrees. For $\langle E \rangle_p$ the estimated uncertainty is $\pm$ 2.5 percent for $\theta \leqq 10$ degrees and $\pm$ 10 percent for $\theta \geqq 20$ degrees. For $\langle E \rangle_f$ the estimated uncertainty is $\pm$ 2 percent for $\theta \leqq 10$ degrees and $\pm$ 8 percent for $\theta \geqq 20$ degrees.

Figure 23 gives the results for the energy losses as a function of the emergence angle. These data are also presented in Table 1. Table 1

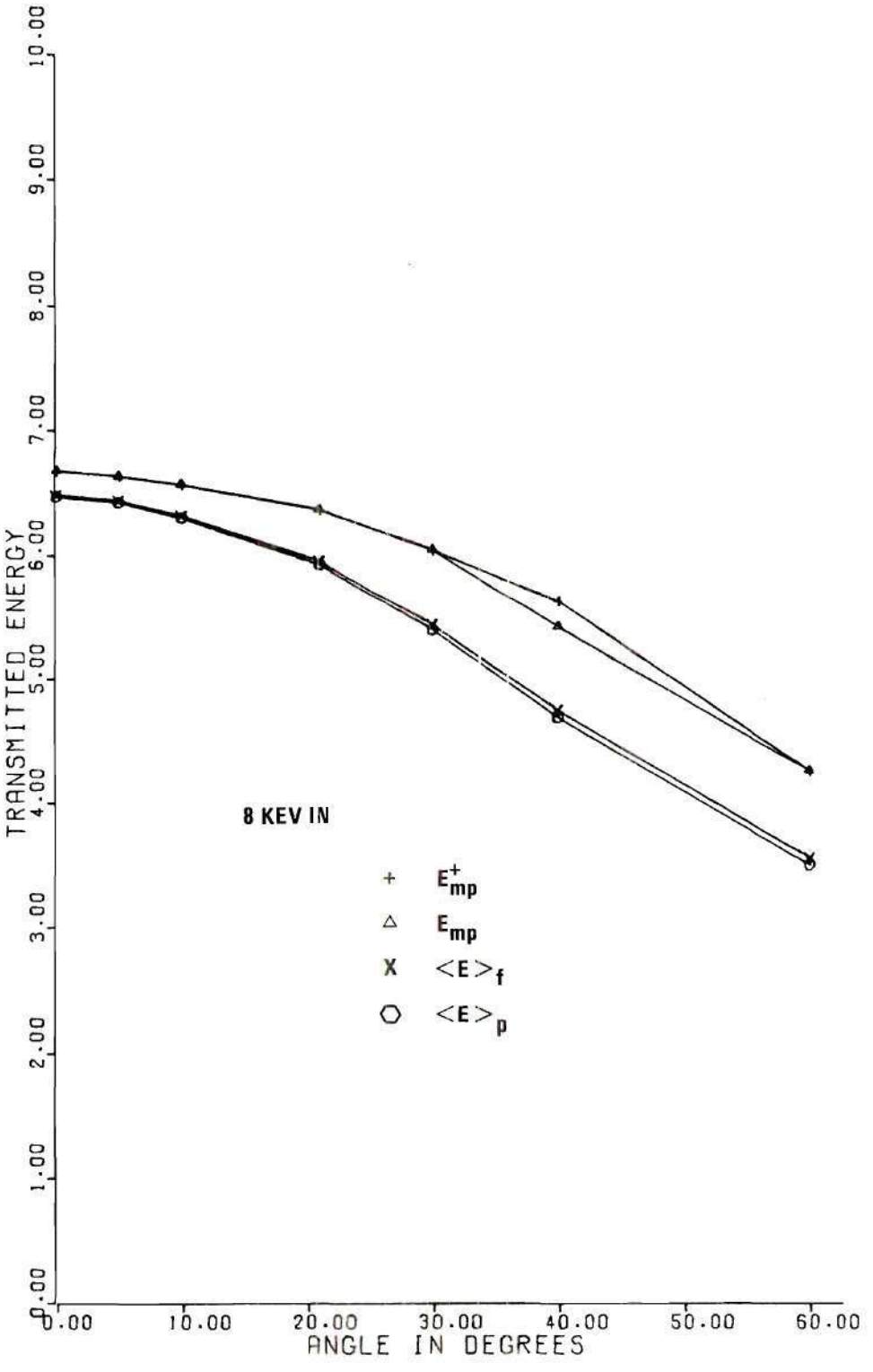

Figure 22. Transmitted Energies for 8 keV Input (Energy in keV)

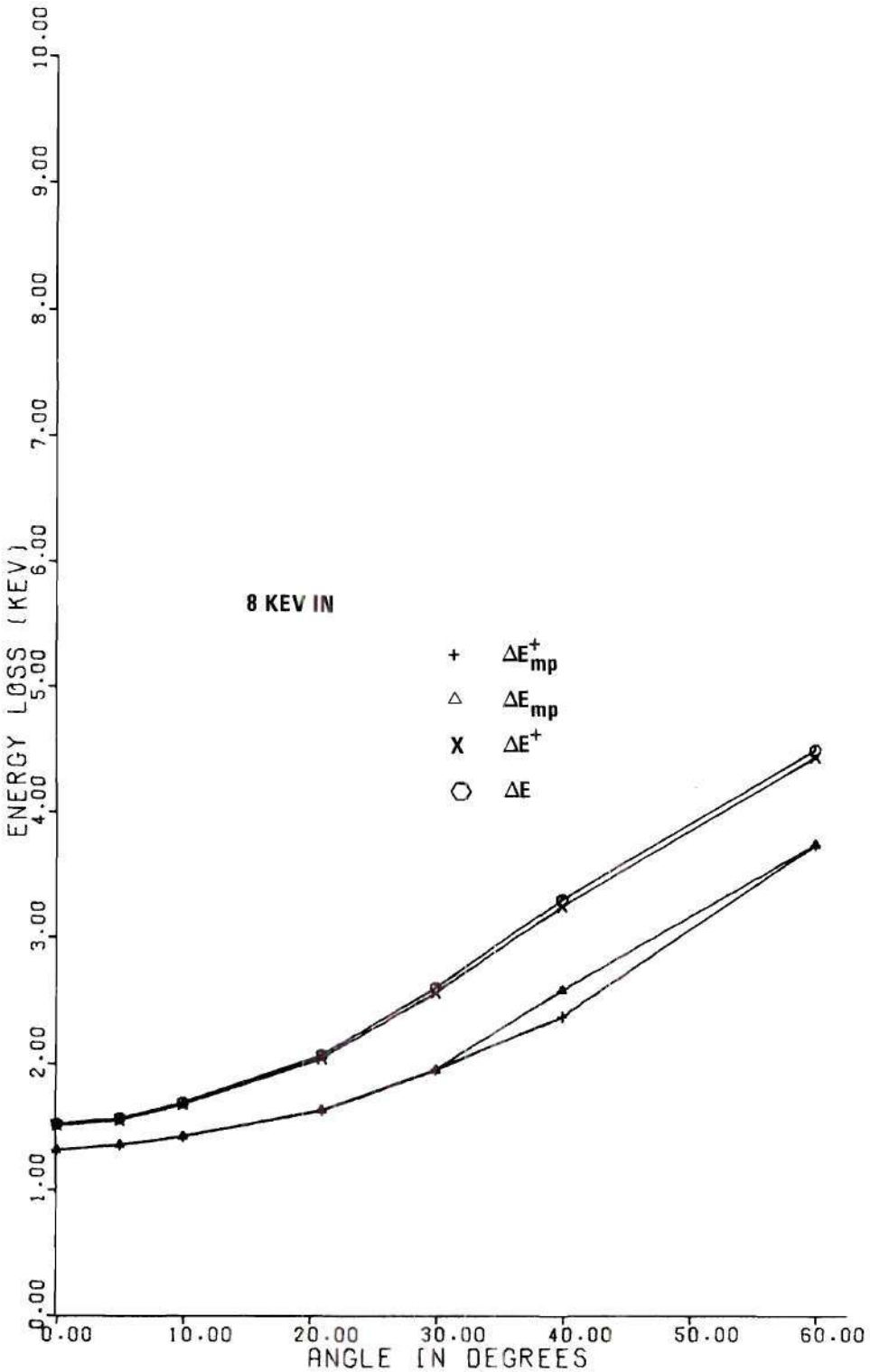

Figure 23. Energy Losses for 8 keV Input

TABLE 1. ENERGY LOSS OF 8 KEV PARTICLES

θ	ΔE	ΔE_{mp}	ΔE^{+}	ΔE^{+}_{mp}
.0	1.526	1.318	1.514	1.318
5.0	1.572	1.363	1.559	1.363
10.0	1.696	1.427	1.680	1.427
21.0	2.067	1.635	2.044	1.635
30.0	2.601	1.952	2.560	1.952
40.0	3.304	2.578	3.246	2.369
60.0	4.496	3.737	4.440	3.737
5.0	1.641	1.433	1.628	1.433
.0	1.541	1.344	1.529	1.344

also includes the check curve energy losses at the bottom of the table. The average energy losses are about 15 percent greater than the most probable values.

The uncertainties in transmitted energies are larger at the larger angles. However, the energy losses are also larger at the larger angles. Consequently, the uncertainty for each type of energy loss can be estimated for all angles as a fixed percentage. The estimated uncertainties in ΔE^{+}, ΔE, ΔE^{+}_{mp}, and ΔE_{mp} are ± 10, ± 15, ± 15, and ± 20 percent respectively.

For easy comparison, ΔE, the average energy loss of all particles is plotted versus emergence angle in Figure 24 for all four input energies. Figure 25a shows the energy loss when averaged over all angles. It is plotted as a function of the algebraic average of the input energy and the average transmitted energy. The algebraic average will be called the average energy in the film. The energy loss, ΔE_{av}, is also plotted in Figure 25b. This time it is plotted as a function of the average velocity in the film. Tabular data are given in Table 2. The estimated uncertainty in ΔE_{av} is ± 20 percent.

The most probable energy loss, ΔE_{mp}, at zero degrees is also plotted in Figure 25b. It is plotted as a function of the velocity corresponding to the energy midway between E_{in} and E_{mp}. This is the energy loss usually measured to determine the electronic stopping power. It is clear that the result is a first order polynomial in velocity, however, the line when extrapolated does not pass through the origin as would be expected from the Lindhard et al.[2] theory if only electronic stopping were present.

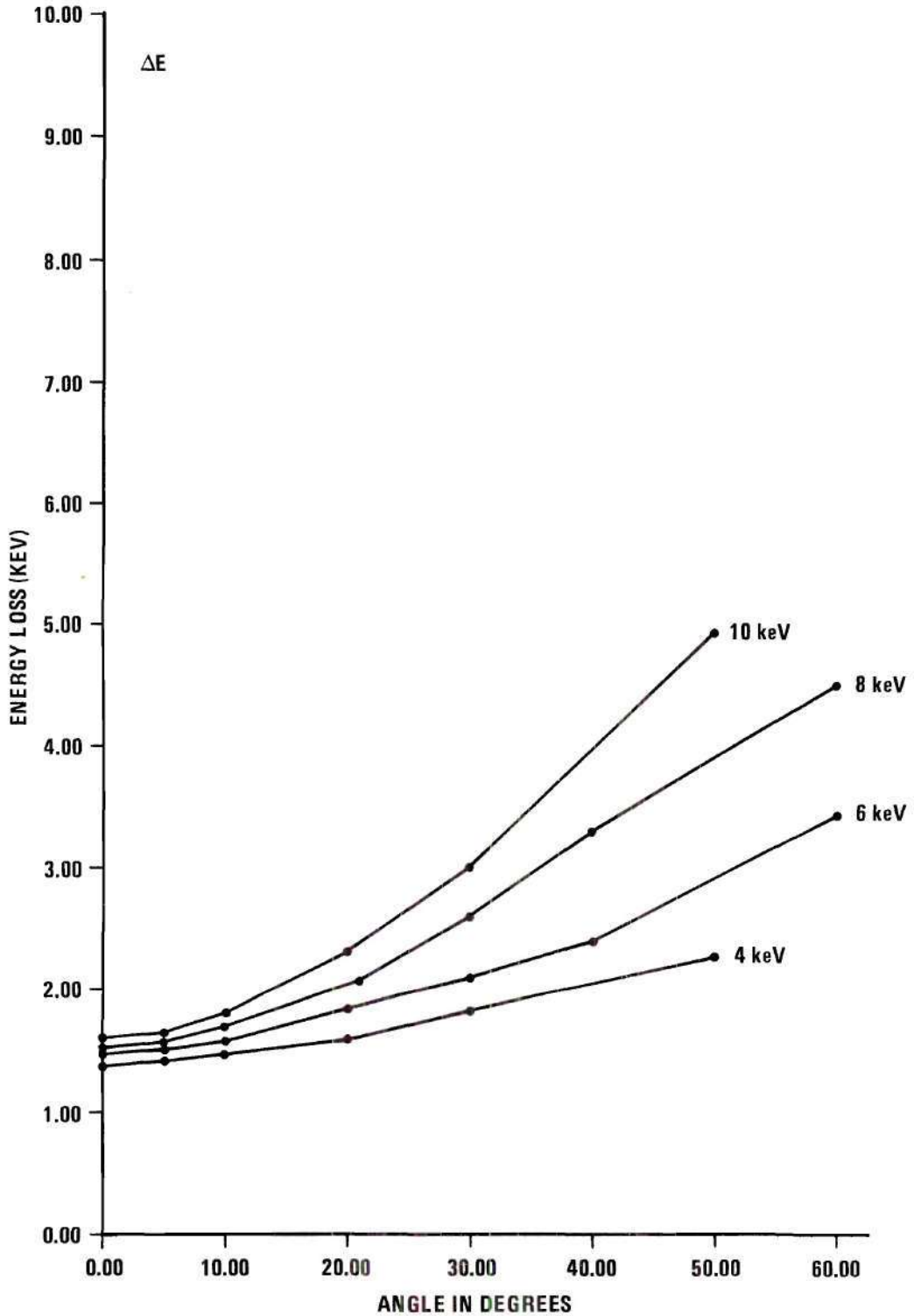

Figure 24. Average Energy Losses for Each Input Energy

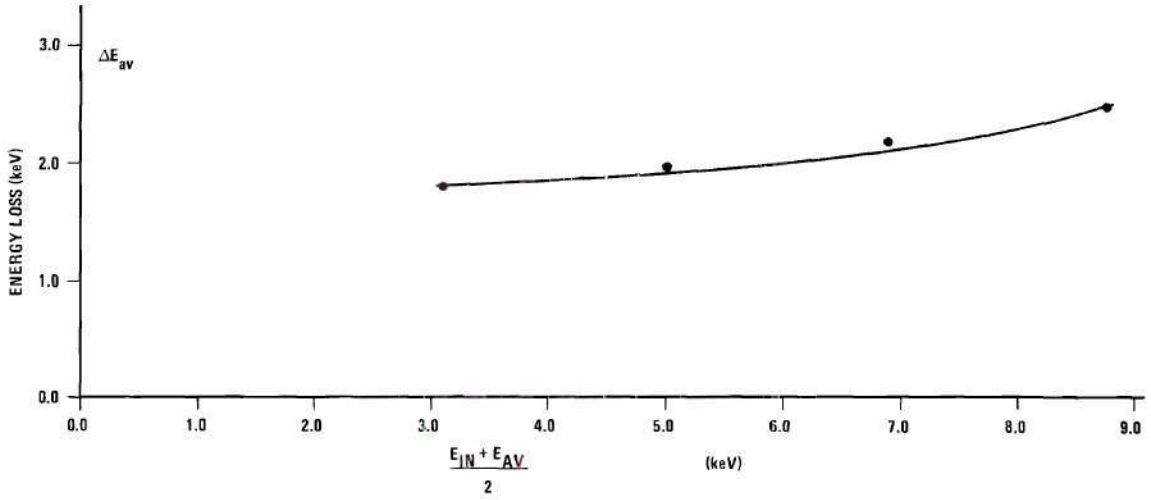

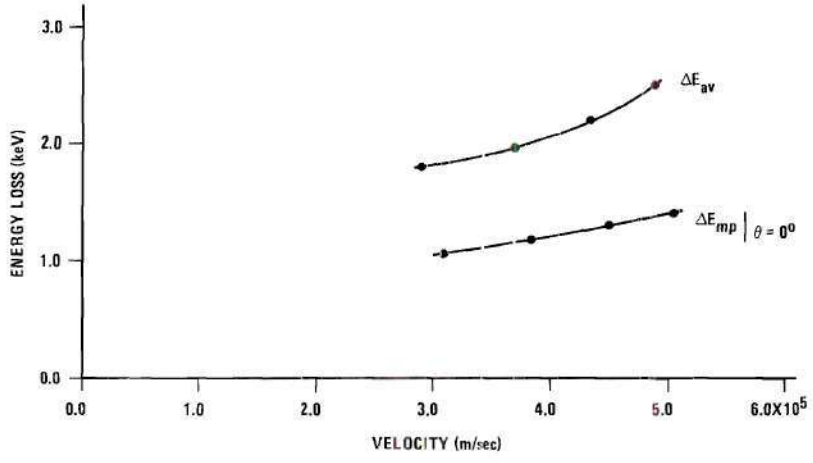

Figure 25. Energy Loss Averaged Over All Angles

Table 2. Average Energy Loss for Different Input Energies*

E_{in}	Average Energy in Film	Average Velocity in Film (10^7 cm/sec)	ΔE_{av}	$\frac{E_{mp} + E_{in}}{2}$	v_o^{**} (10^7 cm/sec)	$\Delta E_{mp}\Big\vert_{\theta = 0}$
10	8.75	4.90	2.51	9.29	5.05	1.41
8	6.90	4.35	2.21	7.34	4.49	1.32
6	5.02	3.71	1.97	5.41	3.85	1.19
4	3.10	2.91	1.81	3.46	3.09	1.09

*All energies are in keV.

**v_o is the velocity that corresponds to the algebraic average of E_{in} and most probable energy at zero degrees.

Experiment Evaluation Checks

Some initial experiment checks have already been discussed. The main purpose of those checks were to determine if the source and detectors were functioning properly so that experimentation could begin. There also exist several methods whereby the results of the experiment can be evaluated. These will be discussed in this section.

Consistency check tables are presented to facilitate this discussion. Table 3 pertains to the eight keV checks. Tables for other input energies are given in Appendix III. The columned data are the ratios of experimental values determined in two different ways. These ratios will be discussed in more detail in the following paragraphs. Several other experimentally determined quantities are presented for comparison in this table. The number of charged particles and total particles as determined from the integrals in Equations 27 and 28 have been divided by the input current. The transmitted energies, $\langle E \rangle_f$ and $\langle E \rangle_p$, have been multiplied by the appropriate angular distributions and integrated to obtain the average transmitted energy in keV of Li^+ and of all particles. The angle θ has been multiplied respectively by the angular distribution of Li^+ and the angular distribution of all particles and then integrated to obtain the average angles of emerging Li^+ and all particles. The average energy loss of all emerging particles, ΔE_{av}, is also given. The small angles near the bottom of the table identify the data from the energy distribution check curves.

Energy Analyzer Operation

It is possible to determine the flux of charged particles by integrating the energy analyzer output. Equation 12 gives

TABLE 3. CONSISTENCY CHECKS FOR INPUT ENERGY OF 8 KEV
TOTAL LI+ DETECTED/INPUT LI WAS .553
TOTAL PARTICLES DETECTED/INPUT LI WAS 1.106

θ	$\frac{C_E(\theta)}{C(\theta)}$	$\left\langle \frac{1}{R} \right\rangle_f \frac{C}{T}$	$\frac{\langle G_T(E) \rangle_p}{G_T(\langle E \rangle_p)}$	$\frac{\langle E \rangle_f}{\langle E \rangle_p}$	$\frac{E^+_{mp}}{E_{mp}}$	$\frac{\Delta E^+}{\Delta E}$	$\frac{\Delta E^+_{mp}}{\Delta E_{mp}}$
.0	.91	.98	1.00	1.00	1.00	.99	1.00
5.0	1.01	1.01	1.00	1.00	1.00	.99	1.00
10.0	1.04	.97	1.01	1.00	1.00	.99	1.00
21.0	1.31	.99	1.01	1.00	1.00	.99	1.00
30.0	1.43	1.10	1.00	1.01	1.00	.98	1.00
40.0	2.13	.73	.98	1.01	1.04	.98	.92
60.0	5.53	.42	.94	1.02	1.00	.99	1.00
5.0	.89	1.01	1.01	1.00	1.00	.99	1.00
.0	.93	.98	1.00	1.00	1.00	.99	1.00

AVERAGE ENERGY OF LI+ PARTICLES = 5.92
AVERAGE ENERGY OF ALL PARTICLES = 5.79
AVERAGE DEFLECTION ANGLE OF LI+ = 18.74 DEGREES
AVERAGE DEFLECTION ANGLE OF ALL = 20.45 DEGREES
AVERAGE ENERGY LOSS OF ALL PARTICLES = 2.21 KEV

$$C_E(\theta) = \frac{1}{\Delta \Omega_E} \int_{-\infty}^{\infty} \frac{I_E(E_o,\theta)}{G_E(E_o)} \, dE_o \tag{39}$$

The subscript E is used on $C_E(\theta)$ to indicate this flux is determined from the energy analyzer integration and not directly from a Faraday cup. This determination depends on the function $G_E(E_o)$. Therefore, it serves to check this calibration function since the value at each different angle was obtained by integrating over a different energy region. The second column of the consistency check table compares $C_E(\theta)$ to $C(\theta)$ which was determined by Faraday cup measurements. The input current was not the same for each energy analyzer scan as it was for the angular scan with the Faraday cup. Hence the comparison is not as accurate as might be desired, but, it is well within the combined accuracies of the two measurements. At large angles the ratio becomes large. This is due to electron noise that is present in the Faraday cup measurements, but not in the energy analyzer measurements.

Determination of R(E)

In order to determine $C_N(\theta)$ it was necessary to integrate $C(\theta)$ over all solid angles (see Equation 26). This integration should give the total number of Li^+ particles per second that emerge from the back side of the film. If all lithium entering the film is transmitted, then the above integral divided by the input (and output) particles per second would be the average value of R(E), averaged over all energy and all angles. For 10, 8, 6, and 4 keV input energies the above results were 0.54, 0.55, 0.50, and 0.40 respectively. These results plotted versus their respective transmitted energies are 4 percent under, 4.5 percent over, 1.5

percent over and 11 percent under the previously determined R(E) curve. The four keV value is low. From inspection of the angular distribution curve at four keV it is obvious that the integral of $C(\theta)$ is too small due to truncation error. If instead the integral of $C(\theta)$ is divided by the total particles detected, integral of $T(\theta)$, this value is less than one percent over R(E). All of these determinations were made on a different portion of film but have shown very good quantitative agreement with R(E). This seems to refute the hypothesis that R(E) depends very sensitively on the particular area of the film used.

The purpose of the third column of the consistency check tables (labeled $\left\langle \frac{1}{R} \right\rangle_f \frac{C}{T}$) was to determine if there was an angular dependence of R(E). In order to see the angular dependence more clearly, $G_T(E)$ was adjusted by a different constant (changed by less than 30 percent) for each input energy to give numbers close to one. Therefore, the percent variation with angle could be easily seen. No variation with angle greater than ten percent was observed except at the large angles for which the measured $C(\theta)$ was too small due to the electron noise.

This adjustment of $G_T(E)$ led to believable results for the total number of particles detected. The angular distribution, $2\pi\sin(\theta)T_N(\theta)$, does not depend on the constant which adjusts the magnitude of $G_T(E)$. Examination of this angular distribution and the knowledge that $T(\theta)$ is too large at large angles make it obvious that the integral of $T(\theta)$ over all angles would be too large for the ten and eight keV input energies and too small (due to truncation at 65 degrees) for the four keV input energy. These conclusions are compatible with the values found in the consistency check tables.

Average Values of Functions

The fourth column of the consistency check tables compares the average of a function of energy with the value of the function evaluated at the average energy. In particular it compares $\langle G_T(E) \rangle_p$ to $G_T(\langle E \rangle_p)$. The comparison is favorable, but was to be expected due to the relatively small variations in $G_T(E)$. It is of more value for energies $E \leq 2.5$ keV where $G_T(E)$ varies more. Its most important application was to check the operation of the computer program's determination of expected values.

Comparisons of Energy Losses

All other columns of the table compare the average energies, most probable energies, average losses, and most probable losses as determined from the $f_\theta(E)$ and $p_\theta(E)$ distributions. The agreement is excellent. This implies that the energies measured are not affected by R(E) very much. Therefore, the uncertainty in R(E) does not strongly affect the uncertainties in energies determined from $p_\theta(E)$.

Pin Holes

Pin holes in the target films could be most easily detected by looking at the output of the Faraday cups when the source was scanned across them. Since the Faraday cup usually measured a current three orders of magnitude smaller than the input current, a pin hole that allowed only one thousandth of the input current to pass through would result in a step function in the scan which would be quite noticeable. Pin holes also would show up in the zero angle energy analysis as a spike at the input energy.

Time Dependence of Film Characteristics

After all energy analysis was completed for a given input energy,

at least one check energy scan was taken to determine if the film had changed its characteristics appreciably. These results are presented at the bottom of almost all data tables. The repeatability was within the claimed accuracy of the measurement for all measurements reported in this research. However, for input currents greater than 10^{-10} amps this was definitely not the case.

Thickness Variations of the Film

As mentioned previously, similar films to those used were studied interferometrically for variations in thickness. Variations greater than the uncertainty (15 percent) of the measurement were not found. A more sensitive test is thought to be the comparison of the zero angle energy distributions. Distributions at zero angle for 10, 8, 6, and 4 keV input energies were compared with the same distributions used to determine R(E). The R(E) determination had been made on a different portion of the film than that used for any of the other measurements. Overlays of the two curves indicated that their difference in energy losses would be less than four percent for all four input energies.

Angular Symmetry

The scattering and energy loss were measured only in a plane. It was assumed that all distributions depend only on θ. Angular scans were usually made about ten degrees past the CSI detector and large aperture Faraday cup. There was good agreement between results on either side of the detectors. All of the six keV distributions were made on the opposite side of the analyzer from the 10, 8, and 4 keV data runs. No obvious error is present. Some of the energy check scans were also made on the

opposite side of the detector from the first energy scan at that angle. The energy losses, ΔE, ΔE_{mp}, ΔE^{+}, and ΔE^{+}_{mp}, determined from these check scans differed from the losses determined by the original scan by less than four percent.

CHAPTER IV

COMPARISONS WITH OTHER RESULTS

Comparisons with selected previous experimental results and theory are presented in this chapter. A comparison with the higher energy results of Ormrod and Duckworth[3] is given first. Some of the energy losses are converted to stopping cross sections to compare with the theory of Lindhard et al.[2] Finally, the total flux per steradian is compared to the theory of Meyer.[9]

Figure 26 shows the results of Ormrod and Duckworth for electronic stopping of lithium in carbon. Nuclear stopping causes angular deflection of the transmitted particles. Therefore, by looking only at the particles transmitted at zero degrees, most of the particles which have undergone nuclear stopping will have been eliminated. Those which have undergone large scattering angles and then been rescattered back into the incident (zero degree) direction are expected to contribute to the tail of the distributions but not to the peak. Therefore, to compare to the electronic stopping measured by Ormrod and Duckworth, $\Delta E_{mp}/N\Delta R_p$ was calculated and is shown in Figure 26. The most probable energy loss, ΔE_{mp}, for zero degrees was used. The atom density, N, for very thin films of carbon is not well known. A value of N that corresponds to the bulk solid specific gravity of 2.0 was used for this comparison. The thickness of the film, ΔR_p, is an increment of the projected range R_p. Theoretical stopping powers are cal-

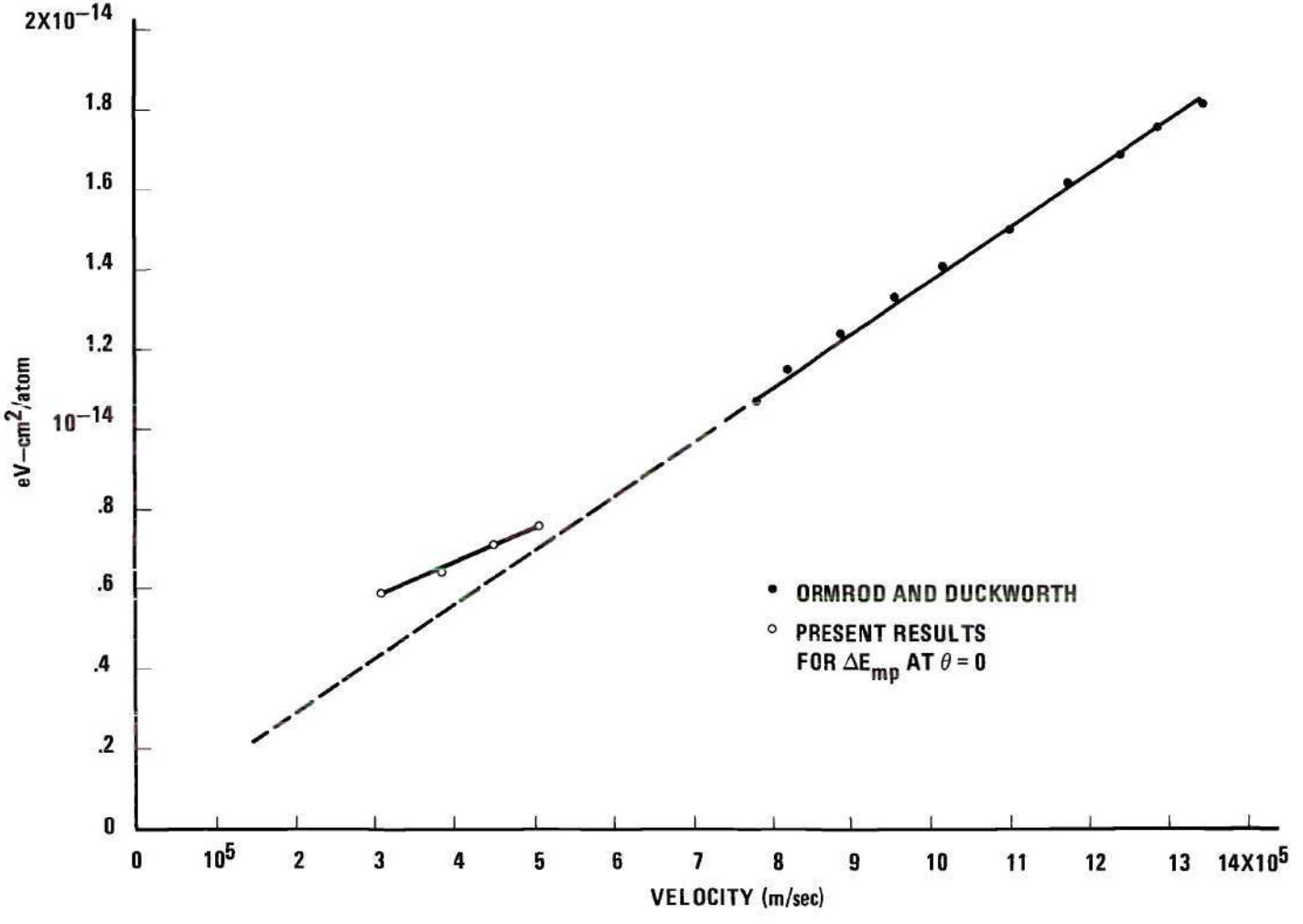

Figure 26. Comparison with Ormrod and Duckworth's Electronic Stopping Cross Sections for Lithium on Carbon (Specific gravity of 2.0 used in comparison.)

culated for differentials in total path length, dR_t. For particles that emerge at zero degrees ΔR_p is expected to be a very close approximation to ΔR_t. Ormrod and Duckworth's results are clearly proportional to velocity as theory predicts. The present results are a linear function of velocity but do not extrapolate to the origin. This indicates that, for energies below 10 keV, the nuclear stopping affects the energy distributions of emerging particles even at the peak of the curve.

Two experimental stopping cross sections are compared to the theory of Lindhard et al.[2] in Figure 27. The experimental stopping cross sections are determined from the energy loss averaged over all angles, ΔE_{av}, and again from ΔE_{mp} at zero degrees. For both experimental stopping cross sections the value of N and ΔR_p used the same values used for the previous comparison to Ormrod and Duckworth's experimental results. The experimental stopping cross section determined by using ΔE_{av} corresponds to the average energy lost in the film and should be compared with the total (electronic + nuclear) stopping cross section. The experimental stopping cross section determined from the most probable energy loss at zero degrees should be dominated by electronic stopping and has often been interpreted as the electronic stopping cross section for energies greater than 20 keV. It should be noted that use of a smaller density would raise the experimental points in Figure 27. The solid lines are the theoretical stopping cross sections. S_e was determined from Equation 1 (see Chapter I). The value of ξ_e used was $Z_1^{1/6}$. S_n was determined from the universal curve for nuclear stopping of Lindhard et al. The dashed line is the total stopping cross section obtained by adding Equations 1 and 2. That is, the result of adding S_e and the nuclear stopping cross section determined

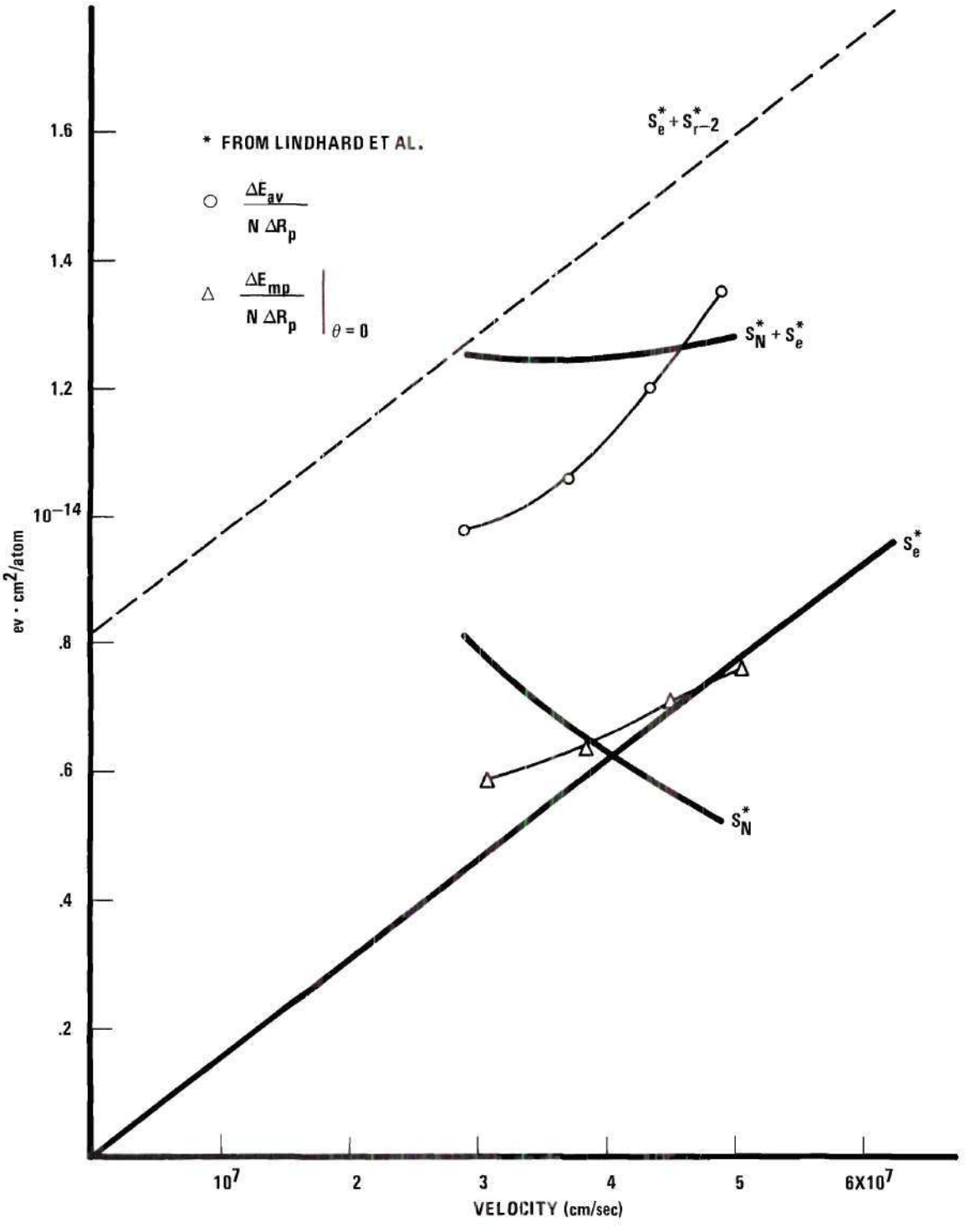

Figure 27. Comparison with Lindhard et al.
(Specific gravity of 2.0 used for comparison.)

from the inverse squared potential approximation to the "more accurate" Thomas-Fermi potential.

As previously mentioned in Chapter II in the discussion of film thickness, the bulk density of carbon may be too large for the thin carbon film. In the comparison to Meyer's theory that will be discussed in the next paragraph, a specific gravity of 1.54 was found to give a "good fit." If the specific gravity of the thin film were 1.54 instead of the 2.0 value used in this comparison to Lindhard et al., each data point would be raised by 30 percent. The total stopping would then agree quite well with the dashed curve. Also, for the 8 and 10 keV input energies, the angular distributions are known to be too large at large angles (see Chapter III and Appendix III). This tends to favor the large energy losses at those angles when ΔE_{av} is calculated. Therefore, the experimental stopping cross sections are probably somewhat (less than 10 percent) too high for the 8 and 10 keV input energies.

In Figure 28 the total particle flux, $T(\theta)$, is compared to the theory of Meyer.[9] Meyer's results give the flux per steradian normalized by dividing by the input particles per second. His theoretical flux at zero degrees was 25 to 30 percent below the present experimental results when a specific gravity for the carbon film of 2.0 was used. When a specific gravity of 1.54 was used, the agreement at zero degrees was within one percent. His entire curve was then plotted using the 1.54 value. The experimental and theoretical curves agree everywhere within the experimental uncertainty.

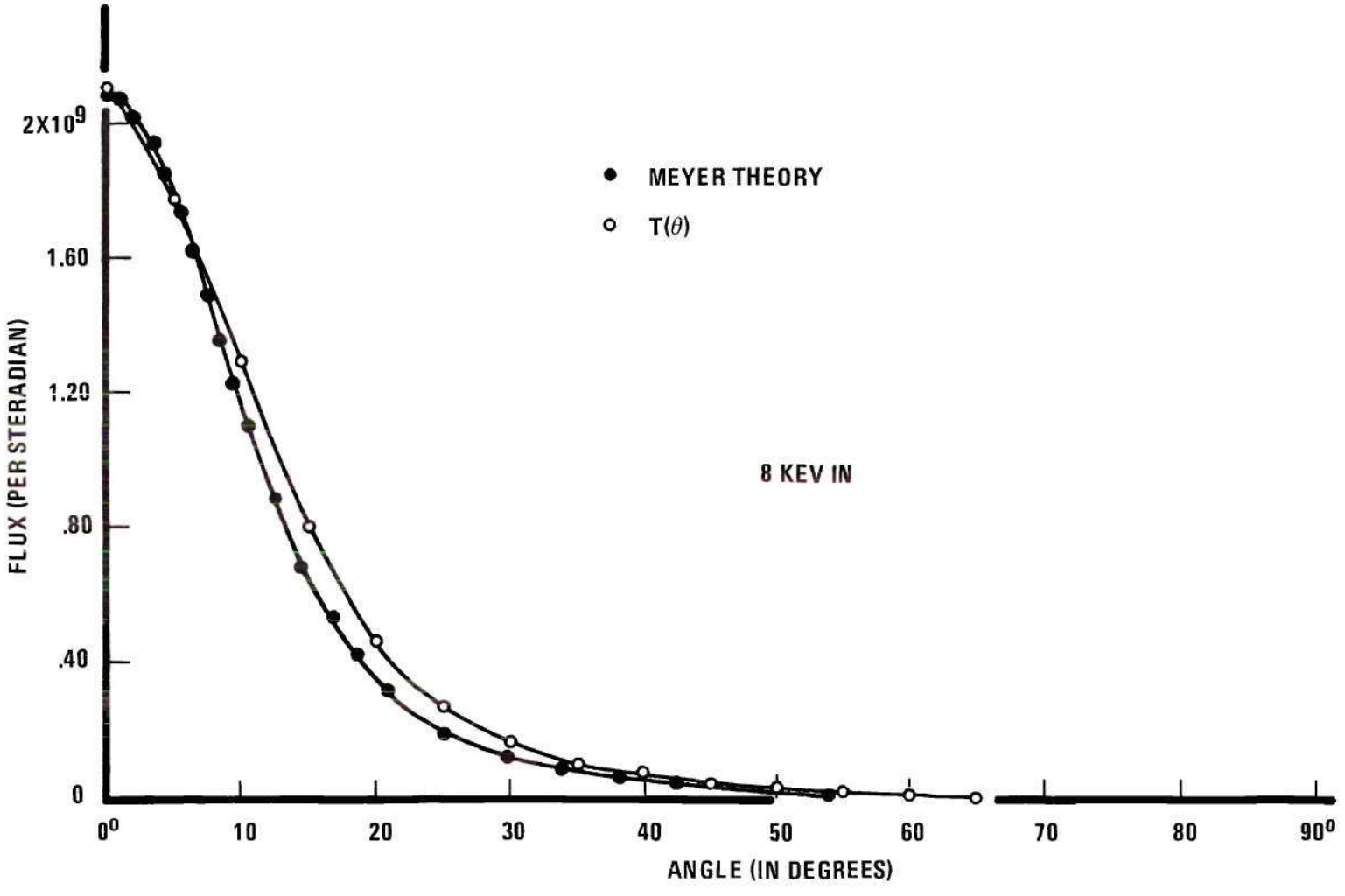

Figure 28. Comparison with the Theory of Meyer
(Specific gravity of 1.54 used for comparison.)

CHAPTER V

CONCLUSIONS AND RECOMMENDATIONS

Several conclusions will be presented in this chapter. One of the conclusions is that more research is desirable in this area. It is expected that this research will be continued and extended in this laboratory. To facilitate that research and any other research in this area several recommendations will also be made.

Conclusions

An experimental facility and associated techniques have been developed for the study of the characteristic energy losses experienced by heavy particles upon passage through thin solid films. The facility and techniques allow the energy losses and particle fluxes to be determined as a function of emergence angle and incident energy. The developed techniques have been applied to an investigation of lithium particles of 3-10 keV passing through thin carbon films. Some results have been compared to existing theories.

More specifically, this research has determined the energy distributions of all transmitted lithium particles for angles between 0 and 60 degrees for input energies of 10, 8, 6, and 4 keV. The angular dependence of the flux of all transmitted lithium particles was also determined for 10, 8, 6, and 4 keV incident energies. From the energy distributions, the most probable and average energy losses were determined as a function

of angle and input energy. The average energy loss of all emerging particles was then determined for each input energy. The increment of projected range (film thickness) through which the particles had passed was determined interferometrically. The density of atoms in a thin film was not measured. By using the bulk density of carbon and another "fitted" density, experimental stopping cross sections and particle flux were compared to existing theories.

The developed technique also allows the measurement of charged particle energy distributions, the flux of charged particles, and charge states. These were measured in this experiment for lithium. However, they cannot be reported as generally valid since they may depend on the surface condition of the film.

The experimental stopping cross section indicates that Lindhard's nuclear stopping cross section based on a fit of an r^{-2} potential to the Thomas-Fermi potential is more accurate in the 3 to 10 keV range than the cross section determined from the Thomas-Fermi potential directly. The multiple scattering theory of Meyer[9] was found to agree with the experimental angular flux determinations for eight keV input energy. The agreement was within the $\pm$ 18 percent uncertainty of the measurement when a specific gravity of 1.54 was used for the carbon film. For a more accurate comparison with theories, the density of carbon in very thin films must be better evaluated. For the energy region investigated in this research, it is clear that the most probable energy loss at zero degrees is caused not only by the more dominant electronic stopping, but also by nuclear stopping as well.

Recommendations

The apparatus and techniques presented are considered adequate for the study of energy loss of low energy particles. However, some changes in apparatus and technique should lead to improved accuracy. If an electron repeller electrode were placed between the entrance aperture of the large aperture Faraday cup and the cup itself, the electron noise that leads to significant error at large angles should be reduced. Such an electrode has been used in the small aperture detector with good results. If this does not remove the electron noise significantly, then a better method of determining $C(\theta)$ at large angles may be to use the energy analyzer integration procedure (Equation 39). Another change in the apparatus which should improve accuracy would be to monitor the input current during experiments and feed the signal back to control the source stability. Of course this current cannot be measured directly with the film in the beam path. But a signal, that is perhaps larger than the current itself, that should be directly proportional to the input current could be measured. If the target plate were not grounded but connected to an electrometer, the positive charge of the input ions that emerge as neutrals plus the positive current due to secondary electrons leaving the film could be monitored. If it proves infeasible to float the target plate, a small electrode placed before the film to measure secondary electrons might achieve the same purpose. If a more accurate experimental verification of the linearity of $G_E(E_o)$ were desired, an additional change to the apparatus could be made. The energy analyzer could be redesigned so that it could also be used as a Faraday cup. One modification in experimental technique

should obviously be made. The CSI detector should be calibrated directly by using the small aperture Faraday cup. This would significantly reduce the errors in determination of $G_T(E)$ and of those measurements which depend upon it.

There are several areas where additional research would be desirable. These suggested areas are presented in the remainder of this chapter.

The mechanism of the CSI detector is not completely understood. A careful analysis of the energy and angular distributions of this experiment would help estimate the detector output for a given angle and distance of the Channeltron from the film. It would also be desirable to study the photons produced by energetic particles passing through a film since this may be a significant contribution to output counts. If the photon production can be shown to be small enough, then perhaps the Channeltron can be used directly as a CSI detector without the film. It would of course be necessary to ground the input so that neutrals and ions would have the same energy upon striking the Channeltron walls. Also, to eliminate the detector film, it should be definitely determined that the Channeltron counting efficiency is the same for ions and neutrals. If the Channeltron can be used without the film, the CSI detector efficiency would be increased by at least two orders of magnitude.

The present apparatus could be used to study the properties of the charge states of particles emerging from films. If all areas of a film on a target plate were each investigated to determine R(E), the dependence on surface condition for different areas of the same film could be evaluated. With the same experimental arrangement, the dependence of R(E) on

bombardment time could also be evaluated. Small angles of three to five degrees (necessary to obtain strong signals) could be used for the R(E) determinations even if the films had pin holes, since normalization to input current is not necessary. Further efforts could also be made to determine if R(E) depends on angle by increasing the input current for the short time necessary to determine the Faraday cup and CSI detector outputs.

The time dependence of film characteristics could also be measured. It would be interesting to know if the time degradation depends only on the total number of particles which have bombarded the film or if rate is a significant factor.

The total number of particles stopped by the film would be an important check on the techniques used in this research. Such a determination could be made by a nuclear activation analysis of the lithium remaining in the carbon film. Study of the crystalline structure after bombardment should show any changes in the structure due to bombardment.

The thickness appears in Lindhard's theory always multiplied by density. In order to compare directly to the stopping theories of Lindhard et al.[2] films could be obtained whose thickness had been determined directly in mass per unit area. However for Meyer's theory the density enters separately and would have to be determined for accurate comparisons.

APPENDICES

APPENDIX I

DETERMINATION OF $G_E(E_o)$

To obtain charged particle distributions from the energy analyzer output, it is necessary to know the integral of the analyzer transmission function with respect to input particle energies. The function $G_E(E_o)$ was defined by Equation 4 in Chapter II.

$$G_E(E_o) \equiv \int_{-\infty}^{\infty} g(E,E_o)dE \qquad \text{(A-1)}$$

where $g(E,E_o)$ is the transmission function. The first variable of the argument is the energy of the incoming particle and the second is the energy E_o for which the analyzer is tuned. However, it was more convenient to integrate with respect to the tuned energy E_o. This appendix establishes the justification of this procedure.

This is a central force problem in classical mechanics. The time can be eliminated from the equations of motion to obtain[32] the following orbit equation.

$$\frac{d^2}{d\theta^2}\left(\frac{1}{r}\right) + \frac{1}{r} = \frac{mr^2}{L^2} F(r) \qquad \text{(A-2)}$$

where L is $mr^2 \frac{d\theta}{dt}$ which is known to be a constant. With the electric field given in Paris and Hurd,[33] the force F(r) can be written

$$F(r) = q\mathcal{E}(r) = - \frac{q\ V_a}{\ln(b/a)} \frac{1}{r} \qquad A\text{-}3)$$

The parameters a and b are the radii of the cylindrical surfaces which have a potential difference of V_a applied, and q is the charge of the particle.

Since L is a constant, it can be determined from the initial velocity (v_o) and radius (r_o). Thus L can be written as

$$L = mr_o v_o = mr_o \sqrt{2E/m} \qquad (A\text{-}4)$$

where E is the initial energy of the particle entering the detector. If equations A-3 and A-4 are substituted into Equation A-2, the result can be written

$$\frac{d^2}{d\theta^2}\left(\frac{1}{r}\right) + \frac{1}{r} = \frac{q\ V_a}{2E\ \ln(b/a)} \frac{r}{r_o^2} \qquad (A\text{-}5)$$

If E_o is defined by

$$E_o \equiv \frac{q\ V_a}{2\ \ln(b/a)} \qquad (A\text{-}6)$$

then Equation A-5 becomes

$$\frac{d^2}{d\theta^2}\left(\frac{1}{r}\right) + \frac{1}{r} = \frac{E_o}{E} \frac{r}{r_o^2} \qquad (A\text{-}7)$$

This equation shows that E_o can be interpreted as the energy for which the analyzer is tuned since when E is equal to E_o the radius has the

constant value of r_o and the particle passes through entrance and exit slits. More importantly, this equation shows that the trajectory does not depend on the individual values of E and E_o but only on their ratio.

This important result can be written in terms of the transmission function $g(E,E_o)$. If γ is defined to be the ratio of E_o to E, then

$$g(E,E_o) = g(E_o/\gamma,E_o) = g(E_o,\gamma E_o) \tag{A-8}$$

If β is then defined by

$$\gamma \equiv 1 - \beta \tag{A-9}$$

Equation A-8 becomes

$$g(E_o/[1-\beta],E_o) = g(E_o,[1-\beta]E_o) \tag{A-10}$$

Since g is zero unless E is very close to E_o (see Figures 10 or 12), the interesting values of γ are those close to one. For this case $|\beta| \ll 1$ and Equation A-10 becomes

$$g(E_o + \beta E_o,E_o) = g(E_o,E_o - \beta E_o) \tag{A-11}$$

For the case of β not extremely small, both sides are zero so Equation A-11 is true for all values of β. This important result was checked experimentally at 9.5 keV.

If we let E be $E_o + \beta E_o$ in Equation A-1 and change variables of integration to β, we have

$$G_E(E_o) = \int_{-\infty}^{\infty} g(E_o + \beta E_o, E_o) E_o d\beta \tag{A-12}$$

which with the help of Equation A-11 becomes

$$G_E(E_o) = \int_{-\infty}^{\infty} g(E_o, E_o - \beta E_o) E_o d\beta \tag{A-13}$$

If we now let E_o' be $E_o - \beta E_o$ and again change variables of integration we have

$$G_E(E_o) = \int_{-\infty}^{\infty} g(E_o, E_o') dE_o' \tag{A-14}$$

This equation shows that for calibration we can fix the input energy to the analyzer and vary the energy for which the analyzer is tuned. The resulting function can then be integrated with respect to the tuned energy to obtain $G_E(E_o)$.

The consequences of Equation A-7 can be further used to show that $G_E(E_o)$ depends linearly on E_o. Let

$$\epsilon \equiv \frac{E}{E_o} \tag{A-15}$$

Since the transmission function $g(E,E_o)$ depends only on the ratio of E to E_o Equation A-8 could have been written

$$g(E,E_o) = g^*(\epsilon) \tag{A-16}$$

where g^* is a function which depends only on ϵ.

Substitution of this result into the definition (A-1) yields

$$G_E(E_o) = \int_{-\infty}^{\infty} g^*(\epsilon)\,dE \qquad \text{(A-17)}$$

It is obvious that for $E_o > 0$, positive constants k_1 and k_2 can be found so that

$$g(E,E_o) = 0 \quad \text{for } E > k_2E_0 \quad \text{or} \quad E < k_1E_o \qquad \text{(A-18)}$$

This allows the replacement of the infinite limits with finite limits

$$G_E(E_o) = \int_{k_1E_o}^{k_2E_o} g^*(\epsilon)\,dE \qquad \text{(A-19)}$$

Changing the variable of integration from E to ϵ gives

$$G_E(E_o) = E_o \int_{k_1}^{k_2} g^*(\epsilon)\,d\epsilon \qquad \text{(A-20)}$$

Therefore

$$G_E(E_o) = kE_o \qquad \text{(A-21)}$$

where k is some constant.

It should be noted that this derivation assumes that the detection of transmitted particles is not a function of energy. The derivation of Equation A-14 allows for this possibility by leaving the E_o in the transmission function. For the present apparatus, a Li^+ ion sees an attractive

potential of 2.5 kV when it leaves the analyzer. Hence all Li^+ has at least 2.5 keV of energy when it strikes the Channeltron. For such energetic particles the detection efficiency is not expected to vary with energy.

APPENDIX II

ANALYZER OUTPUT FOR SLOWLY VARYING DISTRIBUTIONS

The transmission function $g(E,E_o)$ is approximately symmetric as can be seen in Figure 10 or Figure 12. That is

$$g(E_o + \beta, E_o) \approx g(E_o - \beta, E_o) \tag{A-22}$$

This symmetry allows a relaxation of the strong requirement in Chapter III that $f_\theta(E)$ be nearly constant in the in the interval $[E_o-\alpha, E_o+\alpha]$ to obtain its value at E_o. The analyzer output can be written

$$I_E(E_o,\theta) = C(\theta)\Delta\,\Omega_E \int_{-\infty}^{\infty} g(E,E_o) f_\theta(E)\,dE \tag{A-23}$$

It is convenient to look first only at the integral. If $f_\theta(E)$ varies slowly in the interval $[E_o-\alpha, E_o+\alpha]$ for which $g(E,E_o)$ is not equal to zero, then the integral is simplified. That is if $f_\theta(E)$ can be represented by the first two terms of a Taylor Series Expansion

$$f_\theta(E) = f_\theta(E_o) + K(E - E_o) \quad \text{for} \quad E_o - \alpha \leqq E \leqq E_o + \alpha \tag{A-24}$$

where K is a constant then

$$\int_{-\infty}^{\infty} g(E,E_o) f_\theta(E)\,dE = \int_{E_o-\alpha}^{E_o+\alpha} g(E,E_o) f_\theta(E_o)\,dE \qquad \text{(A-25)}$$

$$+ K \int_{E_o-\alpha}^{E_o+\alpha} g(E,E_o)(E - E_o)\,dE$$

The limits have been reduced to the interval where the integrand is not zero. If we let β be $E-E_o$ and break the last integral into two integrals we obtain

$$\int_{-\infty}^{\infty} g(E,E_o) f_\theta(E)\,dE = f_\theta(E_o) G_E(E_o) + K\Big[\int_o^{\alpha} \beta g(E_o + \beta, E_o)\,d\beta \qquad \text{(A-26)}$$

$$+ \int_{-\alpha}^{o} \beta g(E_o + \beta, E_o)\,d\beta\Big]$$

Substitution of Equation A-22 into and change of variable to $\beta' = -\beta$ in the above yields

$$\int_{-\infty}^{\infty} g(E,E_o) f_\theta(E)\,dE = f_\theta(E_o) G_E(E_o) + K\Big[\int_o^{\alpha} \beta g(E_o + \beta, E_o)\,d\beta \qquad \text{(A-27)}$$

$$- \int_o^{\alpha} \beta' g(E_o + \beta', E_o)\,d\beta'\Big]$$

or

$$\int_{-\infty}^{\infty} g(E,E_o) f_\theta(E)\,dE = f_\theta(E_o) G_E(E_o) \qquad \text{(A-28)}$$

Hence Equation A-23 can be written

$$I_E(E_o,\theta) = C(\theta)\Delta\,\Omega_E f_\theta(E_o)G_E(E_o) \qquad \text{(A-29)}$$

Alternate derivations of Equation A-30 based on the mean value theorem for Reiman-Stieltjes integrals[34] or on approximations of average values[22] are possible.

APPENDIX III

DATA

This appendix contains all of the data not included in the text. All figures are first and the tables follow. The data are ordered as the 10, 8, 6, and 4 keV input energies for which they pertain. All 8 keV figures are in the text. All symbols are defined in the text and again in Appendix IV for easy reference.

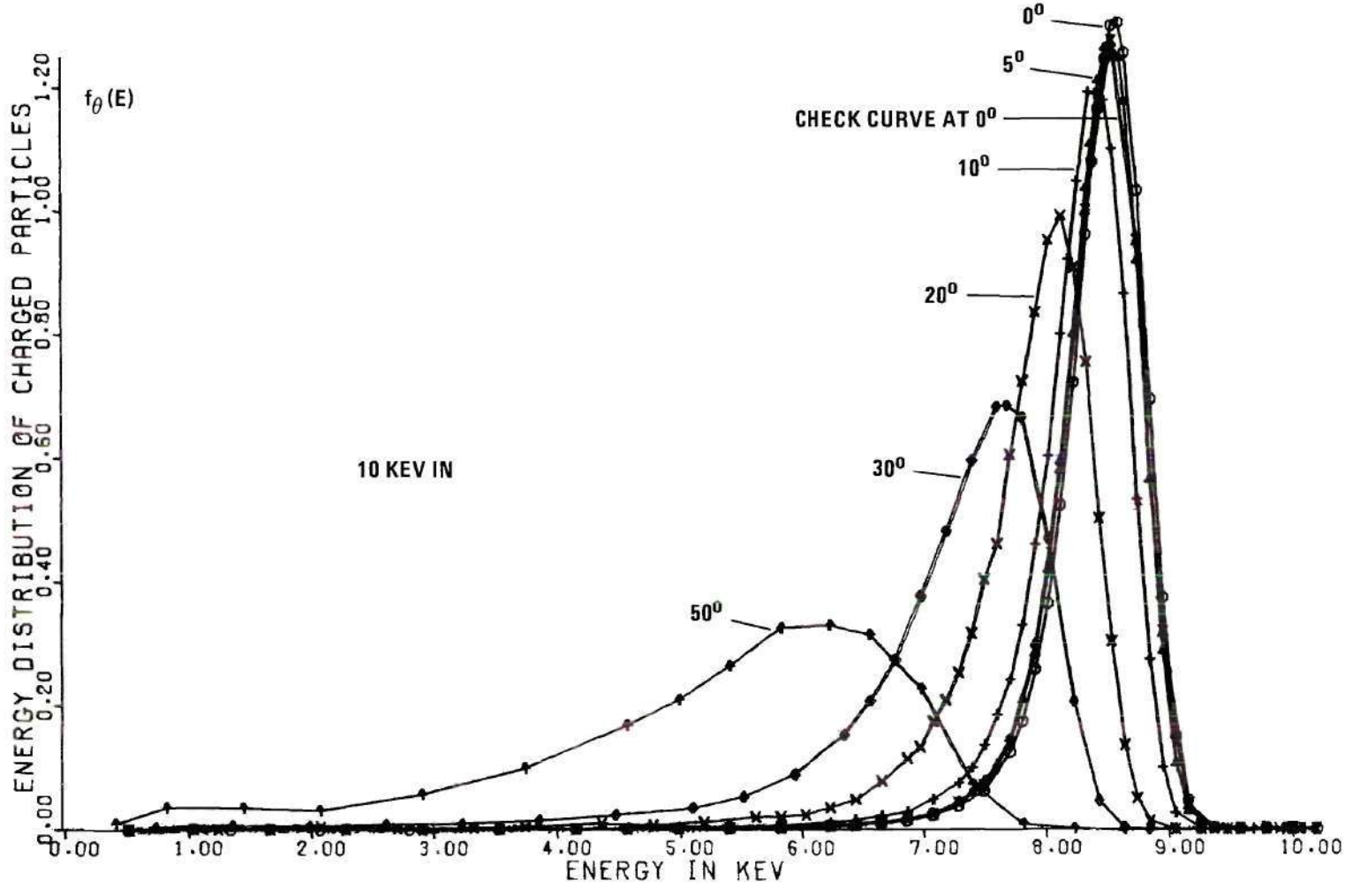

Figure 29. Energy Distributions of Li^+ for 10 keV Input

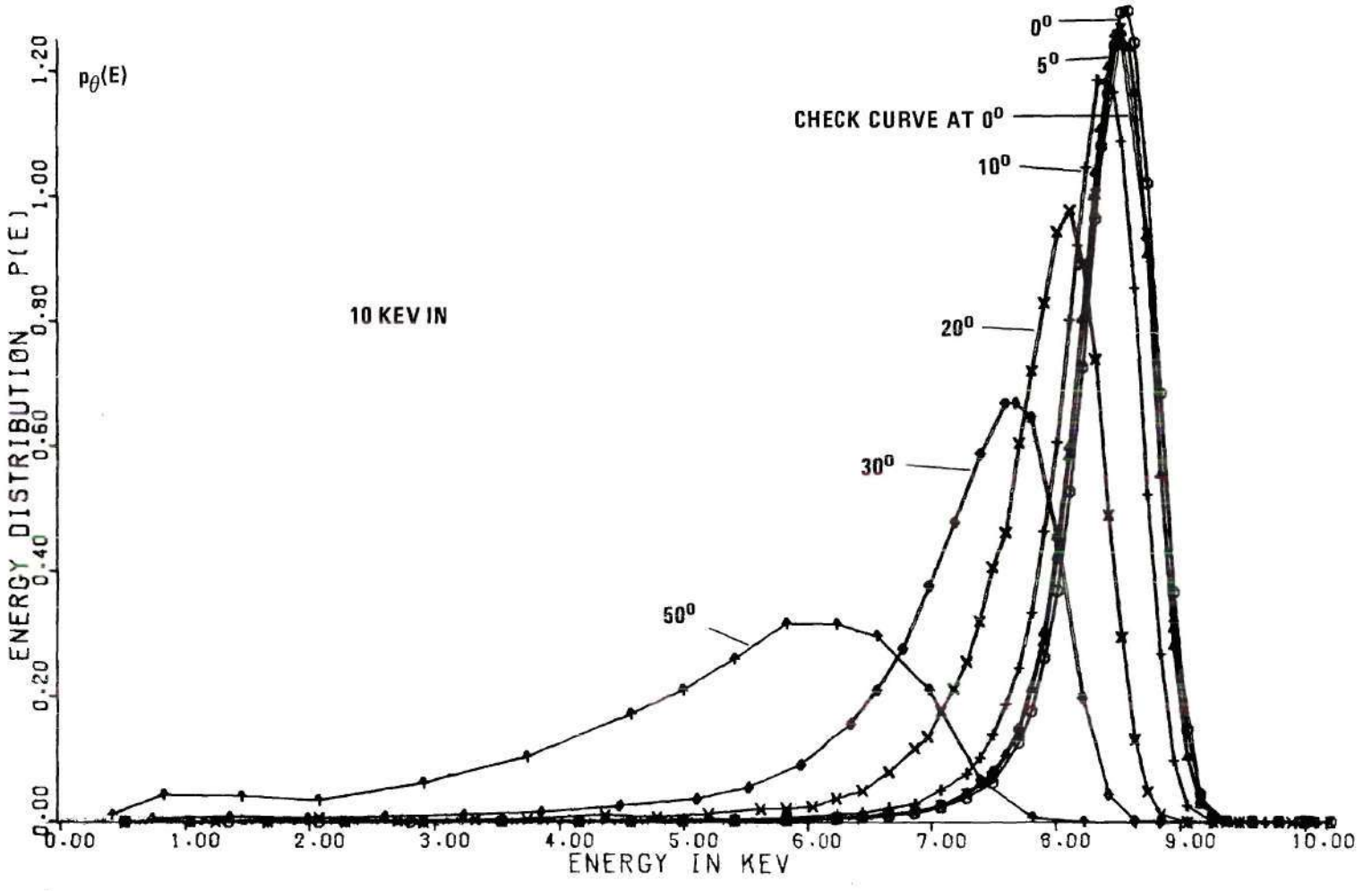

Figure 30. Total Particle Energy Distributions for 10 keV Input

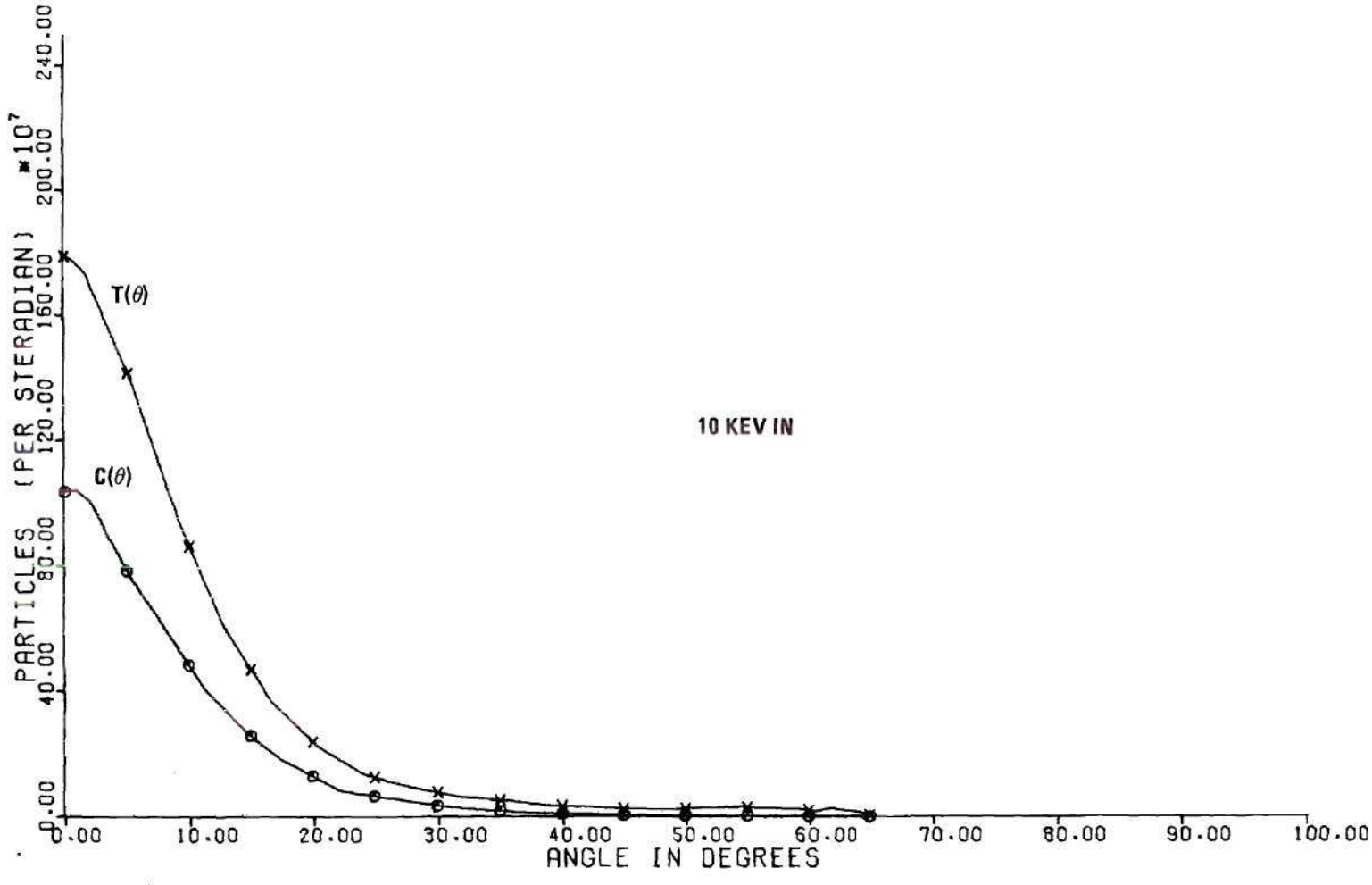

Figure 31. Fluxes of Positive and Total Particles for 10 keV Input

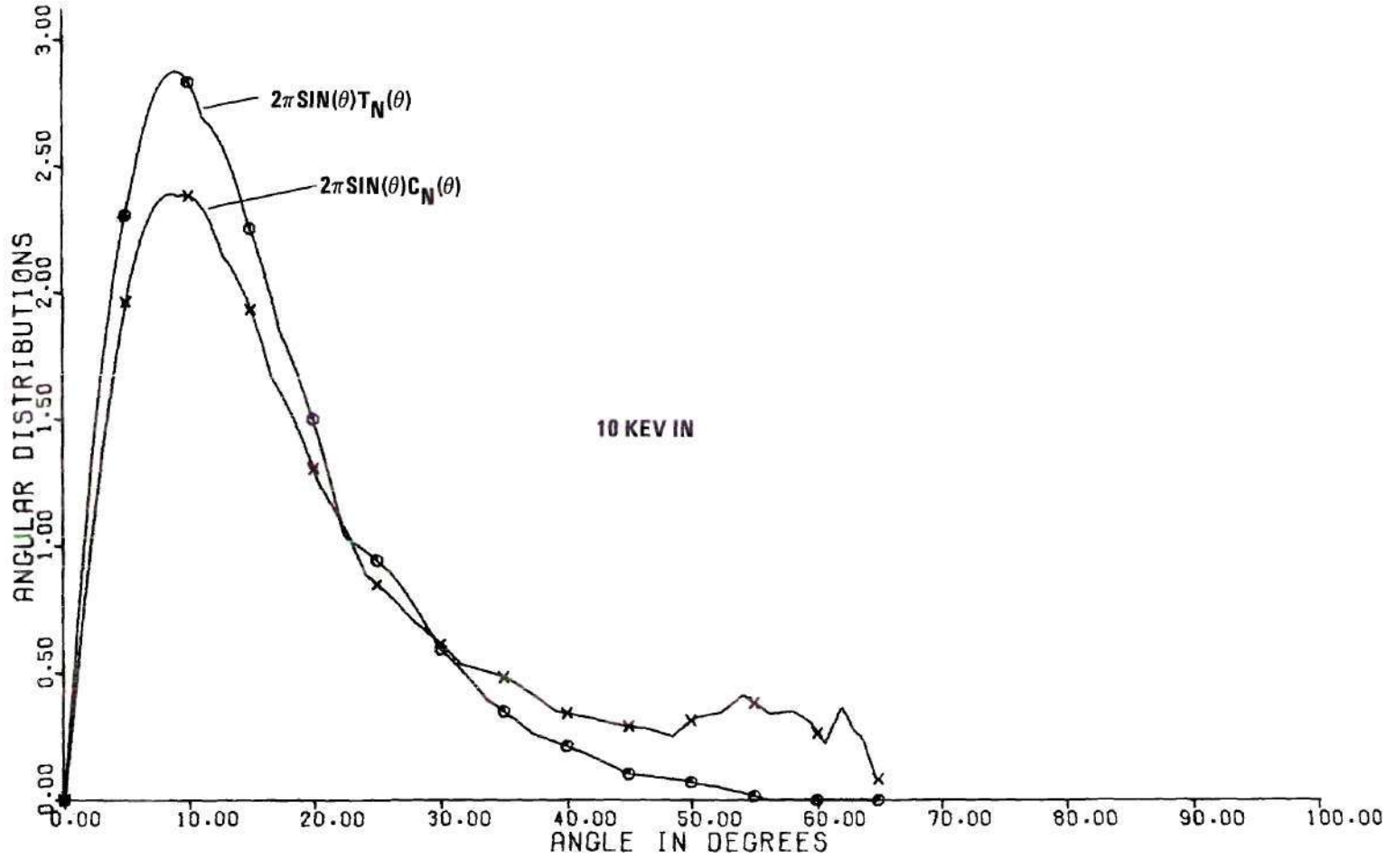

Figure 32. Angular Distributions for 10 keV Input

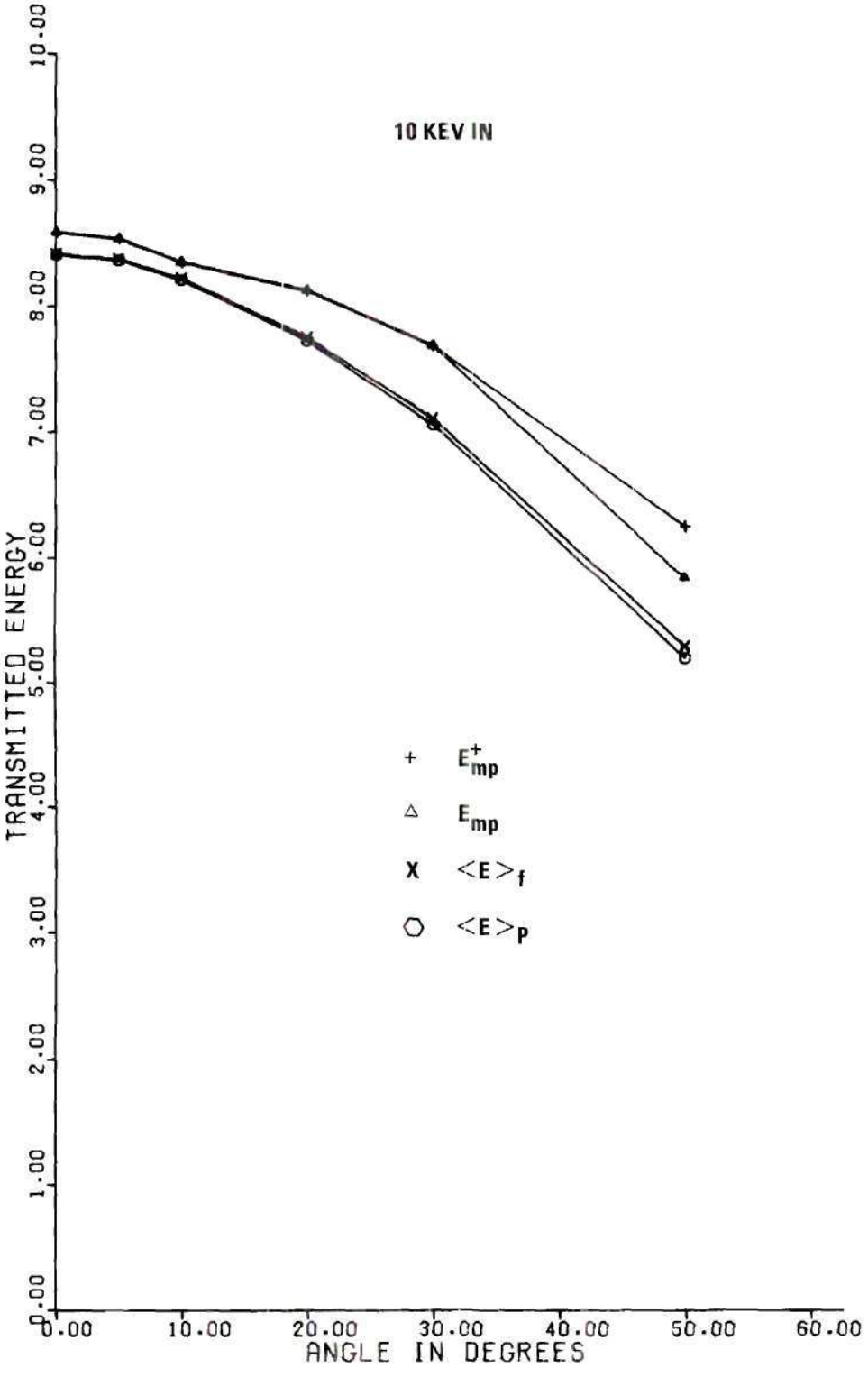

Figure 33. Transmitted Energies for 10 keV Input (Energy in keV)

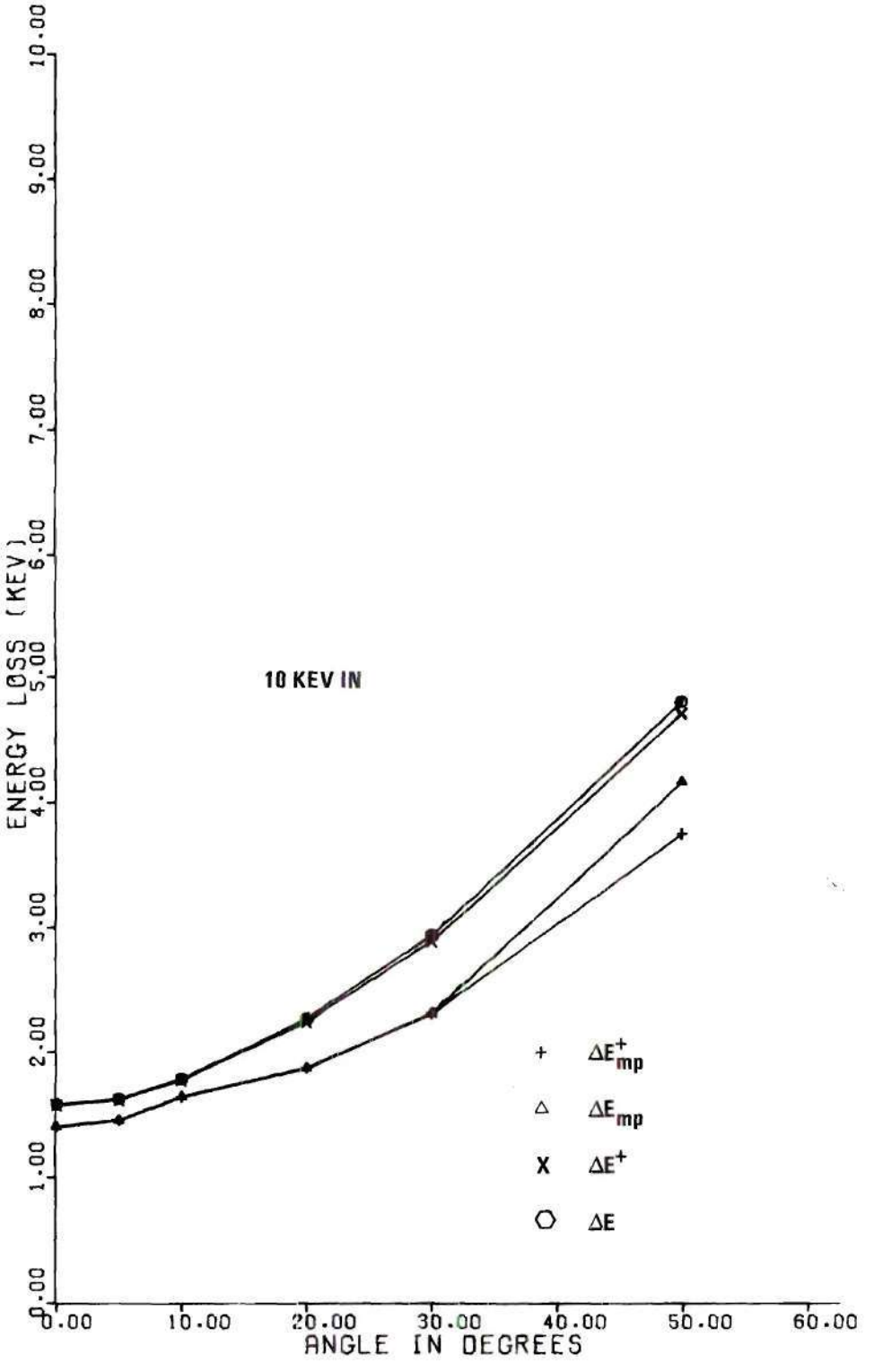

Figure 34. Energy Losses for 10 keV Input

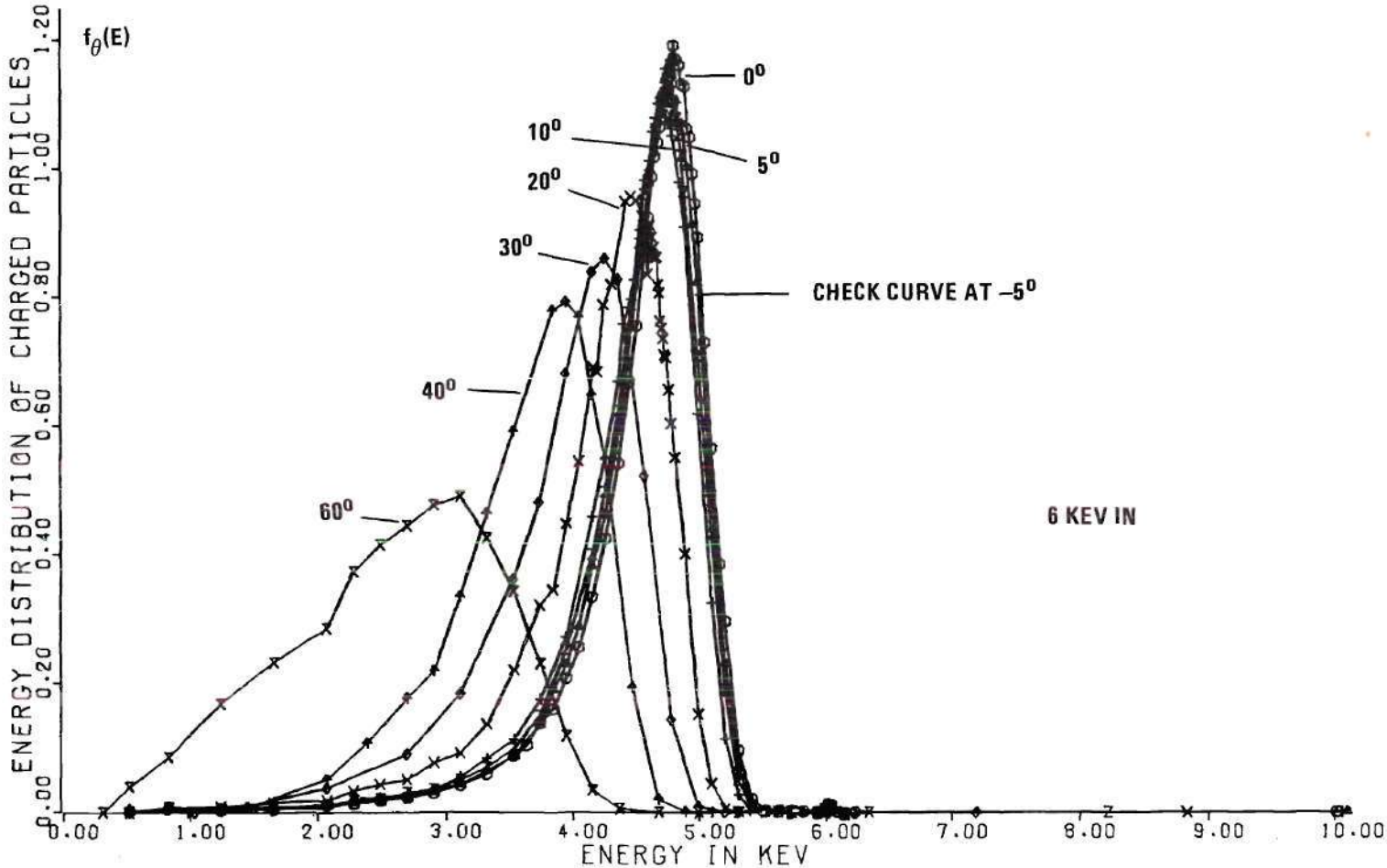

Figure 35. Energy Distributions of Li^+ for 6 keV Input

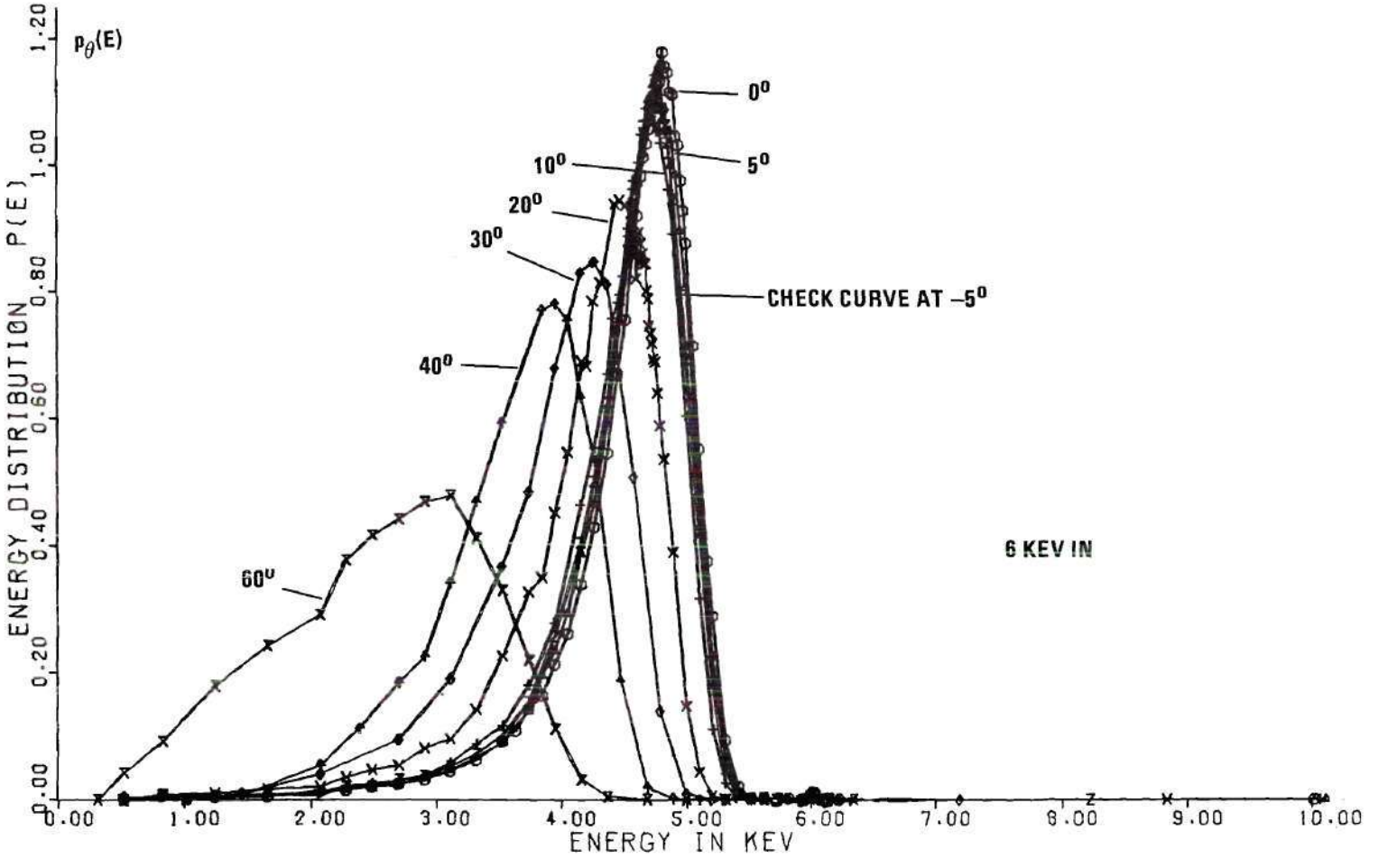

Figure 36. Total Particle Energy Distributions for 6 keV Input

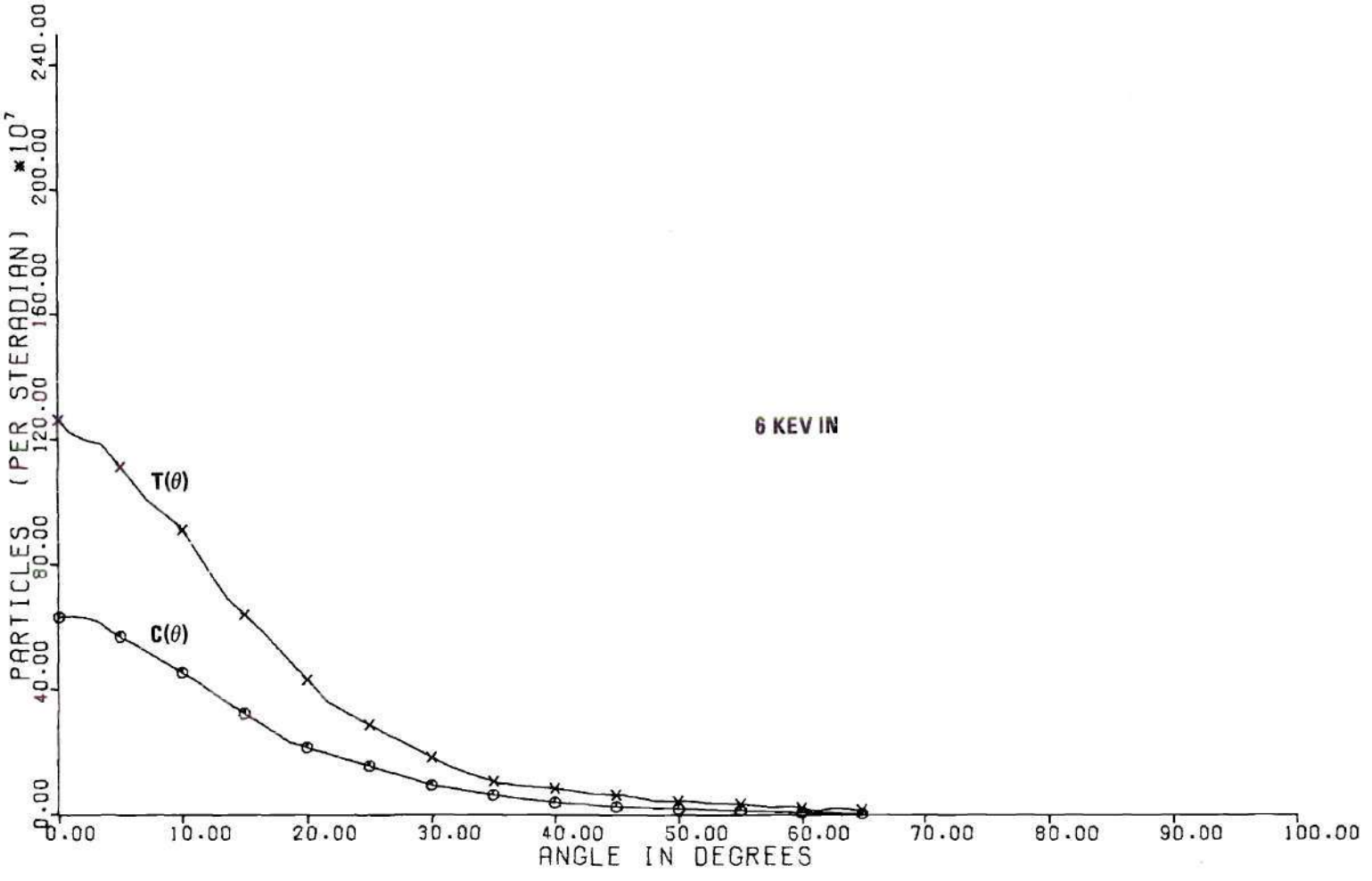

Figure 37. Fluxes of Positive and Total Particles for 6 keV Input

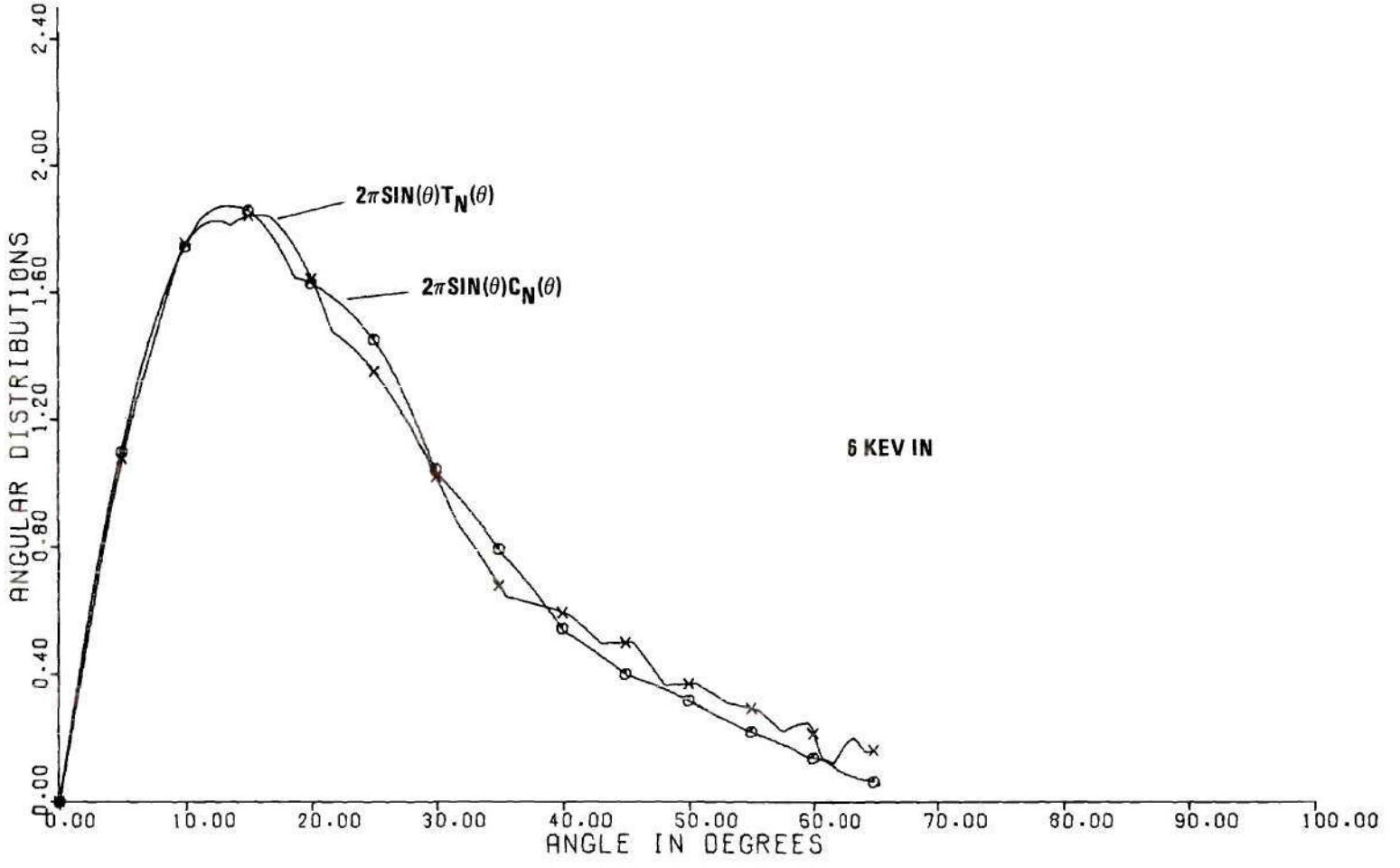

Figure 38. Angular Distributions for 6 keV Input

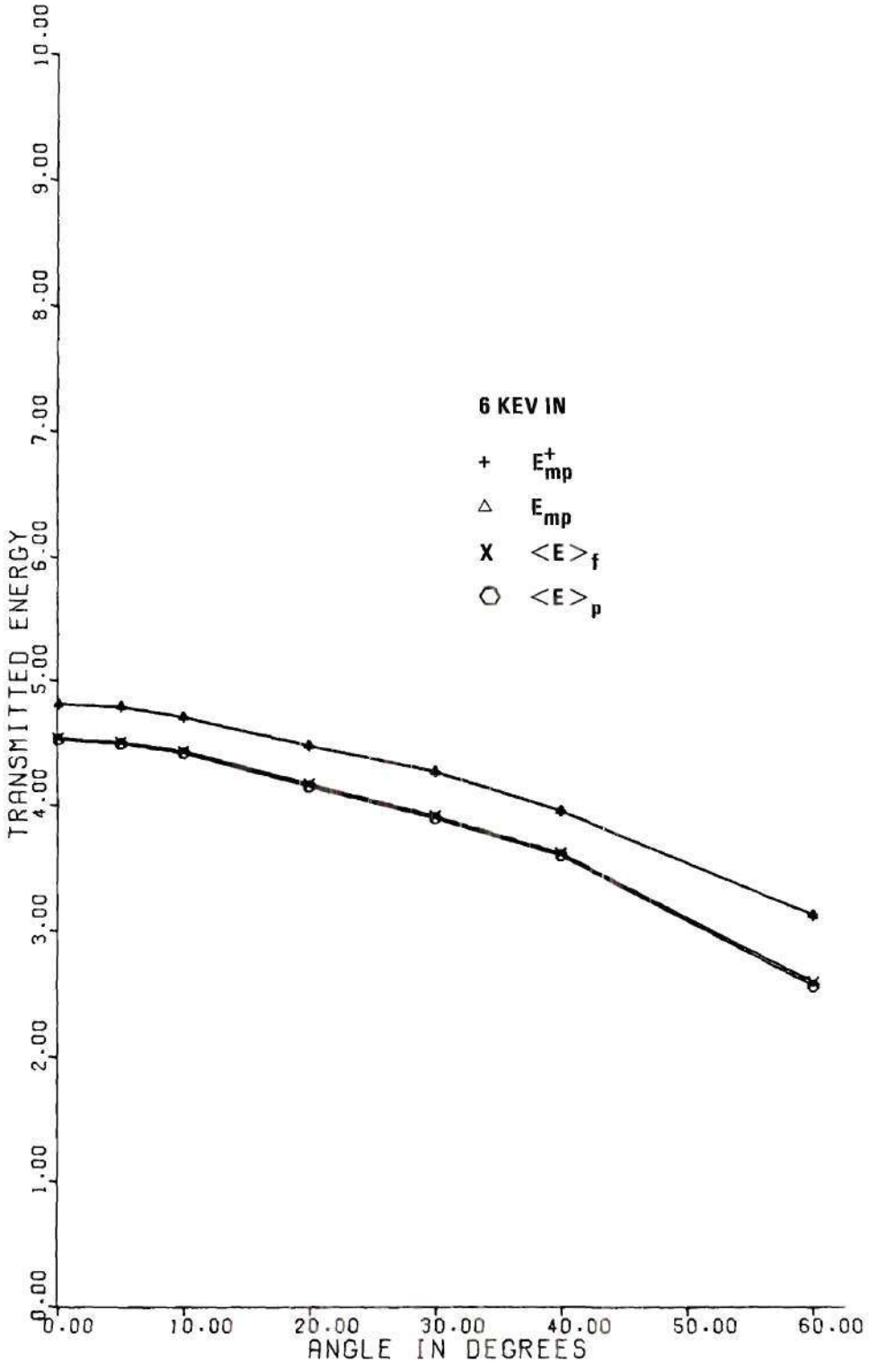

Figure 39. Transmitted Energies for 6 keV Input (Energy in keV)

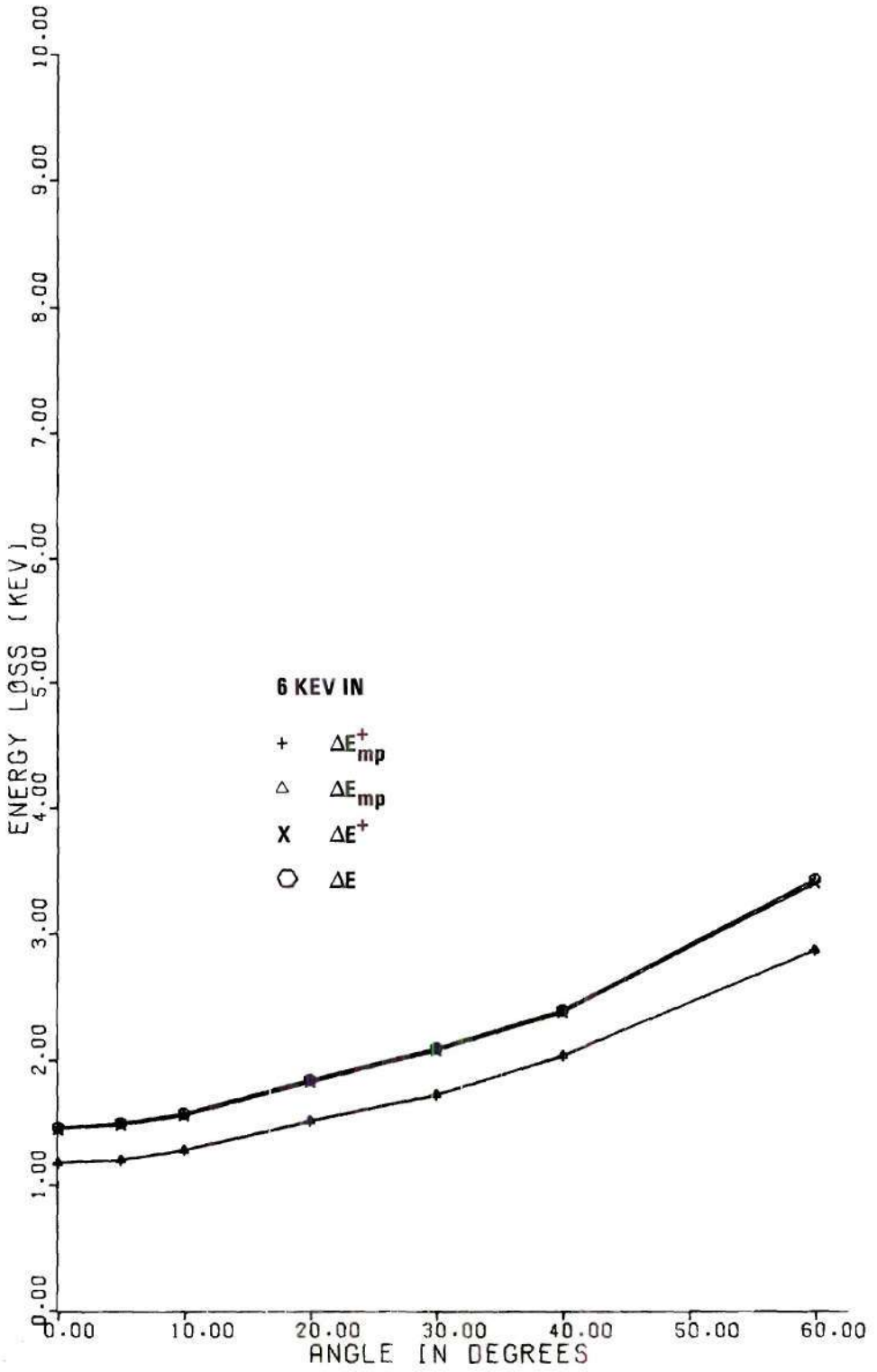

Figure 40. Energy Losses for 6 keV Input

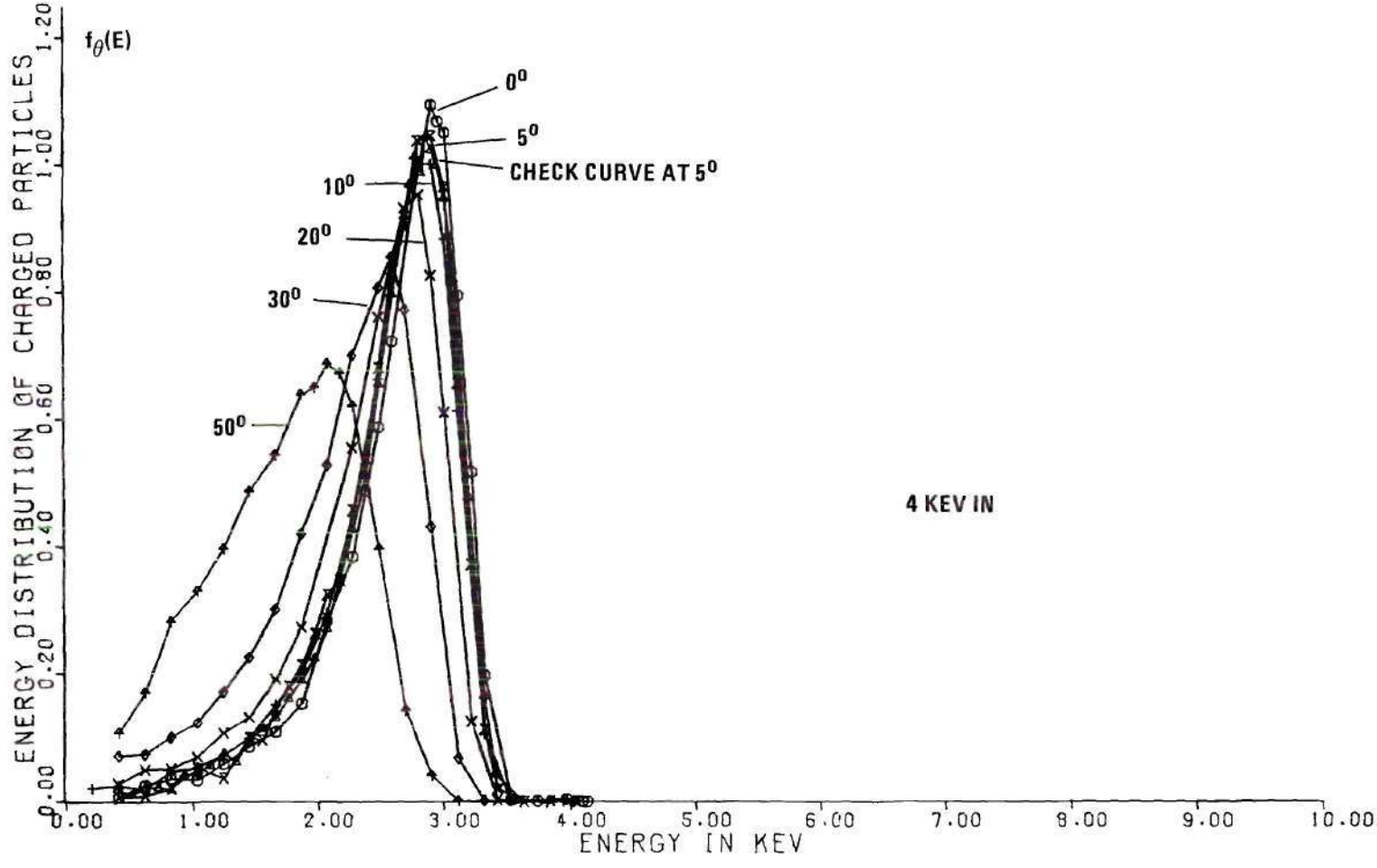

Figure 41. Energy Distributions of Li^+ for 4 keV Input

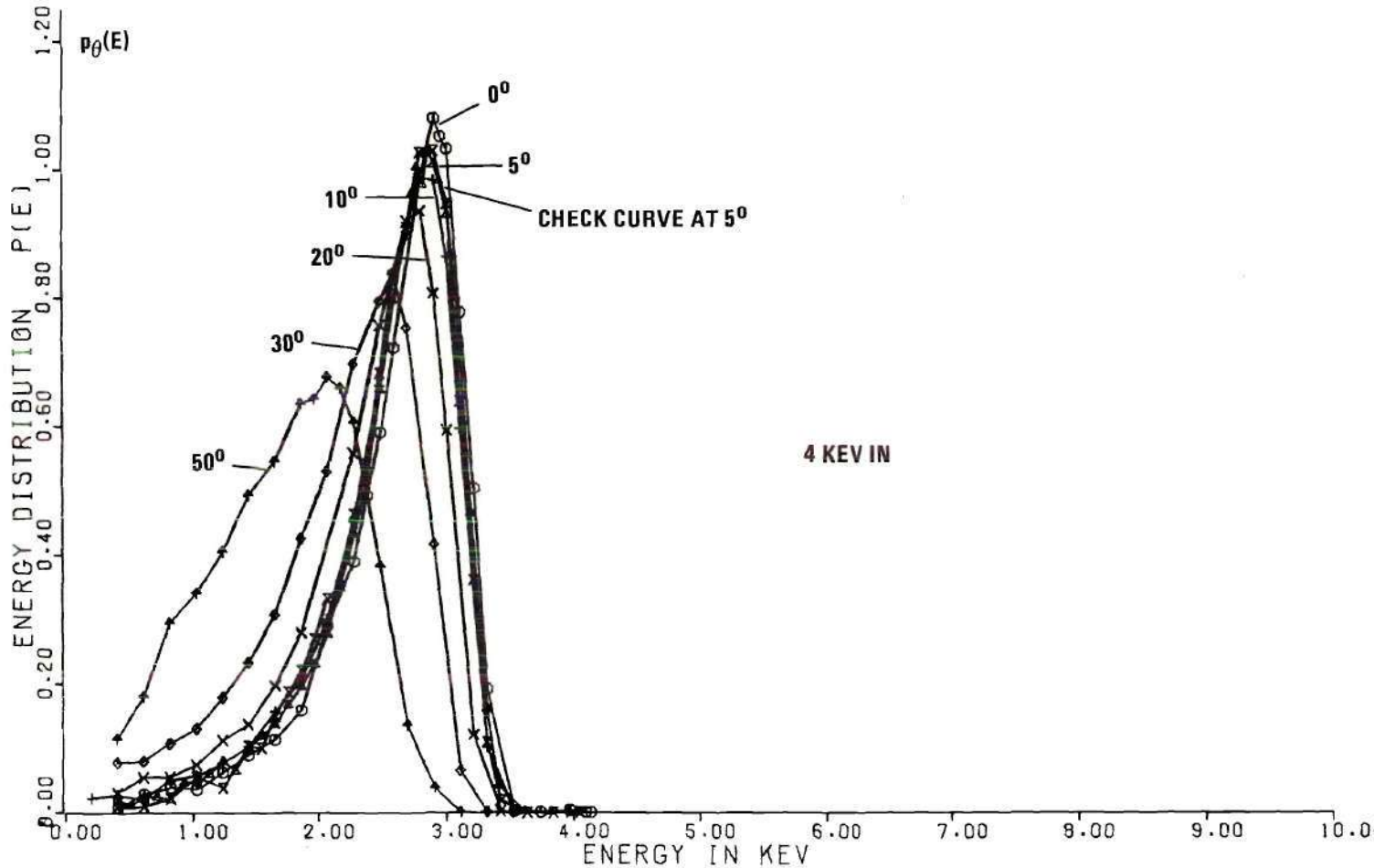

Figure 42. Total Particle Energy Distributions for 4 keV Input

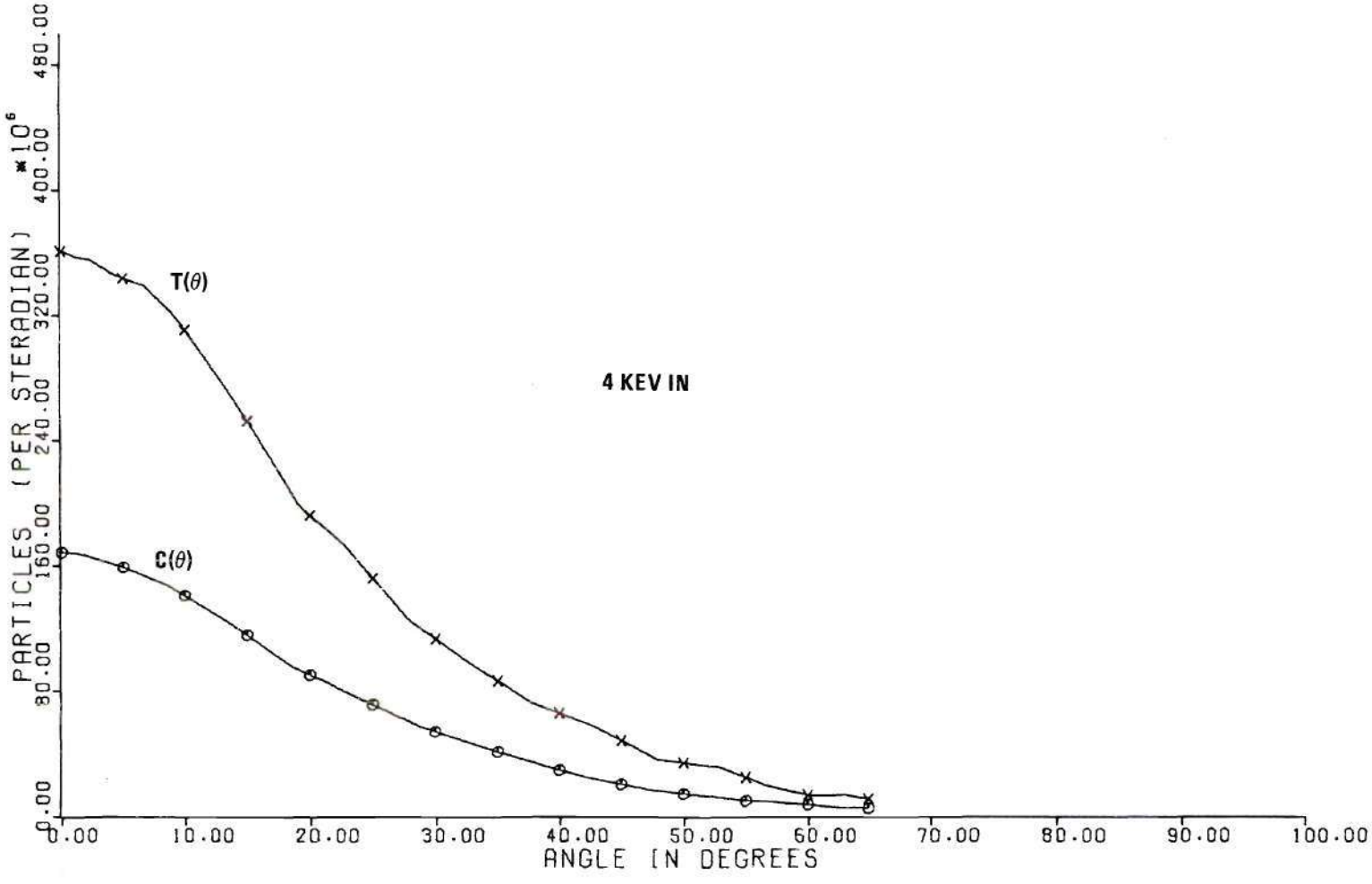

Figure 43. Fluxes of Positive and Total Particles for 4 keV Input

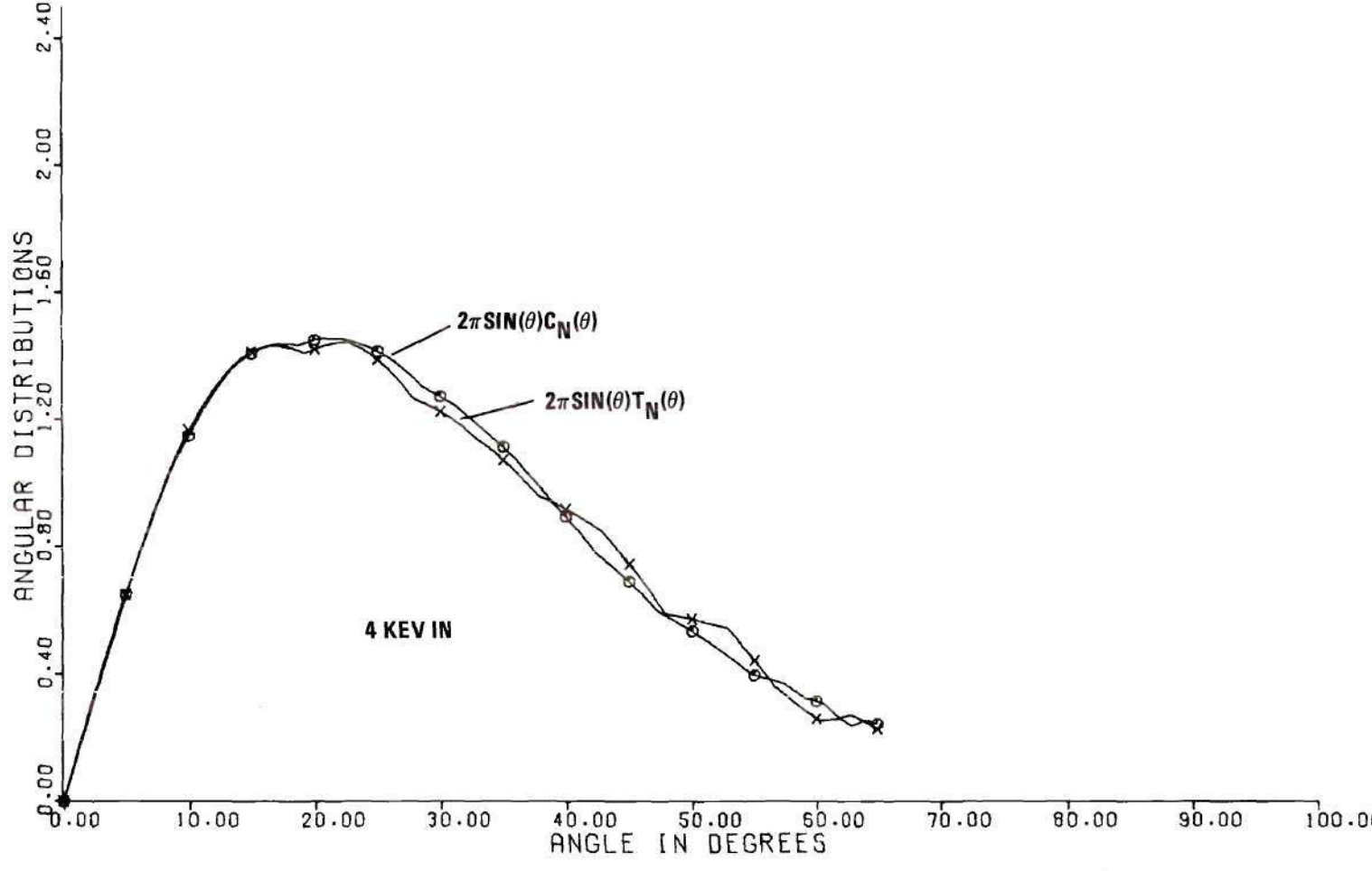

Figure 44. Angular Distributions for 4 keV Input

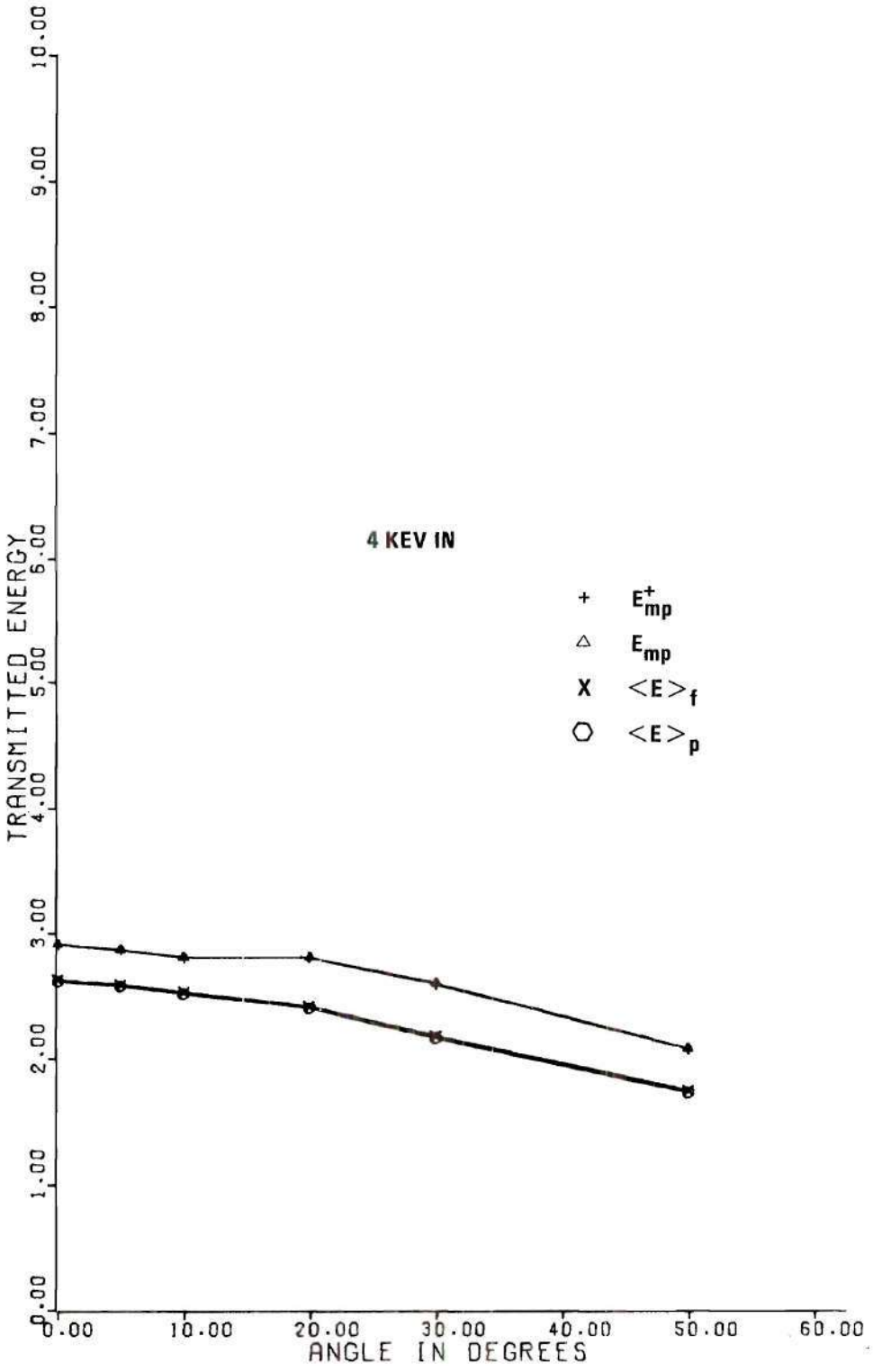

Figure 45. Transmitted Energies for 4 keV Input (Energy in keV)

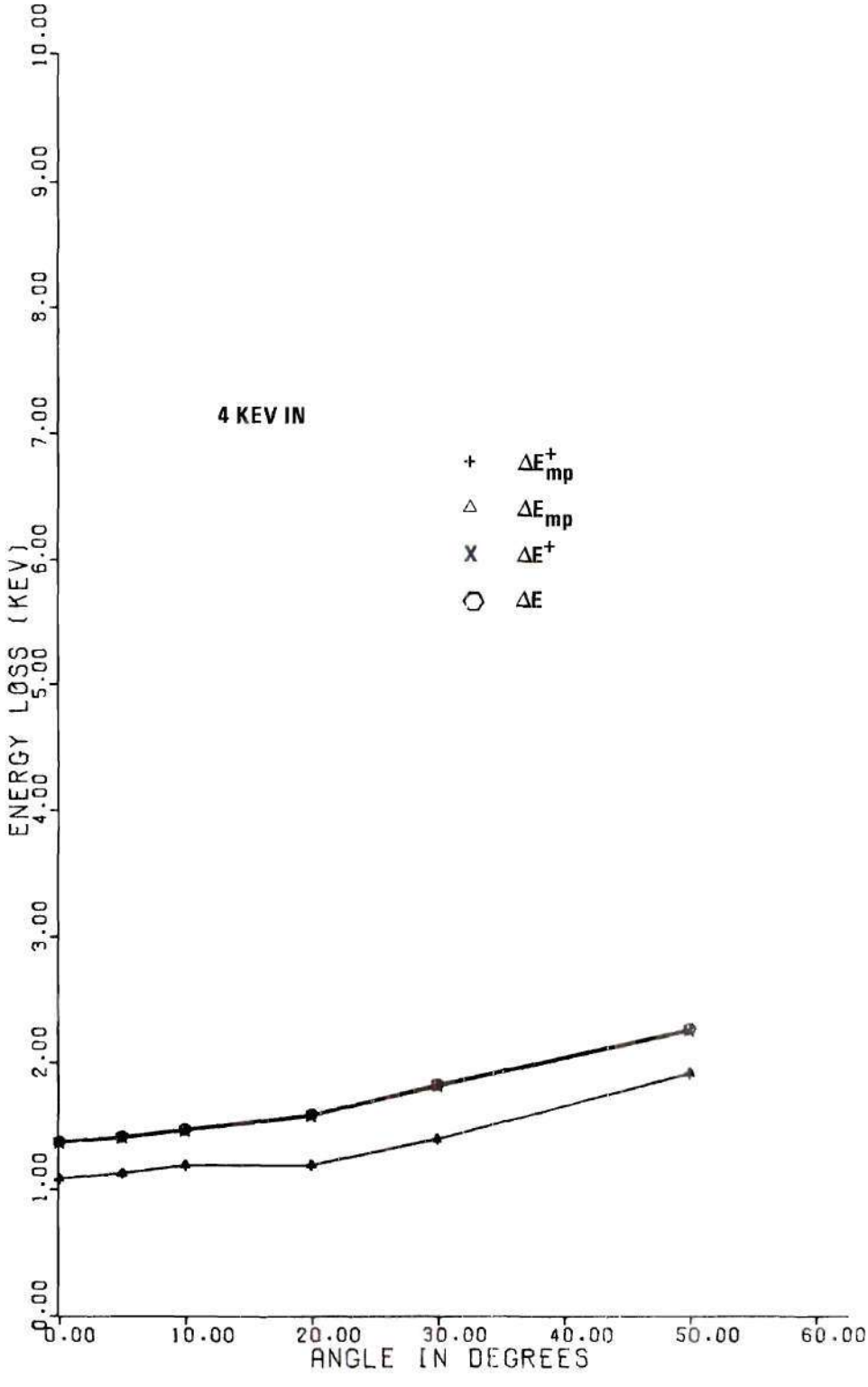

Figure 46. Energy Losses for 4 keV Input

Table 4. Consistency Checks for Input Energy of 10 keV

TOTAL LI+ DETECTED / INPUT LI WAS .543

TOTAL PARTICLES DETECTED / INPUT LI WAS 1.150

θ	$\frac{C_E(\theta)}{C(\theta)}$	$\left\langle \frac{1}{R} \right\rangle_f \frac{C}{T}$	$\frac{\langle G_T(E) \rangle_p}{G_T(\langle E \rangle_p)}$	$\frac{\langle E \rangle_f}{\langle E \rangle_p}$	$\frac{E^+_{mp}}{E_{mp}}$	$\frac{\Delta E^+}{\Delta E}$	$\frac{\Delta E^+_{mp}}{\Delta E_{mp}}$
.0	.98	1.00	1.00	1.00	1.00	1.00	1.00
5.0	1.13	.96	1.00	1.00	1.00	1.00	1.00
10.0	1.06	.97	1.00	1.00	1.00	.99	1.00
20.0	1.09	.96	1.00	1.00	1.00	.99	1.00
30.0	1.34	.82	1.00	1.01	1.00	.98	1.00
50.0	3.39	.21	.99	1.02	1.07	.98	.90
.0	1.03	1.00	1.00	1.00	1.00	1.00	1.00

AVERAGE ENERGY OF LI+ PARTICLES = 7.90

AVERAGE ENERGY OF ALL PARTICLES = 7.49

AVERAGE DEFLECTION ANGLE OF LI+ = 15.25 DEGREES

AVERAGE DEFLECTION ANGLE OF ALL = 20.32 DEGREES

AVERAGE ENERGY LOSS OF ALL PARTICLES = 2.51 KEV

Table 5. Transmitted Energies for 10 keV Input

θ	$\langle E \rangle_p$	E_{mp}	$\langle E \rangle_f$	E^+_{mp}
.0	8.416	8.593	8.423	8.593
5.0	8.372	8.542	8.379	8.542
10.0	8.214	8.356	8.225	8.356
20.0	7.732	8.128	7.758	8.128
30.0	7.062	7.692	7.109	7.692
50.0	5.196	5.833	5.291	6.249
.0	8.388	8.540	8.395	8.540

Table 6. Energy Losses for 10 keV Input

θ	ΔE	ΔE_{mp}	ΔE^{+}	ΔE^{+}_{mp}
.0	1.584	1.407	1.577	1.407
5.0	1.628	1.458	1.621	1.458
10.0	1.786	1.644	1.775	1.644
20.0	2.268	1.872	2.242	1.872
30.0	2.938	2.308	2.891	2.308
50.0	4.804	4.167	4.709	3.751
.0	1.612	1.460	1.605	1.460

Table 7. Energy Distributions for 10 keV Input Energy and Deflection Angle of 0 Degrees

E	$p_\theta(E)$	$f_\theta(E)$
.5222	.0000	.0000
1.3553	.0000	.0000
2.0826	.0000	.0000
2.8130	.0000	.0000
3.5408	.0007	.0005
4.1665	.0010	.0008
4.5830	.0012	.0010
4.9999	.0017	.0015
5.4166	.0022	.0019
5.8335	.0039	.0035
6.2499	.0057	.0053
6.4583	.0071	.0066
6.6665	.0113	.0106
6.8753	.0146	.0138
7.0834	.0257	.0226
7.2919	.0391	.0376
7.5003	.0633	.0613
7.7089	.1273	.1242
7.8130	.1776	.1739
7.9173	.2632	.2587
8.0214	.3700	.3649
8.1256	.5290	.5237
8.2300	.7274	.7227
8.3334	.9650	.9623
8.3853	1.0818	1.0806
8.4374	1.1656	1.1665
8.4897	1.2443	1.2475
8.5410	1.2966	1.3022
8.5930	1.2993	1.3073
8.6449	1.2483	1.2582
8.7486	1.0222	1.0340
8.8527	.6852	.6955
8.9563	.3674	.3743
9.0605	.1484	.1517
9.1638	.0447	.0459
9.2683	.0097	.0100
9.3716	.0022	.0023
9.5795	.0005	.0006
9.7875	.0006	.0006
9.9956	.0002	.0002
10.2031	.0000	.0000

Table 8. Energy Distributions for 10 keV Input Energy and Deflection Angle of 5 Degrees

E	$p_\theta(E)$	$f_\theta(E)$
.5208	.0000	.0000
1.0416	.0000	.0000
1.6670	.0000	.0000
2.2915	.0002	.0002
2.9165	.0004	.0003
3.5417	.0005	.0004
4.1673	.0006	.0005
4.5841	.0012	.0011
5.0007	.0016	.0014
5.4177	.0029	.0026
5.8347	.0032	.0029
6.2511	.0070	.0065
6.4591	.0101	.0094
6.6673	.0129	.0121
6.8756	.0185	.0175
7.0841	.0269	.0257
7.2924	.0466	.0448
7.3968	.0604	.0584
7.5007	.0808	.0783
7.6049	.1081	.1052
7.7091	.1494	.1460
7.8135	.2126	.2085
7.9178	.3047	.2999
8.0220	.4242	.4191
8.1263	.5995	.5942
8.2306	.8040	.8001
8.3342	1.0396	1.0383
8.3759	1.1094	1.1095
8.4382	1.2099	1.2127
8.4907	1.2614	1.2666
8.5419	1.2644	1.2718
8.6045	1.2395	1.2495
8.6459	1.1671	1.1782
8.7499	.9076	.9194
8.8538	.5545	.5638
8.9578	.2812	.2869
9.0618	.1035	.1059
9.1655	.0275	.0282
9.3737	.0011	.0011
9.5819	.0000	.0000
9.7897	.0000	.0000
9.9979	.0000	.0000

Table 9. Energy Distributions for 10 keV Input Energy and Deflection Angle of 10 Degrees

E	$p_\theta(E)$	$f_\theta(E)$
.5209	.0000	.0000
1.0417	.0000	.0000
1.6671	.0000	.0000
2.2917	.0009	.0007
2.9168	.0007	.0005
3.5422	.0013	.0011
4.1680	.0013	.0011
4.5849	.0021	.0019
5.0018	.0042	.0037
5.4187	.0051	.0046
5.8358	.0077	.0071
6.2522	.0124	.0116
6.4606	.0159	.0149
6.6692	.0234	.0222
6.8776	.0300	.0286
7.0859	.0511	.0491
7.2941	.0778	.0753
7.3986	.1030	.1001
7.5028	.1402	.1367
7.6068	.1893	.1853
7.7108	.2469	.2426
7.8151	.3349	.3303
7.9194	.4650	.4602
8.0237	.6076	.6036
8.1278	.8036	.8012
8.1900	.9234	.9226
8.2632	1.0480	1.0498
8.3557	1.1886	1.1947
8.4184	1.1831	1.1916
8.4809	1.1701	1.1810
8.5423	1.0896	1.1022
8.6466	.8542	.8671
8.7504	.5257	.5335
8.8544	.2697	.2757
8.9580	.0984	.1009
9.0614	.0264	.0271
9.2694	.0005	.0005
9.4775	.0001	.0001
9.6850	.0000	.0000
10.1010	.0000	.0000

Table 10. Energy Distributions for 10 keV Input Energy and Deflection Angle of 20 Degrees

E	$p_\theta(E)$	$f_\theta(E)$
.5209	.0000	.0000
1.2500	.0000	.0000
2.0831	.0068	.0054
2.7082	.0025	.0021
3.3334	.0040	.0034
3.7505	.0052	.0045
4.3762	.0117	.0103
4.7928	.0079	.0070
5.2096	.0130	.0119
5.6267	.0216	.0200
5.8353	.0227	.0212
6.0438	.0252	.0237
6.2519	.0380	.0360
6.4603	.0506	.0483
6.6688	.0806	.0776
6.8774	.1181	.1145
6.9816	.1366	.1329
7.0858	.1783	.1743
7.1900	.2130	.2089
7.2941	.2569	.2529
7.3984	.3208	.3171
7.5025	.4078	.4045
7.6066	.4631	.4611
7.7110	.6065	.6058
7.8153	.7223	.7244
7.9196	.8305	.8360
8.0236	.9444	.9542
8.1279	.9804	.9942
8.2319	.8930	.9088
8.3352	.7407	.7565
8.4389	.4910	.5033
8.5429	.2960	.3045
8.6470	.1320	.1363
8.7509	.0490	.0508
8.8548	.0131	.0137
9.0627	.0000	.0000
9.2706	.0000	.0000
9.4787	.0000	.0000
9.8948	.0000	.0000

Table 11. Energy Distributions for 10 keV Input Energy and Deflection Angle of 30 Degrees

E	$p_\theta(E)$	$f_\theta(E)$
.7391	.0059	.0045
1.3638	.0085	.0067
1.9887	.0062	.0050
2.6131	.0095	.0080
3.2380	.0120	.0103
3.8637	.0162	.0143
4.4895	.0263	.0239
5.1149	.0373	.0347
5.5322	.0562	.0531
5.9494	.0926	.0889
6.3665	.1576	.1536
6.5754	.2115	.2078
6.7840	.2773	.2746
6.9928	.3779	.3769
7.2013	.4791	.4815
7.4098	.5887	.5961
7.6081	.6697	.6830
7.6920	.6700	.6853
7.8164	.6483	.6661
8.0247	.4534	.4692
8.2330	.1984	.2068
8.4401	.0442	.0464
8.6472	.0029	.0031
8.8540	.0001	.0001
9.2681	.0000	.0000

Table 12. Energy Distributions for 10 keV Input Energy and Deflection Angle of 50 Degrees

E	$p_\theta(E)$	$f_\theta(E)$
.4163	.0125	.0102
.8326	.0430	.0357
1.4573	.0410	.0350
2.0818	.0349	.0306
2.9149	.0624	.0569
3.7484	.1046	.0987
4.5819	.1730	.1689
4.9986	.2108	.2092
5.4159	.2615	.2637
5.8332	.3172	.3250
6.2495	.3169	.3299
6.5726	.2984	.3144
6.9896	.2121	.2269
7.4061	.0671	.0729
7.8219	.0074	.0082
8.2372	.0009	.0010
8.6512	.0000	.0000
9.0646	.0004	.0005

Table 13. Energy Distributions for 10 keV Check Curve at 0 Degrees

E	$p_\theta(E)$	$f_\theta(E)$
.5207	.0000	.0000
1.0412	.0000	.0000
1.6663	.0000	.0000
2.2908	.0002	.0002
2.9155	.0002	.0001
3.5406	.0003	.0002
4.1662	.0007	.0006
4.5826	.0007	.0006
4.9993	.0012	.0010
5.4162	.0028	.0025
5.8331	.0036	.0032
6.2492	.0067	.0062
6.4573	.0071	.0066
6.6655	.0123	.0116
6.8738	.0170	.0161
7.0820	.0255	.0243
7.2906	.0444	.0427
7.4990	.0727	.0705
7.7073	.1446	.1406
7.9158	.2919	.2871
8.1239	.5889	.5835
8.3318	1.0053	1.0033
8.5399	1.2716	1.2783
8.7477	.9414	.9531
8.9557	.3137	.3199
9.1634	.0392	.0402
9.3711	.0013	.0013
9.5788	.0003	.0003
9.7864	.0004	.0005
9.9525	.0000	.0000
9.9929	.0011	.0012
10.0132	.0012	.0013
10.0535	.0001	.0001
10.1977	.0000	.0000

Table 14. Transmitted Energies for 8 keV Input

θ	$\langle E \rangle_p$	E_{mp}	$\langle E \rangle_f$	E^+_{mp}
.0	6.474	6.682	6.486	6.682
5.0	6.428	6.637	6.441	6.637
10.0	6.304	6.573	6.320	6.573
21.0	5.933	6.365	5.956	6.365
30.0	5.399	6.048	5.440	6.048
40.0	4.696	5.422	4.754	5.631
60.0	3.504	4.263	3.560	4.263
5.0	6.359	6.567	6.372	6.567
.0	6.459	6.656	6.471	6.656

Table 15. Energy Distributions for 8 keV Input Energy and Deflection Angle of 0 Degrees

E	$p_\theta(E)$	$f_\theta(E)$
.6258	.0000	.0000
.8344	.0000	.0000
1.2517	.0021	.0017
1.6692	.0008	.0006
1.8780	.0007	.0006
2.0861	.0006	.0005
2.2948	.0027	.0023
2.5035	.0015	.0012
2.7121	.0013	.0011
2.9207	.0033	.0028
3.1295	.0025	.0020
3.3385	.0039	.0034
3.5472	.0056	.0050
3.7562	.0058	.0053
3.9650	.0069	.0063
4.1742	.0101	.0092
4.3830	.0134	.0123
4.5917	.0158	.0147
4.8005	.0198	.0186
5.0092	.0316	.0299
5.2180	.0432	.0412
5.4269	.0745	.0716
5.5314	.0848	.0819
5.6358	.1058	.1025
5.7404	.1454	.1415
5.8450	.1830	.1788
5.9495	.2327	.2282
6.0540	.3194	.3145
6.0960	.3461	.3413
6.1378	.3919	.3870
6.1800	.4296	.4249
6.2218	.4951	.4905
6.2629	.5294	.5252
6.2838	.5750	.5709
6.3257	.6223	.6189
6.3678	.7048	.7020
6.4310	.7983	.7970
6.4724	.8985	.8985
6.5143	.9817	.9831
6.5565	1.0469	1.0501
6.5989	1.1166	1.1218
6.6407	1.1598	1.1669
6.6821	1.1874	1.1966
6.7033	1.1801	1.1901
6.7452	1.1583	1.1700
6.7871	1.1325	1.1456
6.8919	.9308	.9452
6.9965	.6102	.6220
7.1010	.3261	.3336
7.2056	.1419	.1457
7.3206	.0325	.0335
7.5297	.0013	.0014
7.7389	.0009	.0009
7.9481	.0009	.0009
8.1574	.0000	.0000
8.3657	.0000	.0000
8.7836	.0001	.0001
8.9929	.0000	.0000
9.2018	.0000	.0000
9.8287	.0000	.0000
10.0376	.0001	.0001

Table 16. Energy Distributions for 8 keV Input Energy and Deflection Angle of 5 Degrees

E	$p_\theta(E)$	$f_\theta(E)$
.6259	.0046	.0036
1.2516	.0000	.0000
1.6691	.0006	.0007
2.0858	.0013	.0011
2.4002	.0005	.0005
2.7116	.0019	.0017
2.9201	.0040	.0035
3.1288	.0045	.0039
3.3375	.0034	.0030
3.5463	.0067	.0060
3.7552	.0043	.0039
3.9639	.0100	.0091
4.1730	.0103	.0094
4.3816	.0138	.0128
4.5902	.0210	.0195
4.6947	.0240	.0225
4.7991	.0226	.0213
4.9035	.0284	.0268
5.0078	.0338	.0320
5.1122	.0390	.0371
5.2166	.0493	.0471
5.3209	.0560	.0537
5.4253	.0766	.0738
5.5297	.0965	.0933
5.6342	.1251	.1214
5.7388	.1596	.1555
5.8433	.2056	.2011
5.8851	.2316	.2270
5.9688	.2795	.2747
6.0520	.3452	.3404
6.0939	.3807	.3760
6.1356	.4135	.4091
6.1778	.5011	.4965
6.2196	.5339	.5297
6.2605	.5837	.5800
6.3024	.6363	.6333
6.3441	.7178	.7156
6.3863	.7976	.7963
6.4280	.8606	.8606
6.4692	.9532	.9546
6.5112	1.0261	1.0293
6.5530	1.1084	1.1136
6.5952	1.1180	1.1250
6.6368	1.1647	1.1737
6.6780	1.1621	1.1728
6.7198	1.1403	1.1527
6.7618	1.1024	1.1160
6.8036	1.0435	1.0579
6.8454	.9087	.9228
6.8866	.8401	.8544
6.9284	.7027	.7157
6.9700	.5932	.6051
7.0123	.4668	.4769
7.0541	.3667	.3752
7.0954	.2705	.2772
7.1994	.1043	.1073
7.3038	.0275	.0284
7.5124	.0006	.0006
7.7213	.0004	.0004
7.9299	.0001	.0001
8.1385	.0000	.0000
8.3466	.0000	.0000
8.7634	.0000	.0000
9.1806	.0000	.0000
9.5976	.0000	.0000
10.0146	.0000	.0000

Table 17. Energy Distributions for 8 keV Input Energy and Deflection Angle of 10 Degrees

E	$p_\theta(E)$	$f_\theta(E)$
.8344	.0000	.0000
1.4604	.0013	.0011
2.0861	.0061	.0051
2.5033	.0021	.0018
2.9206	.0036	.0032
3.3381	.0047	.0041
3.7556	.0095	.0086
3.9643	.0157	.0143
4.3821	.0207	.0193
4.5907	.0250	.0234
4.7995	.0352	.0333
5.0080	.0528	.0503
5.2170	.0730	.0700
5.3214	.0808	.0779
5.4258	.1056	.1021
5.5303	.1320	.1282
5.6346	.1746	.1702
5.7390	.2106	.2061
5.8435	.2728	.2681
5.9478	.3540	.3493
6.0523	.4428	.4386
6.0943	.4956	.4917
6.1358	.5496	.5462
6.1782	.5777	.5750
6.2197	.6452	.6432
6.2606	.6985	.6973
6.3025	.7741	.7740
6.3443	.8545	.8557
6.3864	.8837	.8864
6.4281	.9500	.9544
6.4691	1.0222	1.0285
6.5109	1.0478	1.0558
6.5317	1.0790	1.0882
6.5525	1.0980	1.1082
6.5734	1.1170	1.1282
6.5946	1.0914	1.1032
6.6154	1.0882	1.1009
6.6361	1.0786	1.0921
6.6568	1.0512	1.0650
6.6775	1.0274	1.0417
6.7194	.9708	.9859
6.7609	.9096	.9251
6.8032	.7792	.7937
6.8448	.6782	.6918
6.8858	.5889	.6017
6.9276	.4834	.4946
6.9692	.3590	.3679
7.0114	.2836	.2911
7.0530	.1880	.1932
7.0944	.1366	.1406
7.3030	.0073	.0076
7.5116	.0000	.0000
7.7202	.0002	.0002
7.9290	.0000	.0000
8.1375	.0000	.0000
8.3450	.0000	.0000
9.3876	.0000	.0000
10.2218	.0000	.0000

Table 18. Energy Distributions for 8 keV Input Energy and Deflection Angle of 21 Degrees

E	$p_\theta(E)$	$f_\theta(E)$
1.0425	.0072	.0059
2.0851	.0061	.0052
2.7108	.0091	.0080
3.1281	.0137	.0123
3.5457	.0165	.0150
3.9634	.0300	.0278
4.3811	.0489	.0460
4.7986	.0755	.0721
5.2163	.1589	.1546
5.4252	.2271	.2228
5.6345	.3464	.3425
5.8435	.5207	.5190
6.0525	.7200	.7233
6.1571	.8146	.8215
6.2612	.8749	.8857
6.3655	.9035	.9180
6.4700	.8322	.8491
6.5745	.6715	.6876
6.6791	.4581	.4710
6.7841	.2476	.2555
6.8884	.0976	.1011
7.0975	.0046	.0048
7.3062	.0001	.0001
7.7236	.0000	.0000
8.3484	.0000	.0000
10.0146	.0000	.0000

Table 19. Energy Distributions for 8 keV Input Energy and Deflection Angle of 30 Degrees

E	$p_\theta(E)$	$f_\theta(E)$
.5212	.0079	.0064
1.0422	.0154	.0123
2.0843	.0170	.0148
2.7099	.0249	.0223
3.3355	.0369	.0340
3.7529	.0587	.0550
4.1707	.0832	.0792
4.5878	.1384	.1341
4.9008	.2171	.2130
5.2138	.3303	.3279
5.5270	.4841	.4865
5.8397	.6628	.6741
5.9444	.6752	.6894
6.0483	.6781	.6951
6.1528	.6150	.6329
6.2566	.5295	.5470
6.4649	.2467	.2568
6.8818	.0027	.0028
7.2982	.0000	.0000
10.0051	.0000	.0000

Table 20. Energy Distributions for 8 keV Input Energy and Deflection Angle of 40 Degrees

E	$p_\theta(E)$	$f_\theta(E)$
.5105	.0129	.0108
.9593	.0314	.0267
1.4593	.0396	.0345
2.0845	.0490	.0439
2.7099	.0546	.0503
3.2312	.0854	.0804
3.7530	.1347	.1297
4.1706	.1960	.1919
4.5877	.2766	.2754
5.0048	.4060	.4109
5.2135	.4829	.4928
5.4221	.5101	.5248
5.5264	.4973	.5137
5.6307	.5081	.5269
5.8396	.3999	.4180
6.0481	.2405	.2534
6.2557	.0833	.0885
6.4644	.0143	.0153
6.6722	.0008	.0008
6.8797	.0009	.0009

Table 21. Energy Distributions for 8 keV Input Energy and Deflection Angle of 60 Degrees

E	$p_\theta(E)$	$f_\theta(E)$
.5109	.0000	.0000
.9905	.0870	.0779
1.4591	.1051	.0961
2.0841	.1520	.1430
2.5947	.1952	.1878
3.0114	.2211	.2166
3.4801	.3035	.3032
3.8976	.3248	.3301
4.2634	.3579	.3692
4.6805	.2806	.2944
5.0974	.2019	.2153
5.5142	.0481	.0521
5.9309	.0086	.0095
6.3466	.0000	.0000

Table 22. Energy Distributions for 8 keV Check Curve at 5 Degrees

E	$p_\theta(E)$	$f_\theta(E)$
.5213	.0000	.0000
1.3551	.0006	.0005
2.0844	.0025	.0019
2.5012	.0012	.0011
2.9182	.0049	.0043
3.3352	.0062	.0055
3.7524	.0086	.0077
4.1699	.0132	.0122
4.5869	.0225	.0210
5.0039	.0410	.0390
5.2123	.0584	.0559
5.4209	.0950	.0916
5.6293	.1380	.1342
5.8380	.2283	.2239
6.0463	.3731	.3688
6.2544	.6611	.6585
6.3587	.8524	.8524
6.4625	1.0284	1.0324
6.5669	1.1690	1.1780
6.6707	1.1192	1.1322
6.7749	.9425	.9571
6.9832	.3750	.3837
7.1913	.0613	.0632
7.3995	.0021	.0022
7.6074	.0003	.0003
7.8155	.0001	.0001
8.2318	.0000	.0000

Table 23. Energy Distributions for 8 keV Check Curve at 0 Degrees

E	$p_\theta(E)$	$f_\theta(E)$
.5199	.0000	.0000
1.0428	.0012	.0010
1.4601	.0009	.0007
1.8774	.0007	.0005
2.0856	.0000	.0000
2.5027	.0034	.0029
2.9198	.0033	.0028
3.3372	.0024	.0022
3.7547	.0061	.0055
4.1724	.0130	.0119
4.3809	.0089	.0082
4.5897	.0138	.0128
4.7982	.0247	.0232
5.0069	.0352	.0333
5.2157	.0458	.0437
5.4245	.0713	.0686
5.5290	.0940	.0908
5.6332	.1099	.1065
5.7378	.1382	.1345
5.8424	.1988	.1942
5.9469	.2473	.2426
6.0511	.3196	.3148
6.1137	.3866	.3810
6.1555	.4346	.4297
6.1978	.4809	.4763
6.2395	.5351	.5308
6.4889	.9491	.9502
6.5309	1.0384	1.0411
6.5726	1.0658	1.0703
6.5939	1.0895	1.0950
6.6146	1.1392	1.1458
6.6353	1.1501	1.1576
6.6560	1.1813	1.1899
6.6764	1.1731	1.1825
6.6976	1.1700	1.1803
6.7185	1.1627	1.1739
6.7394	1.1528	1.1648
6.7604	1.1372	1.1499
6.7811	1.1005	1.1137
6.8025	1.0596	1.0730
6.8230	1.0235	1.0373
6.8438	.9773	.9913
6.8645	.9358	.9498
6.8852	.8909	.9049
6.9059	.8145	.8280
6.9478	.6907	.7032
6.9895	.5831	.5946
7.0938	.3198	.3273
7.1979	.1250	.1284
7.3022	.0334	.0344
7.5109	.0015	.0015
7.7194	.0017	.0017
7.9278	.0009	.0009
8.1362	.0000	.0000
8.3441	.0000	.0000
8.5524	.0000	.0000
9.3861	.0000	.0000

Table 24. Consistency Checks for Input Energy of 6 keV

TOTAL LI+ DETECTED / INPUT LI WAS .502

TOTAL PARTICLES DETECTED / INPUT LI WAS 1.000

θ	$\frac{C_E(\theta)}{C(\theta)}$	$\left\langle \frac{1}{R} \right\rangle_f \frac{C}{T}$	$\frac{\langle G_T(E) \rangle_p}{G_T(\langle E \rangle_p)}$	$\frac{\langle E \rangle_f}{\langle E \rangle_p}$	$\frac{E^+_{mp}}{E_{mp}}$	$\frac{\Delta E^+}{\Delta E}$	$\frac{\Delta E^+_{mp}}{\Delta E_{mp}}$
ANGLE	CE/CF	C/RT	GT/GT	AVE+/AVE	MP+/MP	LOS+/LOS	MPLOS+/MP
.0	1.01	1.00	.99	1.00	1.00	.99	1.00
5.0	.98	1.02	.99	1.00	1.00	.99	1.00
10.0	.94	1.00	.99	1.00	1.00	.99	1.00
20.0	.94	1.01	.99	1.00	1.00	.99	1.00
30.0	.83	1.05	.99	1.00	1.00	.99	1.00
40.0	.69	.94	.99	1.00	1.00	.99	1.00
60.0	3.17	.82	.94	1.01	1.00	.99	1.00
-5.0	.99	1.04	.99	1.00	1.00	.99	1.00

AVERAGE ENERGY OF LI+ PARTICLES = 4.07

AVERAGE ENERGY OF ALL PARTICLES = 4.03

AVERAGE DEFLECTION ANGLE OF LI+ = 22.65 DEGREES

AVERAGE DEFLECTION ANGLE OF ALL = 23.38 DEGREES

AVERAGE ENERGY LOSS OF ALL PARTICLES = 1.97 KEV

Table 25. Transmitted Energies for 6 keV Input

θ	$\langle E \rangle_p$	E_{mp}	$\langle E \rangle_f$	E^+_{mp}
.0	4.531	4.815	4.545	4.815
5.0	4.496	4.794	4.510	4.794
10.0	4.422	4.712	4.436	4.712
20.0	4.154	4.481	4.171	4.481
30.0	3.901	4.271	3.916	4.271
40.0	3.604	3.959	3.619	3.959
60.0	2.566	3.128	2.596	3.128
-5.0	4.462	4.752	4.477	4.752

Table 26. Energy Losses for 6 keV Input

θ	ΔE	ΔE_{mp}	ΔE^{+}	ΔE^{+}_{mp}
.0	1.469	1.185	1.455	1.185
5.0	1.504	1.206	1.490	1.206
10.0	1.578	1.288	1.564	1.288
20.0	1.846	1.519	1.829	1.519
30.0	2.099	1.729	2.084	1.729
40.0	2.396	2.041	2.381	2.041
60.0	3.434	2.872	3.404	2.872
-5.0	1.538	1.248	1.523	1.248

Table 27. Energy Distributions for 6 keV Input Energy and Deflection Angle of 0 Degrees

E	$p_\theta(E)$	$f_\theta(E)$
.5210	.0020	.0017
.8335	.0063	.0053
1.2504	.0041	.0036
1.6673	.0054	.0048
2.0837	.0137	.0124
2.2921	.0149	.0136
2.5005	.0205	.0188
2.7089	.0251	.0233
2.9173	.0319	.0299
3.1257	.0449	.0424
3.3343	.0624	.0594
3.5427	.0917	.0881
3.6470	.1084	.1046
3.7513	.1440	.1396
3.8557	.1646	.1602
3.9600	.2131	.2083
4.0642	.2618	.2570
4.1690	.3390	.3341
4.2731	.4298	.4254
4.3772	.5459	.5426
4.4607	.6718	.6699
4.5236	.7575	.7573
4.5857	.8688	.8707
4.6170	.9222	.9254
4.6484	.9841	.9888
4.6693	1.0151	1.0207
4.6900	1.0365	1.0431
4.7114	1.0592	1.0668
4.7321	1.1055	1.1144
4.7531	1.1136	1.1235
4.7739	1.1357	1.1467
4.7945	1.1350	1.1470
4.8153	1.1812	1.1946
4.8364	1.1585	1.1727
4.8572	1.1490	1.1640
4.8781	1.1182	1.1337
4.8990	1.1145	1.1309
4.9204	1.0487	1.0651
4.9412	1.0346	1.0515
4.9620	.9777	.9945
4.9830	.9302	.9470
5.0034	.8789	.8955
5.0555	.7159	.7309
5.1077	.5521	.5649
5.1707	.3758	.3854
5.2122	.2882	.2960
5.3166	.0927	.0956
5.4210	.0199	.0207
5.5252	.0023	.0024
5.6296	.0021	.0022
5.8270	.0015	.0015
5.9306	.0007	.0007
5.9729	.0011	.0012
5.9936	.0070	.0074
6.0146	.0117	.0124
6.0357	.0088	.0093
6.0470	.0108	.0115
6.0973	.0004	.0004
6.2446	.0000	.0000
10.0177	.0000	.0000

Table 28. Energy Distributions for 6 keV Input Energy and Deflection Angle of 5 Degrees

E	$p_\theta(E)$	$f_\theta(E)$
.5210	.0000	.0000
.8335	.0043	.0037
1.2504	.0065	.0057
1.6673	.0089	.0079
2.0836	.0108	.0097
2.2920	.0160	.0146
2.5004	.0207	.0191
2.7088	.0234	.0217
2.9171	.0372	.0348
3.1254	.0464	.0439
3.3340	.0671	.0640
3.5425	.0906	.0871
3.7511	.1398	.1356
3.8554	.1957	.1907
3.9595	.2353	.2303
4.0639	.2936	.2886
4.1684	.3873	.3822
4.2726	.4657	.4615
4.3768	.5937	.5909
4.4811	.7566	.7561
4.5852	.9062	.9095
4.6270	.9745	.9796
4.6687	1.0206	1.0276
4.7108	1.1061	1.1156
4.7315	1.1015	1.1118
4.7524	1.1293	1.1409
4.7733	1.1487	1.1614
4.7937	1.1607	1.1745
4.8144	1.0906	1.1045
4.8250	1.0728	1.0869
4.8355	1.0939	1.1087
4.8563	1.0555	1.0707
4.8771	1.0567	1.0728
4.9191	.9877	1.0044
4.9607	.8976	.9143
5.0020	.8084	.8248
5.1063	.4829	.4947
5.2104	.2258	.2323
5.3147	.0666	.0688
5.4190	.0110	.0114
5.5233	.0014	.0015
5.8153	.0003	.0003
6.0239	.0000	.0000
6.2323	.0000	.0000
10.1070	.0000	.0000

Table 29. Energy Distributions for 6 keV Input Energy and Deflection Angle of 10 Degrees

E	$p_\theta(E)$	$f_\theta(E)$
.5211	.0000	.0000
.8336	.0056	.0048
1.2506	.0025	.0021
1.6676	.0072	.0064
2.0839	.0113	.0103
2.2924	.0217	.0199
2.5007	.0249	.0230
2.7093	.0302	.0282
2.9176	.0381	.0358
3.1260	.0578	.0548
3.3346	.0873	.0835
3.5430	.1171	.1130
3.7517	.1812	.1763
3.9602	.2780	.2728
4.1690	.4643	.4596
4.2734	.5548	.5514
4.3776	.6717	.6705
4.4195	.7599	.7598
4.4612	.7851	.7863
4.5034	.8260	.8286
4.5449	.9027	.9071
4.5862	.9780	.9845
4.6280	1.0069	1.0152
4.6489	1.0512	1.0608
4.6697	1.0619	1.0724
4.6907	1.0924	1.1041
4.7119	1.0955	1.1082
4.7328	1.0808	1.0943
4.7541	1.0687	1.0829
4.7747	1.0571	1.0721
4.7953	1.0592	1.0750
4.7993	1.0381	1.0537
4.8616	.9640	.9810
4.8998	.8940	.9111
5.0039	.6059	.6200
5.1082	.3171	.3258
5.2125	.1108	.1143
5.3168	.0265	.0274
5.4005	.0031	.0032
5.6093	.0002	.0002
5.8177	.0000	.0000
6.0267	.0000	.0000
6.2351	.0000	.0000
10.0601	.0000	.0000

Table 30. Energy Distributions for 6 keV Input Energy and Deflection Angle of 20 Degrees

E	$p_\theta(E)$	$f_\theta(E)$
.5211	.0000	.0000
.8336	.0078	.0068
1.2505	.0102	.0090
1.6676	.0169	.0152
2.0839	.0206	.0189
2.2924	.0358	.0331
2.5007	.0470	.0439
2.7092	.0541	.0509
2.9176	.0812	.0772
3.1261	.0958	.0918
3.3345	.1423	.1375
3.5430	.2272	.2216
3.7517	.3271	.3218
3.8559	.3501	.3459
3.9601	.4526	.4491
4.0644	.5475	.5455
4.1791	.6921	.6928
4.2102	.6835	.6850
4.2625	.7867	.7902
4.3253	.8160	.8216
4.4395	.9405	.9514
4.4812	.9469	.9595
4.5232	.9390	.9530
4.5755	.9124	.9280
4.5860	.8955	.9112
4.5961	.8582	.8736
4.6068	.8223	.8374
4.6171	.8895	.9062
4.6277	.8967	.9139
4.6384	.8787	.8960
4.6487	.8485	.8656
4.6592	.8628	.8805
4.6693	.8459	.8636
4.6799	.8466	.8646
4.6902	.8032	.8207
4.7010	.7911	.8087
4.7115	.7475	.7645
4.7221	.7362	.7532
4.7323	.7204	.7373
4.7427	.6954	.7120
4.7531	.6907	.7074
4.7740	.6416	.6578
4.7944	.5898	.6051
4.8258	.5370	.5516
4.8988	.3903	.4021
5.0028	.1479	.1530
5.1071	.0435	.0452
5.2112	.0057	.0059
5.3156	.0005	.0005
5.7324	.0000	.0000
6.1496	.0000	.0000
8.8422	.0000	.0000

Table 31. Energy Distributions for 6 keV Input Energy and Deflection Angle of 30 Degrees

E	$p_\theta(E)$	$f_\theta(E)$
.5208	.0000	.0000
1.0414	.0000	.0000
1.4582	.0101	.0091
2.0828	.0408	.0377
2.7078	.0946	.0900
3.1245	.1905	.1845
3.5413	.3672	.3618
3.7498	.4851	.4821
3.9581	.6810	.6826
4.1667	.8316	.8407
4.2711	.8497	.8626
4.3752	.8135	.8293
4.5833	.5088	.5230
4.7916	.1399	.1450
4.9998	.0091	.0095
5.2078	.0001	.0001
5.3117	.0001	.0001
5.7283	.0000	.0000
6.1444	.0000	.0000
7.1998	.0000	.0000

Table 32. Energy Distributions for 6 keV Input Energy and Deflection Angle of 40 Degrees

E	$p_\theta(E)$	$f_\theta(E)$
.5209	.0049	.0043
.9888	.0000	.0000
1.4584	.0067	.0061
2.0833	.0545	.0510
2.3959	.1129	.1072
2.7084	.1843	.1775
2.9168	.2259	.2195
3.1252	.3420	.3352
3.3337	.4697	.4644
3.5421	.5943	.5928
3.8547	.7734	.7815
3.9587	.7835	.7951
4.0631	.7570	.7714
4.1676	.6346	.6495
4.2719	.5343	.5491
4.4803	.1875	.1943
4.6886	.0199	.0208
4.8967	.0017	.0018
5.1048	.0004	.0004
5.5213	.0000	.0000
6.1455	.0000	.0000

Table 33. Energy Distributions for 6 keV Input Energy and Deflection Angle of 60 Degrees

E	$p_\theta(E)$	$f_\theta(E)$
.3145	.0000	.0000
.5211	.0428	.0390
.8341	.0922	.0853
1.2513	.1787	.1685
1.6686	.2423	.2329
2.0852	.2911	.2850
2.2936	.3777	.3732
2.5022	.4163	.4152
2.7109	.4423	.4451
2.9192	.4696	.4768
3.1276	.4797	.4913
3.3364	.4126	.4263
3.5449	.3299	.3439
3.7535	.2201	.2314
3.9620	.1118	.1186
4.1709	.0319	.0341
4.3794	.0054	.0058
4.6918	.0005	.0005
5.0043	.0005	.0005
5.3162	.0004	.0005
6.3572	.0003	.0004

Table 34. Energy Distributions for 6 keV Check Curve at −5 Degrees

E	$p_\theta(E)$	$f_\theta(E)$
.5210	.0000	.0000
.8335	.0086	.0073
1.2502	.0056	.0049
1.6672	.0076	.0067
2.0834	.0065	.0059
2.2918	.0199	.0182
2.5001	.0216	.0199
2.7085	.0319	.0297
2.9169	.0372	.0349
3.1253	.0523	.0495
3.3339	.0722	.0690
3.5422	.1017	.0980
3.7509	.1539	.1495
3.9594	.2568	.2516
4.1682	.4031	.3984
4.2725	.4992	.4954
4.3766	.6231	.6210
4.4808	.7856	.7862
4.5435	.8777	.8806
4.5847	.9519	.9565
4.6265	.9804	.9868
4.6680	1.0596	1.0683
4.7099	1.0773	1.0880
4.7309	1.0816	1.0932
4.7518	1.1318	1.1450
4.7726	1.0881	1.1016
4.7931	1.1167	1.1315
4.8138	1.0743	1.0894
4.8347	1.0601	1.0759
4.8555	1.0332	1.0495
4.8764	1.0010	1.0176
4.8972	.9445	.9609
5.0013	.6917	.7066
5.1055	.4197	.4305
5.3137	.0485	.0502
5.4180	.0076	.0079
5.5222	.0012	.0013
5.6261	.0012	.0013
5.7302	.0007	.0007
5.9384	.0000	.0000
6.1466	.0000	.0000
8.2292	.0000	.0000

Table 35. Consistency Checks for Input Energy of 4 keV

TOTAL LI+ DETECTED / INPUT LI WAS .404

TOTAL PARTICLES DETECTED / INPUT LI WAS .876

θ	$\frac{C_E(\theta)}{C(\theta)}$	$\left\langle \frac{1}{R} \right\rangle_f \frac{C}{T}$	$\frac{\langle G_T(E) \rangle_p}{G_T(\langle E \rangle_p)}$	$\frac{\langle E \rangle_f}{\langle E \rangle_p}$	$\frac{E^+_{mp}}{E_{mp}}$	$\frac{\Delta E^+}{\Delta E}$	$\frac{\Delta E^+_{mp}}{\Delta E_{mp}}$
.0	.86	1.01	.96	1.00	1.00	.99	1.00
5.0	.92	1.00	.96	1.00	1.00	.99	1.00
10.0	.96	.98	.98	1.01	1.00	.99	1.00
20.0	1.19	1.02	.97	1.01	1.00	.99	1.00
30.0	1.26	1.05	.95	1.01	1.00	.99	1.00
50.0	1.71	.96	.96	1.01	1.00	.99	1.00
5.0	.88	1.00	.96	1.00	1.00	.99	1.00

AVERAGE ENERGY OF LI+ PARTICLES = 2.21

AVERAGE ENERGY OF ALL PARTICLES = 2.19

AVERAGE DEFLECTION ANGLE OF LI+ = 27.85 DEGREES

AVERAGE DEFLECTION ANGLE OF ALL = 27.96 DEGREES

AVERAGE ENERGY LOSS OF ALL PARTICLES = 1.81 KEV

Table 36. Transmitted Energies for 4 keV Input

θ	$\langle E \rangle_p$	E_{mp}	$\langle E \rangle_f$	E^+_{mp}
.0	2.621	2.915	2.633	2.915
5.0	2.581	2.873	2.593	2.873
10.0	2.521	2.810	2.535	2.810
20.0	2.405	2.809	2.419	2.809
30.0	2.168	2.601	2.183	2.601
50.0	1.731	2.081	1.746	2.081
5.0	2.572	2.914	2.583	2.914

Table 37. Energy Losses for 4 keV Input

θ	ΔE	ΔE_{mp}	ΔE^{+}	ΔE^{+}_{mp}
.0	1.379	1.085	1.367	1.085
5.0	1.419	1.127	1.407	1.127
10.0	1.479	1.190	1.465	1.190
20.0	1.595	1.191	1.581	1.191
30.0	1.832	1.399	1.817	1.399
50.0	2.269	1.919	2.254	1.919
5.0	1.428	1.086	1.417	1.086

Table 38. Energy Distributions for 4 keV Input Energy and Deflection Angle of 0 Degrees

E	$p_\theta(E)$	$f_\theta(E)$
.4164	.0073	.0066
.6248	.0287	.0262
.8329	.0391	.0361
1.0411	.0366	.0341
1.2494	.0626	.0591
1.4577	.0908	.0862
1.6662	.1146	.1099
1.8744	.1597	.1545
2.0822	.2916	.2848
2.2903	.3910	.3854
2.3944	.4935	.4885
2.4985	.5916	.5884
2.6028	.7240	.7234
2.8112	.9911	.9993
2.9151	1.0850	1.0968
2.9654	1.0551	1.0708
3.0193	1.0357	1.0535
3.1233	.7793	.7962
3.2275	.5058	.5190
3.3316	.1926	.1985
3.5399	.0030	.0031
3.7484	.0014	.0015
3.9775	.0039	.0041
4.1029	.0006	.0007
4.1445	.0000	.0000

Table 39. Energy Distributions for 4 keV Input Energy and Deflection Angle of 5 Degrees

E	$p_\theta(E)$	$f_\theta(E)$
.4163	.0215	.0195
.5205	.0114	.0104
.6245	.0237	.0217
.7287	.0242	.0223
.8326	.0211	.0195
.9368	.0466	.0433
1.0409	.0475	.0442
1.1450	.0605	.0567
1.2492	.0804	.0758
1.3533	.0654	.0620
1.4574	.1014	.0965
1.5615	.1196	.1143
1.6657	.1370	.1315
1.7699	.1679	.1620
1.8739	.1965	.1905
1.9781	.2317	.2256
2.0816	.2776	.2716
2.1857	.3576	.3515
2.2898	.4331	.4276
2.3939	.5172	.5130
2.4979	.6586	.6562
2.6020	.7976	.7984
2.7060	.9156	.9206
2.7479	.9636	.9706
2.7894	1.0062	1.0153
2.8315	.9790	.9897
2.8731	1.0336	1.0469
2.9143	1.0110	1.0256
2.9561	.9856	1.0010
3.0185	.9313	.9490
3.0605	.8710	.8891
3.0913	.8047	.8225
3.2060	.4658	.4784
3.3271	.1607	.1658
3.4143	.0421	.0436
3.6225	.0021	.0022
3.8309	.0013	.0014
4.0391	.0000	.0000

Table 40. Energy Distributions for 4 keV Input Energy and Deflection Angle of 10 Degrees

E	$p_\theta(E)$	$f_\theta(E)$
.2081	.0234	.0210
.4162	.0278	.0253
.6243	.0214	.0196
.8324	.0511	.0474
1.0405	.0576	.0539
1.2487	.0777	.0734
1.4569	.1040	.0992
1.6653	.1577	.1519
1.8735	.2102	.2043
2.0810	.3016	.2958
2.2891	.4535	.4488
2.4973	.6650	.6643
2.7055	.9197	.9270
2.8096	.9919	1.0043
2.9137	.9869	1.0037
3.0167	.8671	.8858
3.1218	.5986	.6142
3.3301	.1025	.1061
3.5381	.0013	.0014
3.9546	.0000	.0000

Table 41. Energy Distributions for 4 keV Input Energy and Deflection Angle of 20 Degrees

E	$p_\theta(E)$	$f_\theta(E)$
.4162	.0310	.0283
.6243	.0550	.0508
.8324	.0556	.0518
1.0404	.0749	.0705
1.2487	.1134	.1077
1.4568	.1380	.1323
1.6651	.1985	.1921
1.8732	.2809	.2744
2.2888	.5593	.5564
2.4970	.7592	.7622
2.7051	.9219	.9340
2.8091	.9386	.9551
2.9130	.8096	.8276
3.0169	.5959	.6118
3.2252	.1216	.1259
3.4334	.0025	.0026
3.6413	.0000	.0000

Table 42. Energy Distributions for 4 keV Input Energy and Deflection Angle of 30 Degrees

E	$p_\theta(E)$	$f_\theta(E)$
.4161	.0780	.0720
.6244	.0802	.0747
.8324	.1081	.1018
1.0404	.1311	.1246
1.2487	.1799	.1726
1.4568	.2340	.2266
1.6650	.3090	.3021
1.8730	.4261	.4205
2.0807	.5315	.5295
2.2888	.6982	.7019
2.4969	.7966	.8082
2.6009	.8402	.8563
2.7050	.7554	.7732
2.9130	.4181	.4318
3.1210	.0656	.0683
3.3291	.0015	.0016
3.5372	.0008	.0008

Table 43. Energy Distributions for 4 keV Input Energy and Deflection Angle of 50 Degrees

E	$p_\theta(E)$	$f_\theta(E)$
.4163	.1149	.1081
.6244	.1804	.1715
.8325	.2952	.2833
1.0405	.3417	.3311
1.2488	.4064	.3976
1.4569	.4939	.4878
1.6653	.5467	.5451
1.8733	.6362	.6403
1.9776	.6441	.6512
2.0809	.6785	.6890
2.1850	.6604	.6739
2.2891	.6070	.6223
2.4971	.3838	.3971
2.7052	.1368	.1428
2.9131	.0389	.0410
3.1211	.0009	.0010
3.3290	.0004	.0005

Table 44. Energy Distribution for 4 keV Check Curve at 5 Degrees

E	$p_\theta(E)$	$f_\theta(E)$
.4164	.0075	.0068
.6245	.0099	.0091
.8326	.0221	.0204
1.0408	.0554	.0517
1.2490	.0385	.0363
1.4572	.1042	.0992
1.5614	.1006	.0962
1.6656	.1505	.1446
1.7697	.1875	.1810
1.8737	.2215	.2148
1.9779	.2706	.2636
2.0814	.3325	.3254
2.1855	.3535	.3475
2.2895	.4637	.4580
2.3936	.5429	.5387
2.4976	.6842	.6820
2.6017	.8366	.8377
2.7057	.8977	.9029
2.8098	1.0293	1.0399
2.9138	1.0332	1.0485
3.0178	.9490	.9673
3.1219	.6420	.6572
3.2260	.3622	.3725
3.3301	.1096	.1132
3.4341	.0191	.0198
3.6423	.0000	.0000
3.8506	.0000	.0000
4.0585	.0000	.0000

APPENDIX IV

LIST OF SYMBOLS

$C(\theta)$	Flux of Li^+ at the angle θ. (particles/sec·steradian)
$C_N(\theta)$	Li^+ flux divided by all Li^+ detected per second.
E_{in}	Energy of Li^+ input beam. (keV)
$\langle E \rangle_f$	Average transmitted energy of Li^+ at a given angle. (keV)
$\langle E \rangle_p$	Average transmitted energy of charged and neutral particles at a given angle. (keV)
E^+_{mp}	Most probable transmitted energy of Li^+ at a given angle. (keV)
E_{mp}	Most probable transmitted energy of charged and neutral particles at a given angle. (keV)
ΔE^+	Average energy loss of Li^+ at a given angle. (keV)
ΔE	Average energy loss of charged and neutral particles at a given angle. (keV)
ΔE^+_{mp}	Most probable energy loss of Li^+ at a given angle. (keV)
ΔE_{mp}	Most probable energy loss of charged and neutral particles at a given angle. (keV)
ΔE_{av}	Average energy loss, ΔE, averaged over all angles. (keV)
$g(E,E_o)$	Ratio of particles of energy E which are transmitted and detected by the energy analyzer (turned to E_o) to particles entering the analyzer.
$f_\theta(E)$	Energy distribution of Li^+ at the angle θ. (per keV)

$G_E(E_o)$ Integral of $g(E,E_o)$ over all E. (keV)

$G_T(E)$ Detection efficiency of CSI detector for lithium particles of energy E.

I_o Total input particles per sec.

$I_E(E_o,\theta)$ Output of energy analyzer tuned to E_o. (counts/sec)

$I_L(\theta)$ Output of large aperture Faraday cup. (counts/sec)

$I_s(\theta)$ Output of small aperture Faraday cup. (counts/sec)

$I_T(\theta)$ Output of CSI detector. (counts/sec)

$p_\theta(E)$ Energy distribution of charged and neutral particles at the angle θ. (per keV)

R_p Projected range.

R_t Total range.

$T(\theta)$ Flux of charged and neutral particles at the angle θ. (particles/sec.steradian)

$T_N(\theta)$ Flux of charged and neutral particles divided by all of the particles detected per second.

V_a Voltage applied to energy analyzer. (kV)

$\Delta\Omega_E$ Solid angle subtended by energy analyzer entrance aperture.

$\Delta\Omega_L$ Solid angle subtended by the large aperture Faraday cup.

$\Delta\Omega_s$ Solid angle subtended by the small aperture Faraday cup.

$\Delta\Omega_T$ Solid angle subtended by the entrance aperture of the CSI detector.

BIBLIOGRAPHY*

1. Niehls Bohr, Kgl. Danske Videnskab. Selskab, Mat. Fys. Medd. 18, 1 (1948).

2. J. Lindhard and M. Scharff, Phys. Rev. 124, 128 (1961).

   J. Lindhard, M. Scharff, and H. E. Schiott, Kgl. Danske Videnskab. Selskab, Mat. Fys. Medd. 33 (No. 14), 1 (1963).

   J. Lindhard, V. Nielsen, M. Scharff, and P. V. Thomsen, Kgl. Danske Videnskab. Selskab, Mat. Fys. Medd. 33 (No. 10), 1 (1963).

   J. Lindhard V. Nielsen, and M. Scharff, Kgl. Danske Videnskab. Selskab, Mat. Fys. Medd. 36 (No. 10), 1 (1968).

3. A. Van Wijngaarden and H. E. Duckworth, Can. J. Phys. 40, 1749 (1962).

   J. H. Ormrod, and H. E. Duckworth, Can. J. Phys. 41, 1424 (1963).

   J. H. Ormrod, J. R. McDonald, and H. E. Duckworth, Can. J. Phys. 43, 275 (1965).

   J. R. McDonald, J. H. Ormrod, and H. E. Duckworth, Z. Naturforsch. 21, 130 (1966).

4. I. M. Cheshire, G. Dearnaley, and J. M. Poate, Proc. Roy. Soc. A311, p.47 (1969).

5. B. Fastrup, P. Hvelplund, and C. A. Sautter, Kgl. Danske Videnskab. Selskab, Mat. Fys. Medd. 35, (No. 10), 1 (1966).

6. K. O. Nielsen, in "Electromagnetically Enriched Isotopes and Mass Spectrometry," p. 18, Butterworths, New York and London (1956).

7. L. D. Tsendin, Sov. Phys.--Solid State 8, 956 (1966).

8. V. N. Lepeshinskaya and E. M. Zarutskii, Izv. AN SSSR, Ser. Fiz. 28, 1390 (1964).

---

*Abbreviations used herein conform to those found in the American Institute of Physics Style Manual (1969).

E. M. Zarutskii, Sov. Phys.--Solid State 6, 2995 (1965).

9. L. Meyer, Phys. Stat. Sol. (B) 44, 253 (1971).

10. G. Moliere, Z. Naturforsch. 3a, 78 (1948).

11. H. E. Schiott, Kgl. Danske Videnskab. Selskab, Mat. Fys. Medd. 35, (No. 9), 1 (1966).

12. J. B. Sanders, Can. J. Phys. 46, 455 (1968).

13. J. A. Davies, J. Friesen, and J. D. McIntyre, Can. J. Chem. 38, 1526 (1960).

J. A. Davies, J. D. McIntyre, R. L. Cushing, and M. Lounsbury, Can. J. Chem. 38, 1535 (1960).

J. A. Davies and G. A. Sims, Can. J. Chem. 39, 601 (1961).

J. A. Davies, J. D. McIntyre, and G. A. Sims, Can. J. Chem. 39, 611 (1961).

G. R. Piercey, F. Brown, J. A. Davies, and M. McCargo, Phys. Rev. Letters 10, 399 (1963).

B. Domeij, F. Brown, J. A. Davies, G. R. Piercy, and E. V. Kornelsen, Phys. Rev. Letters 12, 363 (1964).

B. Domeij, F. Brown, J. A. Davies, and M. McCargo, Can. J. Phys. 42, 1624 (1964).

E. V. Kornelsen, F. Brown, J. A. Davies, B. Domeij, and G. R. Piercy, Phys. Rev. 136, A849 (1964).

F. Brown, G. C. Ball, D. A. Channing, L. M. Howe, J. P. S. Pringle, and J. L. Whiston, Nuc. Inst. and Meth. 38, 249 (1965).

L. Eriksson, J. S. Davies, and P. Jespersgaard, Phys. Rev. 161, 219 (1967).

L. Eriksson, Phys. Rev. 161, 235 (1967).

P. Jespersgaard and J. A. Davies, Can. J. Phys. 45, 2983 (1967).

14. C. F. Barnett and J. A. Ray, Thermonuclear Division Semi-annual Progress Report No. ORNL-4063, 67 (April 1965).

15. A. Van Wijngaarden and L. Hastings, Can. J. Phys. 45, 2239 (1967).

L. Hastings, P. R. Ryall, and A. Van Wijngaarden, Can. J. Phys. 45, 2333 (1967).

16. W. White and R. M. Mueller, J. Appl. Phys. 38, 3660 (1967).

17. K. Morita, H. Akimune, and T. Suita, J. Phys. Soc. Japan 22, 1503 (1967).

K. Morita, H. Akimune, and T. Suita, J. Phys. Soc. Japan 25, 1525 (1968).

18. F. Bernhard, V. Muller-Jahreis, G. Rockstroh, and S. Schwave, Phys. Stat. Sol. 35, p.285 (1969).

F. Bernhard, J. Lippold, L. Meyer, S. Schwave, and R. Stolle, "Atomic Collision Phenomena in Solids," p. 663, North Holland Pub. Co., Amsterdam.

19. E. M. Zarutskii, Sov. Phys.--Solid State 9, 1172 (1967).

E. M. Zarutskii, Sov. Phys.--Solid State 9, 1495 (1968).

20. Yu. V. Gott and V. G. Tel'kovskii, Sov. Phys.--Solid State 9, 1741 (1968).

21. E. P. Arkhipov and Yu. V. Gott, Sov. Phys.--JETP 29, p.615 (1969).

22. R. L. Wax and W. Bernstein, Rev. Sci. Instr., 38, No. 11, p. 1612 (1967).

23. R. F. Goff, Rev. Sci. Instr., 39, 259 (1968).

24. R. H. Prince and J. A. Cross, Rev. Sci. Instr., 42, 66 (1971).

25. W. C. Lineberger, The Ionization of Lithium Ions by Electron Impact, Ph.D. Thesis, Georgia Institute of Technology, Atlanta, Georgia, 1965; Phys. Rev. 141, 151 (1966).

26. J. A. Phillips, Phys. Rev. 97, 404 (1955).

27. A. L. Hughes and V. Rojansky, Phys. Rev. 34, 284 (1929).

28. A. Papoulis, "Probability, Random Variables and Stochastic Processes," p. 151, McGraw Hill, New York (1965).

29. K. Bethge and H. Fabricius, Z. Physik 168, 143 (1962).

30. S. K. Allison, J. Cuevas, and M. Garcia-Munoz, Phys. Rev. 120, 1266 (1960).

31. G. D. Scott, T. A. McLauchlan, and R. S. Sennett, J. Appl. Phys. 21, 843 (1950).

32. Jerry B. Marion, Classical Dynamics, Academic Press, New York, 1965 p. 273.

33. D. T. Paris and F. K. Hurd, Basic Electromagnetic Theory, McGraw-Hill Book Company, New York, 1969 p. 154.

34. Tom M. Apostol, Mathematical Analysis, Addison-Wesley Publishing Company, Inc., Reading, Mass., 1957, p. 213.

VITA

James Coyt Majure was born in Jasper, Alabama on September 25, 1941. He is the son of H. K. and Ruth Self Majure. On August 25, 1963 he was married to Patricia Ann Paris.

Mr. Majure attended public schools in Oneonta, Alabama and was graduated from Oneonta High School in 1959. He received a Bachelor of Electrical Engineering from the Georgia Institute of Technology in June, 1963.

Mr. Majure served as platoon leader, battalion adjutant, and company commander in the 25th Signal Battalion, U. S. Army, in Karlsruhe, Germany from September, 1963 to September, 1965.

In September, 1965, he began graduate study at the Georgia Institute of Technology, where he has held graduate research and teaching assistantships. In June, 1967, he received the degree of Master of Science in Electrical Engineering from the Georgia Institute of Technology.

Mr. Majure is a member of Eta Kappa Nu, Tau Beta Phi, Phi Kappa Phi, and the Institute of Electrical and Electronics Engineers.